THE EFFECTS OF PROTO-NEUTRON STAR CONVECTION ON THE DYNAMICS AND NUCLEOSYNTHESIS OF THE NEUTRINO-DRIVEN WIND

By

Brian Powers Nevins

A DISSERTATION

Submitted to
Michigan State University
in partial fulfillment of the requirements
for the degree of

Physics—Doctor of Philosophy

2024

ABSTRACT

The neutrino-driven wind from proto-neutron stars has long been considered a possible site for interesting nucleosynthesis of heavy elements, via either an r-process, in which heavy elements are made via rapid neutron captures onto seed nuclei, or a νp-process, in which heavy elements are forged by neutrino-assisted proton captures onto seed nuclei. Many recent studies have indicated that a fiducial wind heated only by neutrino interactions does not attain a high enough entropy or a sufficiently fast expansion to allow these processes to build the heaviest elements found in nature, despite promising results in the early literature. However, a secondary heating source in the wind could strongly enhance heavy nucleosynthesis by disrupting seed nucleus formation, and allowing extended nucleon captures to build heavier elements. A promising physical source of such secondary heating is gravito-acoustic waves, launched by vigorous convection in the proto-neutron star, which form shocks and deposit energy into the wind.

In this thesis, we derive a numerical model for examining the effects of such propagating waves on both the dynamics and the nucleosynthetic processes active in the wind. We explore, via parameter studies, the effects of these wave on both neutron- and proton-rich winds, and how potential r- and νp-processes are affected. Finally, we compute the integrated nucleosynthesis from a realistic proto-neutron star evolution to examine the effects of propagating waves on the different stages of nucleosynthesis a time-dependent wind undergoes, and to predict the full nucleosynthetic yield of realistic winds. We find that gravito-acoustic waves propagating through the wind have a substantial impact on both r- and νp-processing, via heating due to shock formation as well as the momentum flux carried by the waves. The combination of these effects also reduces the asymptotic electron fraction of the wind by up to 20%. We even find that, for winds in which the wave luminosity is $\gtrsim$ 1% of the wave luminosity, a third-peak, albeit suppressed, r-process attains despite proton-rich conditions in the wind. Though a full r-process is not realized in the realistic, time-integrated wind from a simulated proto-neutron star, this is likely due to the low-mass ($\sim 1.35\,M_\odot$) neutron star formed. If a heavier (e.g., $1.6\,M_\odot$) proto-neutron star forms with a similar neutrino spectrum and convective properties, our results suggest that a full r-process can proceed.

To my beloved wife, Sarah, and to the saints in Christ at University Reformed Church.

ACKNOWLEDGEMENTS

This work was completed at Michigan State University during the years 2019-2024, with support from a University Distinguished Fellowship and from the College of Natural Sciences. This work was made possible in large part by the computational resources and services provided by the Institute for Cyber-Enabled Research at MSU.

I am deeply grateful to my lovely wife, Sarah, and to my parents for their love and support as I have pursued this goal. Also to my many dear friends and mentors at University Reformed Church, who have refreshed my soul time and again over the last 5 years.

I thank my advisors, Ed Brown and Luke Roberts, for their patience, help and encouragement in completing this work through a complicated advising situation; Luke, for continuing to work with me after moving across the country; and Ed, for adopting me into his research group and taking the time to learn about and help me with my project, which was outside his typical research area. Thanks also to Sean Couch for his hard work getting STIR up and running, and helping put chapter 5 together; to the rest of my committee members, Filomena Nunes, Joey Rodriguez, and Betty Tsang, for their help and support; also to Stan Woosley and Brian Metzger, who provided helpful comments and discussion regarding chapter 3. Further thanks to Kim Crosslan for her invaluable administrative assistance in navigating the PhD program. I am also grateful to my friends and colleagues in the department: Jordan Purcell, Sheng Lee, Erin White, and many others. Thank you to Dr. Amy Kolan, Dr. Prabal Adhikari, and the rest of the physics department at St. Olaf College, who prepared me so well for my time at MSU.

My greatest thanks and praise are to the Lord my God, who has kept me through this journey. He has written His faithfulness into the fixed order of the stars, and His kindness into their beauty.

Jeremiah 31:33-36 (English Standard Version)

"For this is the covenant that I will make with the house of Israel after those days, declares the Lord: I will put my law within them, and I will write it on their hearts. And I will be their God, and they shall be my people. And no longer shall each one teach his neighbor and each his brother, saying, 'Know the Lord,' for they shall all know me, from the least of them to the greatest, declares the Lord. For I will forgive their iniquity, and I will remember their sin no more."

Thus says the Lord,
who gives the sun for light by day
and the fixed order of the moon and the stars for light by night,
who stirs up the sea so that its waves roar—
the Lord of hosts is his name:
"If this fixed order departs
from before me, declares the Lord,
then shall the offspring of Israel cease
from being a nation before me forever."

Psalm 19:1 (English Standard Version)

The heavens declare the glory of God,
and the sky above proclaims his handiwork.

Psalm 148:3 (English Standard Version)

Praise him, sun and moon,
praise him, all you shining stars!

TABLE OF CONTENTS

CHAPTER 1

INTRODUCTION

1.1 Supernovae

After formation, stars maintain their interior temperature against radiative losses by fusing hydrogen into helium. As a massive ($\gtrsim 8\,M_\odot$) star reaches the end of its main-sequence phase, the supply of hydrogen in its core is depleted, and progressively heavier isotopes begin to fuse in its core. Carbon, neon, oxygen, silicon, and finally iron are formed. Burning stalls when the core reaches nuclear statistical equilibrium (NSE), which favors nuclei with high binding energies near the iron peak. Fusing these elements no longer produces energy, and an inert core of iron-peak elements, held up by electron degeneracy pressure, is formed. As fusion continues in the layers surrounding the core, more iron is added, until the core approaches the Chandrasekhar mass. As the core grows, the rising density causes the electrons to become increasingly relativistic, which lowers the adiabatic index γ from the 5/3 of an ideal gas towards 4/3. At the Chandrasekhar mass, when $\gamma = 4/3$, the core becomes mechanically unstable and begins to collapse. The density-sensitive electron-capture reaction rate then increases, and electrons and protons rapidly combine into neutrons. These electron captures further decrease γ and rob the core of support, and the material begins to free fall towards the center of the star as it becomes more and more neutron-rich. The free fall is halted when neutron degeneracy pressure becomes significant; the abrupt stiffening of the core launches a shockwave toward the stellar surface (Weaver et al., 1978; Woosley & Janka, 2005). The shock stalls eventually, but is re-invigorated by the neutrinos released by the ongoing electron captures in the core (Burrows & Vartanyan, 2021). Upon reaching the surface, the shock violently disrupts the star and creates the luminous event observed as a supernova.

This picture describes the process by which a neutron star is formed in a core-collapse supernova (CCSN), and is born out in modern simulations (e.g., Burrows et al., 2019). The collapsing iron core rapidly neutronizes as the extreme density drives electron capture reactions, and neutron degeneracy pressure halts its collapse at a radius of order $\sim 50\,\mathrm{km}$, from an original radius of order $\sim 2000\,\mathrm{km}$ (Couch, 2017). About $10^{53}\,\mathrm{erg}$ of gravitational potential energy are released in

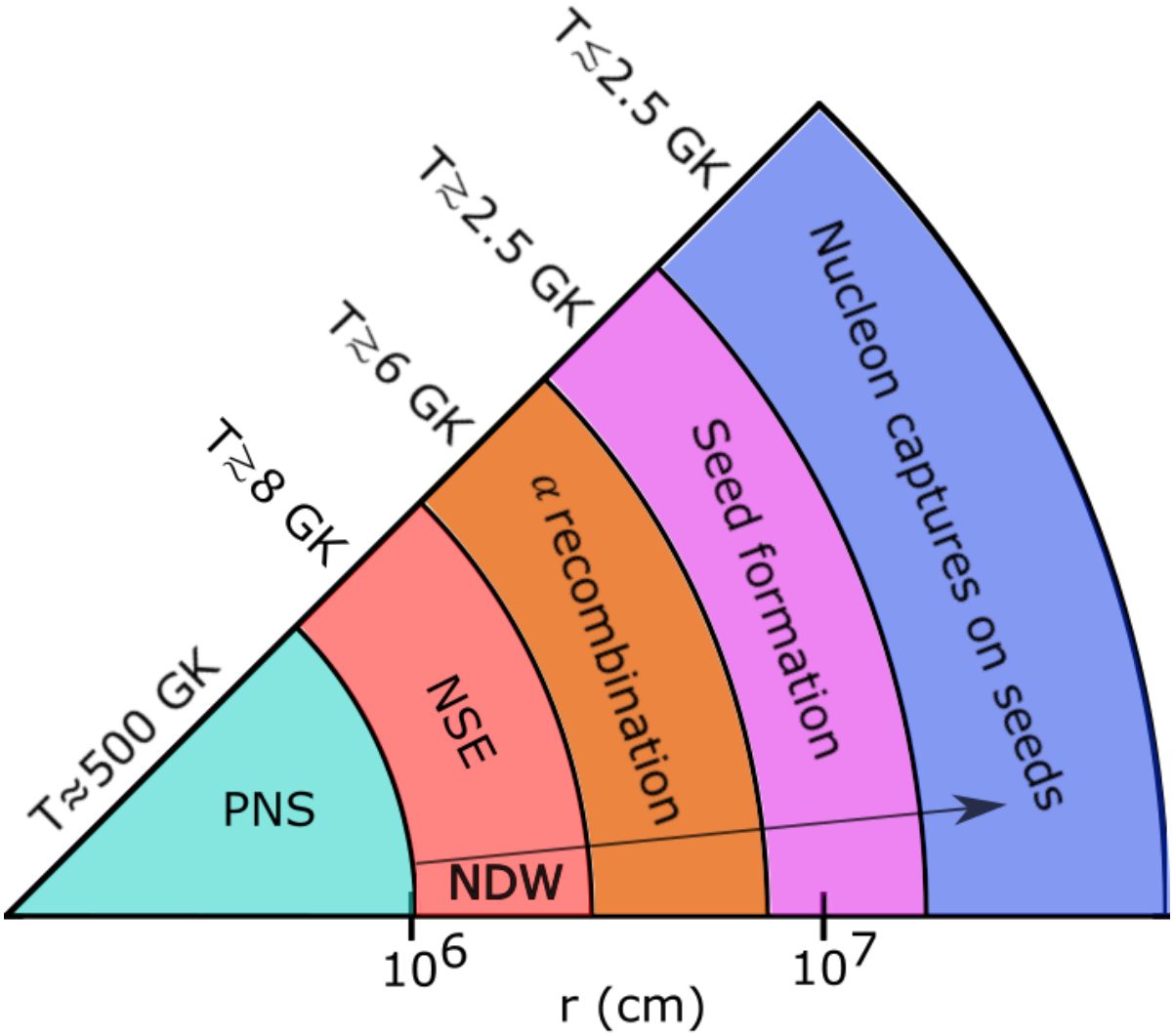

Figure 1.1 Schematic showing the dominant reactions and rough temperature ranges of the various nucleosynthetic stages the NDW undergoes during its outflow. The wind initially is extremely hot, but cools rapidly once it leaves the PNS.

the process, resulting in an extremely hot and dense proto-neutron star (PNS) that is opaque to neutrinos. The PNS then radiates this energy as a massive flux of neutrinos and antineutrinos over the course of ~ 20 s (Qian & Woosley, 1996; Woosley & Janka, 2005), while shrinking towards the fiducial 10 km cold neutron star radius. As the PNS cools, the neutrinosphere (the high temperature region opaque to neutrinos) shrinks until the star is fully transparent to neutrinos and becomes a mature (though hot) neutron star (Camelio, 2018).

1.2 The Neutrino-Driven Wind

As the PNS cools, the immense neutrino flux interacts with its outermost layers and is sufficient to unbind some ($\sim 10^{-3}\,M_\odot$, Wanajo, 2013) material from the surface in what has been called the neutrino-driven wind (NDW, Duncan et al., 1986). Initially, the material in the NDW is hot ($T \sim 3\,\mathrm{MeV}$), dense ($\rho_{\mathrm{PNS}} \sim 10^{12}\,\mathrm{g\,cm^{-3}}$), and neutron-rich (electron fraction $Y_e \lesssim 0.3$) (Qian & Woosley, 1996; Couch, 2017). These conditions are such that the wind material begins in NSE and proceeds through several phases of nucleosynthesis as it cools (see Figure 1.1). While in NSE, the material primarily consists of free protons and neutrons. As the temperature drops below $T \sim 1\,\mathrm{MeV}$, the wind is expected to undergo α-recombination, in which all free nucleons possible are bound into α particles.

As the temperature approaches $T = 0.5\,\mathrm{MeV}$, these α particles combine into successively heavier elements up to the iron peak. The starting point for this process is $3\alpha \rightarrow {}^{12}\mathrm{C}$ or, in neutron-rich conditions, $3\alpha + \mathrm{n} \rightarrow {}^{12}\mathrm{C} + \mathrm{n}$. Neutron-rich conditions are not guaranteed or necessarily even expected at this point; the electron fraction in the wind is altered significantly by charged-current neutrino and antineutrino reactions during these initial moments while the material is close to the PNS surface. The neutrino spectrum of the PNS is the most important factor in determining the asymptotic electron fraction of the wind. Assuming other factors are negligible, the equilibrium electron fraction in the wind is reached when $T \approx 1$ MeV and is (Qian & Woosley, 1996)

$$Y_{e,\mathrm{eq}} \approx \left[1 + \frac{L_{\bar{\nu}_e}\left(\epsilon_{\bar{\nu}_e} - 2\Delta + 1.2\Delta^2/\epsilon_{\bar{\nu}_e}\right)}{L_{\nu_e}\left(\epsilon_{\nu_e} + 2\Delta + 1.2\Delta^2/\epsilon_{\nu_e}\right)}\right] \tag{1.1}$$

where L_{ν_e} and $L_{\bar{\nu}_e}$ denote the electron neutrino and antineutrino luminosities respectively, the ϵ_ν denote the electron neutrino and antineutrino energies in MeV, and Δ represents the positive mass difference between protons and neutrons, approximately equal to 1.293 MeV. Most modern simulations predict a very slightly neutron-rich or proton-rich NDW, with $0.45 \lesssim Y_{e,\mathrm{eq}} \lesssim 0.65$ (e.g., Fischer et al., 2010; Roberts et al., 2012a; Hüdepohl, 2013; Martínez-Pinedo et al., 2014; Xiong et al., 2020; Pascal et al., 2022). As the range suggests, there is significant uncertainty in $Y_{e,\mathrm{eq}}$.

The efficiency of this α-process, and specifically the 3- and 4- body reactions that form the initial ${}^{12}\mathrm{C}$ nuclei, determine the character of the nucleosynthesis going forward. Once the wind

cools below $T \approx 5$ GK, α capture reactions freeze out, and nucleosynthesis is dominated by nucleon captures onto the heavy ($A \geq 12$) nuclei formed by the α-process. The number and type of free nucleons in the wind is determined by the electron fraction, and the number of capture targets is set by the efficiency of the α-process. If a large number of heavy nuclei were formed, the free nucleons are spread thinly and nucleosynthesis remains concentrated near the iron peak. If the α-process were inefficient and only a few heavy nuclei were formed, each one could undergo a large number of nucleon captures to build much heavier nuclei as the wind continues outward.

Two main parameters, the entropy (s) and the dynamical timescale (τ_d), determine the efficiency of the α-process (Hoffman et al., 1997). The ^{12}C nuclei are formed via 3- and 4-body reactions which are highly dependent on both density and temperature. These seed nuclei are formed when $T \approx 0.5$ MeV, and at a fixed temperature, a higher entropy corresponds to a lower density. High entropies therefore inhibit seed formation by suppressing the ^{12}C-forming reaction rates. The dynamical timescale of the wind (defined here as $\tau_d = T/\dot{T}$, similar to the $r/\dot{r}$ of Qian & Woosley, 1996) describes how quickly the wind is expanding outwards, and is a helpful indicator of how quickly the wind is cooling. Temperatures in excess of 2.5 GK are required to facilitate the α-capture reactions that form the heavy seed nuclei, and a fast expansion (i.e., a short dynamical timescale) means the wind material will move through this temperature range much faster. The reaction rate is not necessarily affected, but the amount of time over which the reactions can take place is diminished. In the case of a neutron-rich wind ($Y_e < 0.5$), the neutron-catalyzed $3\alpha + \mathrm{n} \rightarrow {}^{12}\mathrm{C} + \mathrm{n}$ becomes the dominant seed-forming channel, and so the electron fraction enters as a third parameter determining the efficiency of the α-process. A higher abundance of free neutrons allows for more efficient seed formation.

Once the wind cools below 2.5 GK, α capture reactions freeze out, and subsequent nucleosynthesis depends primarily on the electron fraction of the wind. At this point, the wind material comprises free nucleons (either protons or neutrons), α particles, and whatever heavy seed nuclei were formed in the α-process. At these temperatures, the α particles are essentially inert, and nucleosynthesis is driven by nucleon captures onto the seed nuclei. This can proceed via two

general branches depending on the electron fraction. If the wind is neutron-rich, neutron captures and subsequent β-decays proceed freely, building heavier elements from the initial seed nuclei in an r-process (Burbidge et al., 1957). If the wind is proton-rich, the νp-process operates, building heavier nuclides via proton captures facilitated by a small abundance of free neutrons created *in-situ* by charged-current neutrino reactions (Fröhlich et al., 2006). How far these processes can proceed (i.e., the heaviest elements that can be synthesized) depends mainly on the ratio of free nucleons to seed nuclei, which is set by the electron fraction and the efficiency of the α-process. Naturally, then, most research on the NDW in recent decades has focused on these two factors. Much work has been done to explore the neutrino spectrum of a cooling PNS, and the electron fraction it predicts in the wind (e.g. Hüdepohl et al., 2010; Roberts, 2012; Roberts et al., 2012a; Martínez-Pinedo et al., 2012; Hüdepohl, 2013; Martínez-Pinedo et al., 2014; Xiong et al., 2019, 2020). This work joins the body of literature studying the variety of phenomena that affect the efficiency of the α-process, and the subsequent nucleosynthesis.

1.2.1 Physical Phenomena Affecting NDW Nucleosynthesis

The efficiency of the α-process depends mainly on the entropy and the dynamical timescale of the wind, as described above. The asymptotic entropy of the wind is individually affected by a number of factors. It scales positively with PNS mass and inversely with the neutrino luminosity L_ν (Thompson et al., 2001). The inclusion of general relativistic effects therefore has a substantially positive effect on entropy (Cardall & Fuller, 1997; Otsuki et al., 2000; Wanajo, 2013). Strong (magnetar-strength) magnetic fields have been a subject of much study; they tend to increase entropy by trapping material closer to the neutron star, thereby increasing the neutrino heating the material receives (Thompson, 2003). The wind termination shock, when the fast-moving wind material impacts slower-moving material behind the primary supernova shock, can also affect nucleosynthesis based on the radius and temperature at which it occurs. A termination shock close to the PNS can dramatically increase the amount of neutrino heating the material receives, raising the entropy, but will also greatly increase the dynamical timescale (Arcones et al., 2007; Arcones & Thielemann, 2012). The most-studied factor affecting the dynamical timescale of the wind is

PNS rotation, which provides an additional centrifugal acceleration to the wind material (Metzger et al., 2007).

The focus of this work is a phenomenon that can affect both the entropy and the dynamical timescale of the wind simultaneously: the generation of waves propagating through the wind. Suzuki & Nagataki (2005) considered Alfvén waves generated by strong magnetic fields; our focus is the more ubiquitous phenomenon of gravito-acoustic waves briefly considered by Metzger et al. (2007). These waves are generated by convection in the PNS, which has been shown to be common across a broad range of progenitors (e.g., Nagakura et al., 2020; Nagakura et al., 2021), unlike the magnetar-strength magnetic fields required for significant Alfvén wave generation. PNS convection is predicted to be most vigorous 1–2 seconds post-bounce, and gradually tapering off thereafter. The convective region in the outer layers of the PNS launches density waves into the adjacent radiative region, the outflowing wind, and these waves continue to propagate outward in the wind. Gravity, acoustic, and non-propagating wave modes will all be excited, but the energy flux will be dominated by the gravity mode branch (Goldreich & Kumar, 1990). The luminosity carried by the gravity waves is approximately

$$L_g \approx M_{\rm con} L_{\rm con} \approx M_{\rm con} L_\nu, \tag{1.2}$$

where $M_{\rm con}$ is the convective Mach number in the PNS convective zone, $L_{\rm con}$ is the convective luminosity, and L_ν is the total neutrino luminosity of the PNS. Convection in the PNS is expected to be efficient, so $L_{\rm con} \approx L_\nu$. Simulations by Dessart et al. (2006) and Gossan et al. (2020) indicate that $10^{-2} \lesssim M_{\rm con} \lesssim 10^{-1}$. Though the waves begin primarily in the gravity mode branch, they will encounter an evanescent region close to the surface of the PNS. They will tunnel through this region with some efficiency $\mathcal{T}$, emerging in the acoustic wave branch and continuing out into the wind (see figure 1.2). The total wave luminosity actually reaching the wind is then given by

$$L_w \approx M_{\rm con} \mathcal{T} L_\nu. \tag{1.3}$$

Simulations by Gossan et al. (2020) indicate that $0.01 \lesssim \mathcal{T} \lesssim 0.2$ in the pre-supernova explosion environment, and our models find similar values in the NDW phase (see chapter 5). The wave

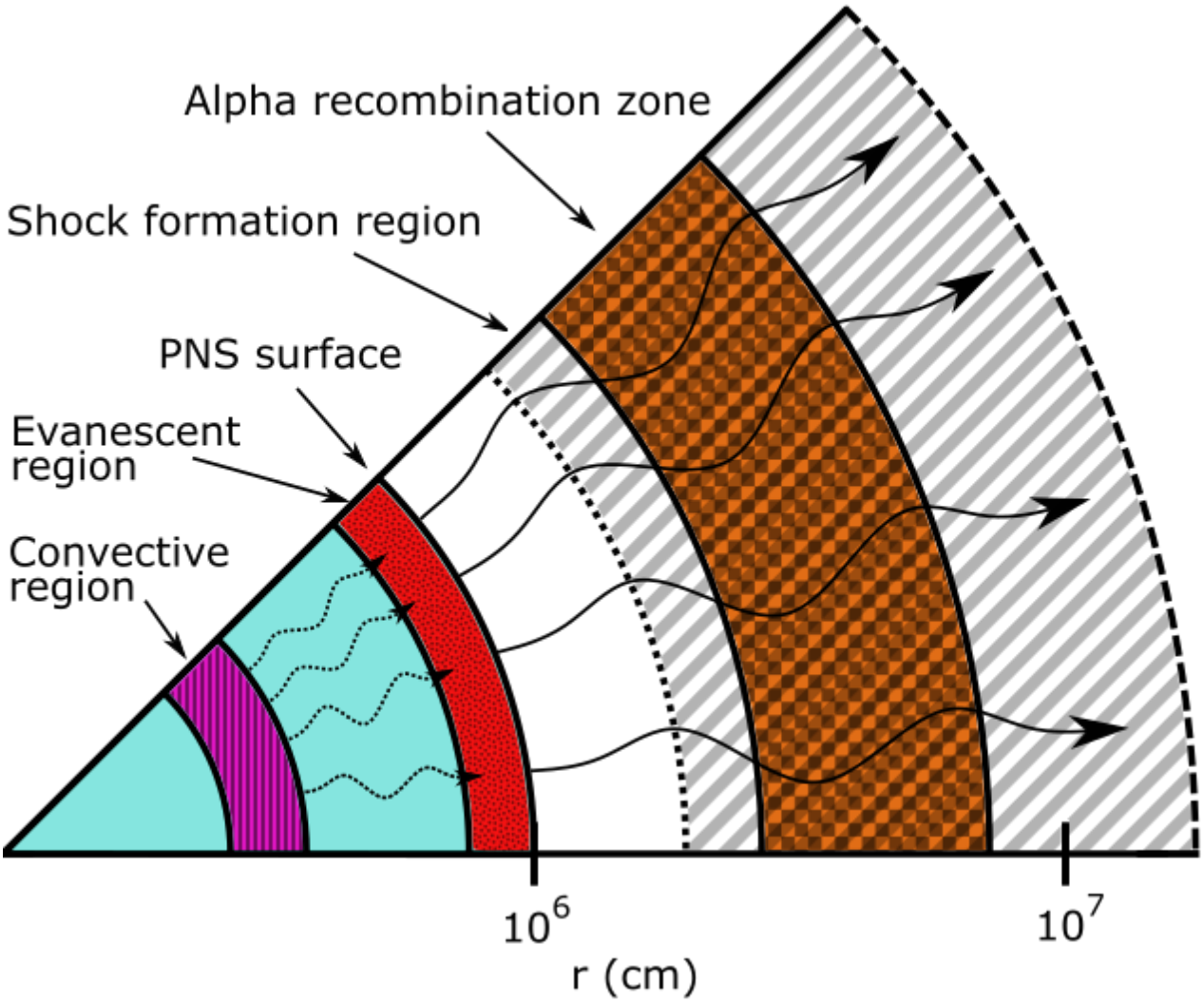

Figure 1.2 An approximate schematic of gravito-acoustic wave emission and propagation inside and near the PNS. Gravity waves (dashed) are generated by the convective region, attenuate in the evanescent region, and re-emerge as acoustic waves (solid) near the surface of the PNS. They then propagate outward through the wind until they form shocks and dissipate. The region of possible shock formation and heat deposition overlaps with the α-forming region. If the waves shock before or during α recombination, the additional heating will inhibit seed formation, making a strong r-process more likely.

luminosity can therefore reasonably fall in the range of 10^{-5} to 10^{-2} L_ν, enough to significantly alter the dynamics of the wind. Wave angular frequencies of 10^2 to 10^4 s^{-1} are expected, and tend to increase with time. If information about the convective velocity of the PNS is known, L_w and ω can be calculated explicitly (see chapter 5).

As the waves propagate through the wind, they impose two main effects. First, these waves carry momentum, and this momentum flux accelerates the wind and reduces the dynamical timescale. Second, due to the density dependence of the sound speed (c_s), the peaks of these waves travel slightly faster than the troughs. Eventually, the waves become non-linear and form shocks, which efficiently deposit their energy into the wind as heat (Mihalas & Mihalas, 1984). This acts to raise the entropy of the wind. Depending on how long it takes these shocks to form, this heat could be deposited while the α-process is ongoing or after it has already ended. In the latter case, this additional heating will have little if any effect on the nucleosynthesis in the wind. In the former, however, it could substantially affect the efficiency of the α-process. A third effect emerges as a consequence of these two primary effects: the additional energy and momentum deposited by the waves reduces the amount of neutrino heating experienced by the material as it is ejected, which in turn affects Y_e. The material is initially extremely neutron-rich, and the neutrino heating it experiences drives it toward $Y_e = 0.5$. This reduction in neutrino heating causes the material to remain more neutron-rich than the neutrino spectrum of the PNS would predict. This also reduces the asymptotic entropy of the wind prior to shock heating, as neutrino heating is the primary source of entropy in the wind.

The objective of this work is to determine how the presence of gravito-acoustic waves affects nucleosynthesis in the NDW, in both the neutron-rich and proton-rich branches. The mathematical formalism and modeling methods used to this end are described in chapter 2. In chapters 3 and 4, a brief history of the r-process and νp-process in the NDW is provided, and the impact of gravito-acoustic waves on these processes is described. Finally, in chapter 5 the total, time-integrated nucleosynthetic yield of a NDW derived from a self-consistent supernova simulation is explored.

CHAPTER 2

MATHEMATICAL FORMALISM AND MODELING METHOD

While a supernova is an inherently three-dimensional event, with turbulence and stellar anisotropies playing vital roles, the computational power and complexity required to simulate these events in 3D can be prohibitive. There have been many fruitful efforts to model supernovae generally (e.g., O'Connor, 2015; Curtis et al., 2018; Couch et al., 2020), and the NDW specifically (e.g., Qian & Woosley, 1996; Thompson et al., 2001; Wanajo et al., 2001), in spherical symmetry. The reduced complexity of a spherically symmetric model allows for large parameter studies such as the ones described in chapters 3 and 4, and is the most commonly used tool for examining the NDW.

A further approximation of time-independence is also often used when modeling the NDW. After the supernova shock has been launched and during the cooling phase of the PNS (while the wind is being launched), both the physical properties and the neutrino spectrum of the PNS vary slowly compared to the dynamical timescale of the wind, which makes such a steady-state treatment reasonable. This steady-state assumption reduces the equations describing the wind to depend only on the properties of the PNS, the local conditions and equation of state of the wind, and the radial distance of a fluid element in the wind from the PNS.

2.1 Fundamental Equations of the Neutrino-Driven Wind

The NDW is described by the equations of inviscid hydrodynamics. We denote the velocity, density, pressure, and specific internal energy of the wind with $\vec{v}$, ρ, P, and ϵ respectively. The equations for conservation of mass, momentum, and energy, including the energy and momentum of the propagating waves (Jacques, 1977), are respectively

$$\frac{\partial \rho}{\partial t} + \nabla \cdot (\rho \vec{v}) = 0 \tag{2.1}$$

$$\frac{\partial}{\partial t}(\rho \vec{v}) + \nabla \cdot (\mathbf{T} + \mathbf{\Pi}) = \rho \vec{g} \tag{2.2}$$

$$\frac{\partial}{\partial t}\left[\rho\left(\epsilon + \frac{1}{2}v^2 + \Phi\right) + \mathcal{E}\right] + \nabla \cdot \left[\rho \vec{v}\left(h + \frac{1}{2}v^2 + \Phi\right) + \vec{v}_g \mathcal{E} + \mathbf{\Pi} \cdot \vec{v}\right] = \rho \dot{q}_\nu \tag{2.3}$$

with the ideal fluid stress tensor $\mathbf{T}$ given by

$$T_{ij} = P\delta_{ij} + \rho v_i v_j. \tag{2.4}$$

Here $h = \epsilon + P/\rho$ is the specific enthalpy, Φ is the Newtonian gravitational potential, and $\vec{g}$ is the Newtonian gravitational acceleration. The energy density and stress tensor of the waves are $\mathcal{E}$ and $\mathbf{\Pi}$, respectively. The volumetric heating rate per unit mass due to neutrino interactions is denoted by $\dot{q}_\nu$; as is customary in studies of the NDW, we neglect the momentum flux of the neutrinos as it is expected to be negligible (e.g., Qian & Woosley, 1996). By expanding equations (2.2) and (2.3), using equation (2.1) to eliminate terms, subtracting the dot product of $\vec{v}$ with equation (2.2) from equation (2.3), and taking $\partial\Phi/\partial t = 0$, we reduce equations (2.1)–(2.3) to Lagrangian form:

$$\frac{D\rho}{Dt} = -\rho\nabla\cdot\vec{v} \tag{2.5}$$

$$\frac{D\vec{v}}{Dt} = -\frac{1}{\rho}\nabla P - \frac{1}{\rho}\nabla\cdot\mathbf{\Pi} - \vec{g} \tag{2.6}$$

$$\frac{D\epsilon}{Dt} = -P\frac{D}{Dt}\left(\frac{1}{\rho}\right) - \frac{1}{\rho}\left[\frac{\partial\mathcal{E}}{\partial t} + \nabla\cdot\left(\vec{v}_g\mathcal{E} + \mathbf{\Pi}\cdot\vec{v}\right)\right] + \vec{v}\cdot\nabla\cdot\mathbf{\Pi} + \dot{q}_\nu. \tag{2.7}$$

We use the notation

$$\frac{D}{Dt} \equiv \frac{\partial}{\partial t} + \vec{v}\cdot\nabla$$

to denote the material (or convective) derivative, which describes the Lagrangian change in a quantity moving with velocity $\vec{v}$. No source term for mass exists in the outflowing wind, so the evolution of density is determined strictly by the divergence of the velocity. The velocity is determined by the internal thermodynamic state of the wind, but is also affected by gravity and stresses exerted by the waves. The specific internal energy of the wind can be converted into kinetic energy as the pressure does work on the wind material, and can also be affected by changes in the energy of the waves due to, e.g., shock formation, and by neutrino interactions that heat or cool the wind. Since several of these equations depend on the wave treatment, we will consider that first, before addressing each of these equations in turn.

2.1.1 Gravito-Acoustic Wave Propagation

In this work, we follow Jacques (1977) in treating the waves in the eikonal approximation. In this approximation, while the energy density of the waves is not conserved due to adiabatic losses, the number density of wave quanta (often referred to as the wave action) $\mathcal{N} = \mathcal{E}/\omega_0$ is conserved

in the absence of dissipation, i.e.,

$$\frac{\partial \mathcal{N}}{\partial t} + \nabla \cdot (\vec{v}_g \mathcal{N}) = 0. \tag{2.8}$$

Here $\omega_0 = \omega c_s / v_g$ denotes the wave frequency in the fluid frame, with c_s and ω representing the sound speed and the wave frequency in the rest frame of the PNS, and $\vec{v}_g = \vec{v} + c_s \vec{e}_k$ being the group velocity. When dissipation is present, we parameterize the energy loss, and thus the change in the wave action, with a characteristic dissipation length l_d:

$$\frac{\partial \mathcal{N}}{\partial t} + \nabla \cdot (\vec{v}_g \mathcal{N}) = -\frac{v_g \mathcal{N}}{l_d}. \tag{2.9}$$

In this treatment, the wave frequency ω is constant along a ray,

$$\frac{\partial \omega}{\partial t} + \vec{v}_g \cdot \nabla \omega = 0; \tag{2.10}$$

thus in steady-state and spherical symmetry, the wave frequency in the PNS frame is constant. With these approximations, we can now examine the hydrodynamic equations.

2.1.2 Mass Conservation

The mass conservation equation can be integrated to provide an expression for the mass-loss rate from the PNS due to the wind. Rewriting equation (2.1) in the steady-state approximation, we have

$$\nabla \cdot (\rho \vec{v}) = 0.$$

Integrating over a sphere of radius r, assuming spherical symmetry, and applying Gauss's law, this becomes

$$\int_V \nabla \cdot (\rho \vec{v}) d^3 r = \oint_A \rho v d^2 r = 4\pi r^2 v \rho = C. \tag{2.11}$$

The integration constant C is immediately recognizable as the mass-loss rate of the PNS due to the wind:

$$\dot{M} = 4\pi r^2 v \rho. \tag{2.12}$$

The steady-state approximation thus essentially states that the mass-loss rate is constant in the wind.

2.1.3 Momentum Conservation

The momentum conservation equation can be expanded in the following way. Applying the one-dimensional and steady-state approximations transforms the material derivative to

$$\frac{D}{Dt} = v\frac{d}{dr}. \tag{2.13}$$

With this transformation, Equation (2.6) becomes

$$v\frac{dv}{dr} = -\frac{1}{\rho}\frac{dP}{dr} - \frac{1}{\rho}(\nabla \cdot \mathbf{\Pi} + \rho\vec{g}) \cdot \vec{e}_r. \tag{2.14}$$

The stress tensor for radially propagating acoustic waves is (Jacques, 1977)

$$\mathbf{\Pi} = \begin{pmatrix} \Pi_{rr} & 0 & 0 \\ 0 & \Pi_{\theta\theta} & 0 \\ 0 & 0 & \Pi_{\phi\phi} \end{pmatrix} = \mathcal{E}\begin{pmatrix} a_1 & 0 & 0 \\ 0 & a_2 & 0 \\ 0 & 0 & a_3 \end{pmatrix}, \tag{2.15}$$

where $\mathcal{E}$ is again the energy density of the waves, and

$$\begin{aligned} a_1 &= \frac{1}{2}(\gamma + 1), \\ a_2 = a_3 &= \frac{1}{2}(\gamma - 1). \end{aligned} \tag{2.16}$$

Here $\gamma \equiv (\partial \ln P / \partial \ln \rho)_s$ is the adiabatic index. The divergence of $\mathbf{\Pi}$ in spherical symmetry, i.e., the (negative) effective force exerted by the waves on a fluid element, is (assuming constant γ)

$$\begin{aligned} \nabla \cdot \mathbf{\Pi} &= \left[\frac{1}{r^2}\frac{\partial}{\partial r}\left(r^2\Pi_{rr}\right) - \frac{\Pi_{\theta\theta} + \Pi_{\phi\phi}}{r}\right]\vec{e}_r + \left[\frac{1}{r\sin\theta}\frac{\partial}{\partial\theta}(\Pi_{\theta\theta}\sin\theta) - \frac{\Pi_{\phi\phi}\cot\theta}{r}\right]\vec{e}_\theta \\ &= \left[\frac{\partial\Pi_{rr}}{\partial r} + \frac{2\Pi_{rr} - \Pi_{\theta\theta} - \Pi_{\phi\phi}}{r}\right]\vec{e}_r \\ &= \left[a_1\frac{\partial\mathcal{E}}{\partial r} + \frac{2\mathcal{E}}{r}\right]\vec{e}_r. \end{aligned}$$

The equality of the transverse components $\Pi_{\theta\theta}$ and $\Pi_{\phi\phi}$ ensures that $\nabla \cdot \mathbf{\Pi}$ is purely radial. With $\vec{g} = (GM/r^2)\vec{e}_r$, the spherically symmetric, steady-state momentum conservation equation (2.6) thus becomes

$$v\frac{dv}{dr} = -\frac{1}{\rho}\frac{dP}{dr} - \frac{GM}{r^2} - \frac{a_1}{\rho}\frac{d\mathcal{E}}{dr} - \frac{2\mathcal{E}}{\rho r}. \tag{2.17}$$

Most prior work on the NDW only includes the pressure and gravitational terms; the others arise specifically from wave contributions.

To describe the evolution of the energy density of the waves, recalling that $\mathcal{E} = \omega_0 \mathcal{N}$, we make use of equation (2.9) in the steady-state approximation:

$$\nabla \cdot (\vec{v}_g \mathcal{N}) = -\frac{v_g \mathcal{N}}{l_d}, \tag{2.18}$$

which is again analogous to the conservation of quantized wave packets. For non-dissipative waves, $l_d \to \infty$ and $\mathcal{N}$ is conserved. The process by which the waves become dissipative is described in section 2.1.4.2 below. Expanding and solving for $d\mathcal{N}/dr$ in spherical symmetry, equation (2.18) becomes

$$\frac{d\mathcal{N}}{dr} = -\mathcal{N}\left(\frac{1}{l_d} + \frac{2}{r} + \frac{1}{v_g}\frac{dv_g}{dr}\right). \tag{2.19}$$

Note that, for the sake of simplifying computation, equation (2.19) can be written in terms of $\mathcal{L} = 4\pi r^2 v_g \omega \mathcal{N}$ as

$$\frac{d\ln \mathcal{L}}{dr} = -\frac{1}{l_d}. \tag{2.20}$$

$\mathcal{L}$ can be thought of as an effective wave luminosity remaining in the wind at a given radius, and thus accounts for any dissipation that has taken place. In the absence of dissipation ($l_d \to \infty$), $\mathcal{L}$ is a conserved quantity. For the wave energy density, we now have

$$\frac{d\mathcal{E}}{dr} = \omega_0 \frac{d\mathcal{N}}{dr} + \mathcal{N}\frac{d\omega_0}{dr} = \omega \mathcal{N}\frac{c_s}{v_g}\left(\frac{1}{c_s}\frac{dc_s}{dr} - \frac{1}{l_d} - \frac{2}{r} - \frac{2}{v_g}\frac{dv_g}{dr}\right). \tag{2.21}$$

We can then rewrite equation (2.17) as

$$\begin{aligned} v\frac{dv}{dr} &= -\frac{1}{\rho}\frac{dP}{dr} - \frac{GM}{r^2} - \frac{a_1 c_s \omega \mathcal{N}}{\rho v_g}\left[\frac{1}{c_s}\frac{dc_s}{dr} - \frac{1}{l_d} - \frac{2}{r}\left(1 - \frac{1}{a_1}\right) - \frac{2}{v_g}\frac{dv_g}{dr}\right] \\ &= -\frac{P}{\rho}\frac{d\ln P}{dr} - \frac{GM}{r^2} - \frac{a_1 c_s \omega \mathcal{N}}{\rho v_g}\left[\frac{d\ln c_s}{dr} - \frac{1}{l_d} - \frac{2}{r}\left(1 - \frac{1}{a_1}\right) - \frac{2}{v_g}\left(c_s\frac{d\ln c_s}{dr} + \frac{dv}{dr}\right)\right]. \end{aligned} \tag{2.22}$$

It will be helpful to cast the derivatives of pressure and sound speed in terms of density, entropy, and electron fraction:

$$\begin{aligned}\frac{d\ln P}{dr} &= \frac{1}{s}\left(\frac{\partial \ln P}{\partial \ln s}\right)_{\rho,Y_e}\frac{ds}{dr} + \frac{1}{\rho}\left(\frac{\partial \ln P}{\partial \ln \rho}\right)_{s,Y_e}\frac{d\rho}{dr} + \frac{1}{Y_e}\left(\frac{\partial \ln P}{\partial \ln Y_e}\right)_{s,\rho}\frac{dY_e}{dr} \\ &= \frac{\Gamma^{Ps}_{\rho Y_e}}{s}\frac{ds}{dr} - \frac{\rho c_s^2}{P}\left(\frac{2}{r} + \frac{1}{v}\frac{dv}{dr}\right) + \frac{\Gamma^{PY_e}_{s\rho}}{Y_e}\frac{dY_e}{dr} \qquad (2.23)\end{aligned}$$

$$\begin{aligned}\frac{d\ln c_s}{dr} &= \frac{1}{s}\left(\frac{\partial \ln c_s}{\partial \ln s}\right)_{\rho,Y_e}\frac{ds}{dr} + \frac{1}{\rho}\left(\frac{\partial \ln c_s}{\partial \ln \rho}\right)_{s,Y_e}\frac{d\rho}{dr} + \frac{1}{Y_e}\left(\frac{\partial \ln c_s}{\partial \ln Y_e}\right)_{s,\rho}\frac{dY_e}{dr} \\ &= \frac{\Gamma^{c_s s}_{\rho Y_e}}{s}\frac{ds}{dr} - \Gamma^{c_s\rho}_{sY_e}\left(\frac{2}{r} + \frac{1}{v}\frac{dv}{dr}\right) + \frac{\Gamma^{c_s Y_e}_{sY_e}}{Y_e}\frac{dY_e}{dr}, \qquad (2.24)\end{aligned}$$

with $\Gamma^{wx}_{yz} = (\partial \ln w/\partial \ln x)_{y,z}$. Substituting these into equation (2.22) and solving for dv/dr yields the critical form of the momentum conservation equation,

$$\begin{aligned}\left[v^2 - c_s^2 + \frac{a_1 v c_s \omega \mathcal{N}}{\rho v_g}\left(\frac{c_s - v}{v}\Gamma^{c_s\rho}_{sY_e} - 2\right)\right]\frac{dv}{dr} &= -\frac{v}{\rho}\left(\frac{P}{s}\Gamma^{Ps}_{\rho Y_e}\frac{ds}{dr} + \frac{P}{Y_e}\Gamma^{PY_e}_{s\rho}\frac{dY_e}{dr}\right) + \frac{v}{r}\left(2c_s^2 - \frac{GM}{r}\right) \\ &+ \frac{a_1 v c_s \omega \mathcal{N}}{\rho v_g}\left[\frac{c_s - v}{v_g}\left(\frac{1}{s}\Gamma^{c_s s}_{\rho Y_e}\frac{ds}{dr} + \frac{1}{Y_e}\Gamma^{c_s Y_e}_{s\rho}\frac{dY_e}{dr} - \frac{2}{r}\Gamma^{c_s\rho}_{sY_e}\right) + \frac{1}{l_d} + \frac{2}{r}\left(1 - \frac{1}{a_1}\right)\right]. \qquad (2.25)\end{aligned}$$

This form clearly shows the singularity, or critical point, in the momentum equation. In the absence of wave effects (i.e., $\mathcal{N} = 0$), the singularity occurs when $v = c_s$, as shown by Thompson et al. (2001). To obtain a physical wind solution, the right-hand side of the critical form equation must go through zero exactly when $v = c_s$. The inclusion of wave effects modifies the location of the critical point but does not remove it. To simplify notation, we introduce the dimensionless f functions:

$$\begin{aligned} f_1 &= 1 - \frac{v^2}{c_s^2}, \\ \delta f_1 &= -\frac{a_1 \omega \mathcal{N}}{\rho c_s v_g}\left(\frac{c_s - v}{v}\Gamma^{c_s\rho}_{sY_e} - 2\right), \\ f_2 &= \frac{r}{\rho c_s^2}\left(\frac{P}{s}\Gamma^{Ps}_{\rho Y_e}\frac{ds}{dr} + \frac{P}{Y_e}\Gamma^{PY_e}_{s\rho}\frac{dY_e}{dr}\right) - 2 + \frac{GM}{r c_s^2}, \\ \delta f_2 &= -\frac{a_1 r \omega \mathcal{N}}{\rho c_s v_g}\left[\frac{c_s - v}{v_g}\left(\frac{1}{s}\Gamma^{c_s s}_{\rho Y_e}\frac{ds}{dr} + \frac{1}{Y_e}\Gamma^{c_s Y_e}_{s\rho}\frac{dY_e}{dr} - \frac{2}{r}\Gamma^{c_s\rho}_{sY_e}\right) + \frac{1}{l_d} + \frac{2}{r}\left(1 - \frac{1}{a_1}\right)\right], \qquad (2.26)\end{aligned}$$

so that equation (2.25) becomes

$$(f_1 + \delta f_1)\frac{d\ln v}{d\ln r} = f_2 + \delta f_2, \qquad (2.27)$$

where the wave contributions are entirely contained in the δ-terms.

2.1.4 Energy Conservation

The energy conservation equation can also be expanded. In steady-state and spherical symmetry, equation (2.7) becomes

$$v\frac{d\epsilon}{dr} = -vP\frac{d}{dr}\left(\frac{1}{\rho}\right) - \frac{1}{\rho}\left[\nabla\cdot\left(\vec{v}_g\mathcal{E} + \mathbf{\Pi}\cdot\vec{v}\right) - \vec{v}\cdot\nabla\cdot\mathbf{\Pi}\right] + \dot{q}_\nu. \tag{2.28}$$

The total derivative of the specific internal energy is given by the first law of thermodynamics, $d\epsilon = Tds - Pd(1/\rho)$, so equation (2.28) becomes

$$v\frac{ds}{dr} = -\frac{1}{\rho T}\left[\nabla\cdot\left(\vec{v}_g\mathcal{E} + \mathbf{\Pi}\cdot\vec{v}\right) - \vec{v}\cdot\nabla\cdot\mathbf{\Pi}\right] + \frac{\dot{q}_\nu}{T}. \tag{2.29}$$

Evaluating the wave stress terms, this becomes

$$v\frac{ds}{dr} = -\frac{1}{\rho T}\left[\nabla\cdot\left(\vec{v}_g\mathcal{E}\right) - \frac{1}{2}(\gamma+1)\mathcal{E}\frac{dv}{dr} - (\gamma-1)\frac{\mathcal{E}v}{r}\right] + \frac{\dot{q}_\nu}{T}. \tag{2.30}$$

This equation shows the two main energy sources in the wind. One of these, neutrino heating, is necessarily included in every similar model of the NDW. Neutrinos interacting with the wind material, primarily via the charged-current $\nu_e + n \rightarrow p + e^-$ and $\bar{\nu}_e + n \rightarrow p + e^-$ reactions, deposit some of their energy as heat. This is the dominant energy source in the wind. Wave effects will also contribute to heating the wind, via shock heating and also via the wave stress. Applying equation (2.18), this becomes

$$\begin{aligned} v\frac{ds}{dr} = \frac{v_g\mathcal{E}}{\rho T}\Bigg[&\left(\frac{1}{l_d} + \frac{d\ln\omega_0}{dr}\right) \\ &+ \left(\frac{d\ln v_g}{dr} - \frac{d\ln c_s}{dr} + \frac{\gamma+1}{2v_g}\frac{dv}{dr} + \frac{(\gamma-1)v}{rv_g}\right)\Bigg] + \frac{\dot{q}_\nu}{T}. \end{aligned} \tag{2.31}$$

In the isentropic limit, i.e., $l_d \rightarrow \infty$ and $\dot{q} \rightarrow 0$, it can be shown that the logarithmic terms exactly cancel with the wave stress terms, so that $ds/dr = 0$ self-consistently. This also ensures that, in the absence of dissipation prior to shock formation, there is negligible change in entropy due to the waves. Because the waves shock well before the transonic point in our simulations, $v \ll c_s$, $v_g \approx c_s$, and $\omega_0 \approx \omega$ at the relevant radii, so the derivatives of v_g and c_s cancel, the derivative of ω_0

vanishes, and the wave stress terms will be negligible. For computational simplicity, therefore, we neglect all but the dissipation length term, which will be dominant when shock formation occurs. Doing so will only lower the entropy of the wind, so our results in this work should be considered a lower bound on the wind entropy and ensuing nucleosynthesis. Inserting the definition of $\mathcal{N}$, this leaves us with

$$v\frac{ds}{dr} = \frac{c_s}{\rho T l_d}\omega\mathcal{N} + \frac{\dot{q}_\nu}{T} \tag{2.32}$$

as the final form of the entropy equation. The remaining heating terms, from neutrinos and from wave shocks, will be examined further in turn.

2.1.4.1 Neutrino heating and cooling

The primary energy source in the wind is heating by neutrinos. The derivation of the reaction and heating/cooling rates is quite involved, and rather than attempting to repeat it, we refer the reader to appendix C of Lippuner & Roberts (2017). Neutrino and antineutrino capture reactions will heat the wind, as the energy of the (anti) neutrino is added to the wind material. (Anti) neutrino emission reactions, on the other hand, will cool the wind. The net neutrino heating is given by

$$\dot{q}_\nu = (\dot{q}_{\bar{\nu}_e} - \dot{q}_{e^-})Y_p + (\dot{q}_{\nu_e} - \dot{q}_{e^+})Y_n. \tag{2.33}$$

The $\dot{q}_i$ represent the heating/cooling rates[1] due to the following charged-current neutrino reactions:

$$\begin{aligned} \nu_e + n &\longleftrightarrow e^- + p \\ \bar{\nu}_e + p &\longleftrightarrow e^+ + n. \end{aligned} \tag{2.34}$$

Because the neutrino flux experienced by the wind falls off as r^2, the heating rates (and thus the entropy deposition) are very high while the wind is close to the PNS surface. Cooling via neutrino emission is fairly weak throughout the wind, so if only neutrino heating contributions are considered, the entropy of the wind quickly reaches an asymptotic value. Because the electron fraction of the wind also asymptotes early (as discussed in section 2.1.5), we approximate $Y_p = Y_e$ and $Y_n = 1 - Y_e$, which yields

$$\dot{q}_\nu = (\dot{q}_{\nu_e} - \dot{q}_{e^+}) + (\dot{q}_{\bar{\nu}_e} + \dot{q}_{e^+} - \dot{q}_{e^-} - \dot{q}_{\nu_e})Y_e \tag{2.35}$$

[1] We have made the notation change $\dot{q}_i = |\dot{\epsilon}_i|$ from equation C19 of Lippuner & Roberts (2017).

as the total energy source term due to neutrino interactions.

2.1.4.2 Gravito-acoustic wave heating

Gravito-acoustic waves provide a secondary heat source in the wind as they steepen into shocks and deposit their energy. These waves propagate through a fluid element at the speed of sound. Because the waves are density perturbations and the sound speed is density-dependent, the peaks of the waves travel slightly faster than the troughs. This causes the waves to steepen into a sawtooth shape and form shocks, which efficiently thermalize the wave energy. Shocks will form at a radius R_s given by the time needed for the peak to catch up with a preceding trough (Mihalas & Mihalas, 1984):

$$\frac{1}{4}(\gamma+1)c_s^{-1}\int_0^{R_s} u_0(r')dr' = \frac{\pi c_s}{2\omega}, \tag{2.36}$$

which, with $u_0 = \sqrt{2\mathcal{E}/\rho}$ representing the velocity perturbation of the waves (Jacques, 1977), becomes

$$\int_0^{R_s}\sqrt{\frac{2c_s\omega\mathcal{N}}{v_g\rho}}dr' = \frac{2\pi c_s^2}{\omega(\gamma+1)}. \tag{2.37}$$

We can then use the shock jump conditions in combination with a model for the shock profile to obtain an estimate for l_d. A planar shock propagating in an ideal gas will be governed by the following shock jump conditions (Zel'dovich & Raizer, 1967):

$$M_0^2 \equiv \left(\frac{v_0}{c_{s,0}}\right)^2 = \frac{(\gamma+1)P_0+(\gamma-1)P_0}{2\gamma P_0} \tag{2.38}$$

$$\frac{\rho_1}{\rho_0} = \frac{(\gamma+1)P_0+(\gamma-1)P_0}{(\gamma-1)P_0+(\gamma+1)P_0} \tag{2.39}$$

$$s_1 - s_0 = c_v \ln\left[\frac{P_1}{P_0}\left(\frac{\rho_0}{\rho_1}\right)^\gamma\right], \tag{2.40}$$

representing the upstream Mach number and the compression and entropy changes across the shock. Upstream and downstream quantities are indicated by a "0" and "1" subscript, respectively. In a weak shock, the fractional pressure perturbation is small, i.e., $p \equiv (P_1 - P_0)/P_0 \ll 1$. Expanding equations (2.38)–(2.40) to lowest order in p and expressing them in terms of the reduced Mach

number $m \equiv M_0^2 - 1$, we have

$$m = \frac{\gamma + 1}{2\gamma} p \ll 1 \tag{2.41}$$

$$\frac{\rho_1}{\rho_0} - 1 = \frac{p}{\gamma} = \frac{2m}{\gamma + 1} \tag{2.42}$$

$$s_1 - s_0 = \frac{2c_v\gamma(\gamma - 1)}{3(\gamma + 1)^2} m^3. \tag{2.43}$$

Multiplying the entropy jump by the temperature T, and using the relation $(\gamma - 1)c_v T = P/\rho$, we obtain an expression for the heat deposition per unit mass due to a single shock:

$$\Delta q = T(s_1 - s_0) = \frac{2\gamma P_0}{3\rho(\gamma + 1)^2} m^3. \tag{2.44}$$

The change in heat per unit area Q as a fluid element traverses the shocks is given by Δq multiplied by the mass flux ρv_0:

$$\frac{DQ}{Dt} = v_0 \frac{dQ}{dr} = \frac{2\gamma P_0 v_0}{3(\gamma + 1)^2} m^3, \tag{2.45}$$

where we have applied the steady-state form of equation (2.13).

We now seek an expression for the mean energy per area Q carried by the waves. The phase velocity v_p as a function of position (z) in the wave is given by

$$v_p(z) = c_s + \frac{\gamma + 1}{2} u(z) \tag{2.46}$$

where $u(z)$ is the velocity perturbation of the wave. For an initially sinusoidal wave packet, $u(z) = u_0 \sin(kz)/2$. The variation in $u(z)$ causes the waves to steepen into a sawtooth profile, with velocity perturbation

$$u(z) = \frac{1}{2} u_0 \left(\frac{2z}{\lambda} - 1 \right), \qquad 0 < z \leq \lambda. \tag{2.47}$$

The shock, located at the leading edge of the wave packet, moves at a speed

$$v_0 = v_p(\lambda) = c_s + \frac{\gamma + 1}{4} u_0. \tag{2.48}$$

We can then express the reduced Mach number as

$$m = \left(\frac{v_0}{c_s} \right)^2 - 1 \approx \frac{\gamma + 1}{2} \frac{u_0}{c_s}. \tag{2.49}$$

A propagating wave will do work at a rate $(P_1 - P_0)u \approx \gamma P_0 u^2/c_s$. Integrated over one period (using $z = c_s t$), the energy flux transmitted by the wave is

$$Q = \frac{\gamma P_0}{c_s} \int_0^{\lambda/c_s} u^2 dt = \frac{\gamma P_0 u_0^2}{12 c_s^2} \lambda = \frac{\gamma P_0}{3(\gamma+1)^2} \lambda m^2, \tag{2.50}$$

where we use equation (2.49). Note that $Q = \mathcal{E}/\lambda$, so this also provides an expression for the energy density of the waves. Using equations (2.45) and (2.50), we can write down the characteristic dissipation length of the waves:

$$l_d = \left(\frac{1}{Q} \frac{dQ}{dr} \right)^{-1} = \frac{\lambda}{2m} = \frac{\pi c_s}{m\omega}. \tag{2.51}$$

We can thus write the entropy evolution equation (2.29) as

$$v \frac{ds}{dr} = \frac{S_E}{T}, \tag{2.52}$$

where

$$S_E = \left[(\dot{q}_{\nu_e} - \dot{q}_{e^+}) + (\dot{q}_{\bar{\nu}_e} + \dot{q}_{e^+} - \dot{q}_{e^-} - \dot{q}_{\nu_e}) Y_e + \frac{c_s}{\rho l_d} \omega \mathcal{N} \right] \tag{2.53}$$

represents the full energy source term including both wave and neutrino contributions, with l_d given by equation (2.51) and the $\dot{q}_i$ calculated according to Lippuner & Roberts (2017).

2.1.4.3 Scaling relationships

Using the equations above, we can derive a number of scaling relationships and order-of-magnitude estimates to describe what changes we should observe in the wind as the wave properties are changed. Inserting equation (2.50) into equation (2.51) with the definition of $\mathcal{N}$ yields

$$l_d = \frac{\pi c_s}{\omega(\gamma+1)} \left(\frac{\gamma v_g P}{3 c_s \omega \mathcal{N}} \right)^{1/2}. \tag{2.54}$$

In the limit $v \ll c_s$, and assuming a radiation-dominated $\gamma = 4/3$, we can use this to obtain an order-of-magnitude estimate of the dissipation length:

$$l_d \approx (1.64 \times 10^6 \,\mathrm{cm}) \frac{c_{s,9}}{\omega_3} \left(\frac{U}{10\mathcal{E}} \right)^{1/2} \tag{2.55}$$

where ω_3 and $c_{s,9}$ denote the wave frequency in units of $10^3\,\mathrm{s}^{-1}$ and the sound speed in units of $10^9\,\mathrm{cm\,s}^{-1}$, and $U = \rho\epsilon \approx P/(\gamma - 1)$ is the internal energy density of the wind. The factor of 10

accounts for the expected difference in scale between the wave and internal energy densities. In terms of the wave luminosity emerging from the evanescent region prior to dissipation L_w (see Equation 1.3), the dissipation length will scale as

$$l_d \propto L_w^{-1/2}\omega^{-1}. \tag{2.56}$$

Approximating density and pressure with power law expressions derived from our numerical results, we estimate the radius of shock formation will scale as

$$R_s \propto L_w^{-2/11}\omega^{-4/11}. \tag{2.57}$$

Therefore, as the wave luminosity is increased, we expect the radius of shock formation to move inward, making it more likely that the energy deposited by the shocks will affect seed nucleus formation. The dissipation length will respond more strongly, causing the waves to deposit their energy faster and increasing the effect on seed formation. Increasing the wave frequency will have a similar and stronger effect: the shocks will form earlier and deposit their energy more quickly at higher frequencies.

2.1.5 Lepton Number Conservation

Though it does not appear in the standard Euler equations, tracking the evolution of the electron fraction within a fluid element will be necessary to obtain accurate nucleosynthesis results. We can write down the material derivative

$$\frac{DY_e}{Dt} = (\lambda_{\nu_e} + \lambda_{e^+})Y_n - (\lambda_{\bar{\nu}_e} + \lambda_{e^-})Y_p \tag{2.58}$$

where the λ_i represent the rates of the neutrino reactions in equation (2.34). Again, these rates rapidly fall off with the neutrino flux experienced by the fluid element as it moves outward in the wind, causing the electron fraction to asymptote to a certain value very early on. In a wind purely affected by neutrinos (no waves, magnetic fields, etc.), Y_e approaches the equilibrium value of equation (1.1). Taking the approximation $Y_n = 1 - Y_p$ and $Y_p = Y_e$ and applying equation (2.13), we find

$$v\frac{dY_e}{dr} = \lambda_{\nu_e} + \lambda_{e^+} - (\lambda_{\bar{\nu}_e} + \lambda_{e^-} + \lambda_{\nu_e} + \lambda_{e^+})Y_e = S_{Y_e} \tag{2.59}$$

for the final form of the lepton number conservation equation.

2.1.6 Corrections from General Relativity

The extreme density of the PNS makes relativistic corrections important for accurately modeling the wind (Cardall & Fuller, 1997; Otsuki et al., 2000). Because the total mass of the wind is far less than the PNS mass, we treat the system in the Schwarzschild limit, in which the mass of the system is treated as a point source at the center of the PNS. The derivation is quite involved; following a similar process to Thompson et al. (2001), we find adjusted forms of the mass, momentum, energy, and lepton number conservation equations (absent wave effects):

$$\begin{aligned}
\dot{M} &= 4\pi r^2 e^{\Lambda} W v \rho \\
(v^2 - c_s^2)\frac{dv}{dr} &= -\frac{v}{\rho}\left(\frac{P}{s}\frac{\Gamma^{Ps}_{\rho Y_e}}{W^2 h}\frac{ds}{dr} + \frac{P}{Y_e}\frac{\Gamma^{PY_e}_{\rho s}}{W^2 h}\frac{dY_e}{dr}\right) + \frac{v}{r}\left(\frac{2c_s^2}{W^2} - \frac{GM}{r^2}\frac{c^2 - c_s^2}{c^2 e^{2\Lambda} W^2}\right) \\
v\frac{ds}{dr} &= \frac{S_E}{e^{\Lambda} W T} \\
v\frac{dY_e}{dr} &= \frac{S_{Y_e}}{e^{\Lambda} W}.
\end{aligned}$$

For the mass, energy, and lepton number conservation equations, the corrections take the form of a simple prefactor in terms of the Lorentz factor $W = \left(1 - \frac{v^2}{c^2}\right)^{-\frac{1}{2}}$ and the metric function $e^{\Lambda} = \sqrt{1 - \frac{2GM}{rc^2}}$. The critical form of the momentum equation is somewhat more involved, using the dimensionless form of the specific enthalpy $h = \rho(c^2 + e) + P/\rho c^2$, with e representing the energy density of the wind. Ignoring the wave contribution terms, we can recognize the form of equation (2.25), and so we can adjust our definition of f_2 from equation (2.26) to incorporate the relativistic corrections:

$$f_2 = \frac{r}{\rho c_s^2}\left(\frac{P}{s}\frac{\Gamma^{Ps}_{\rho Y_e}}{W^2 h}\frac{ds}{dr} + \frac{P}{Y_e}\frac{\Gamma^{PY_e}_{s\rho}}{W^2 h}\frac{dY_e}{dr}\right) - \frac{2}{W^2} + \frac{GM}{rc_s^2}\frac{c^2 - c_s^2}{c^2 e^{2\Lambda} W^2}. \tag{2.60}$$

Ideally, we would also include relativistic effects on the wave contribution terms δf_1 and δf_2. We do not for two reasons. First, the derivation of the wave stress contributions to the momentum equation we follow from Jacques (1977) relies on the eikonal (WKB) approximation. The additional accuracy to be gained from including relativistic effects would not outweigh the uncertainty introduced by this

approximation. Second, the derivation we follow relies on a complicated formalism to differentiate the waves from the background fluid, and (to our knowledge) no one has yet worked out a general-relativistic version of this formalism. The final form of the conservation equations is thus

$$\dot{M} = 4\pi r^2 e^{\Lambda} W v \rho \tag{2.61}$$

$$(f_1 + \delta f_1)\frac{d\ln v}{d\ln r} = f_2 + \delta f_2 \tag{2.62}$$

$$v\frac{ds}{dr} = \frac{1}{e^{\Lambda} W T}\left[(\dot{q}_{\nu_e} - \dot{q}_{e^+}) + (\dot{q}_{\bar{\nu}_e} + \dot{q}_{e^+} - \dot{q}_{e^-} - \dot{q}_{\nu_e})Y_e + \frac{\mathcal{L}}{4\pi r^2 \rho l_d}\right] \tag{2.63}$$

$$v\frac{dY_e}{dr} = \frac{1}{e^{\Lambda} W}\left[\lambda_{\nu_e} + \lambda_{e^+} - (\lambda_{\bar{\nu}_e} + \lambda_{e^-} + \lambda_{\nu_e} + \lambda_{e^+})Y_e\right] \tag{2.64}$$

$$\frac{d\ln \mathcal{L}}{dr} = -\frac{1}{l_d} \tag{2.65}$$

with

$$\begin{aligned}
f_1 &= 1 - \frac{v^2}{c_s^2} \\
\delta f_1 &= -\frac{a_1 \mathcal{L}}{4\pi r^2 \rho c_s v_g^2}\left(\frac{c_s - v}{v}\Gamma^{c_s\rho}_{sY_e} - 2\right) \\
f_2 &= \frac{P}{\rho c_s^2}\left(\frac{r}{s}\frac{\Gamma^{Ps}_{\rho Y_e}}{W^2 h}\frac{ds}{dr} + \frac{r}{Y_e}\frac{\Gamma^{PY_e}_{s\rho}}{W^2 h}\frac{dY_e}{dr}\right) - \frac{2}{W^2} + \frac{GM}{r c_s^2}\frac{c^2 - c_s^2}{c^2 e^{2\Lambda} W^2} \\
\delta f_2 &= -\frac{a_1 \mathcal{L}}{4\pi r^2 \rho c_s v_g^2}\left[\frac{c_s - v}{v_g}\left(\frac{r}{s}\Gamma^{c_s s}_{\rho Y_e}\frac{ds}{dr} + \frac{r}{Y_e}\Gamma^{c_s Y_e}_{s\rho}\frac{dY_e}{dr} - 2\Gamma^{c_s\rho}_{sY_e}\right) + \frac{r}{l_d} + 2(1 - 1/a_1)\right]
\end{aligned} \tag{2.66}$$

and the λ_i and $\dot{q}_i$ calculated according to Lippuner & Roberts (2017) assuming a zero chemical potential Fermi-Dirac spectrum.

2.1.7 Wind Termination Shock

The NDW does not take place in a vacuum—eventually the fast-moving, transonic wind will impact slower-moving material behind the primary supernova shock. We follow Arcones & Thielemann (2012) in our treatment of this. Once the wind reaches a certain radius R_{WT}, we employ the relativistic Rankine-Hugoniot shock conditions:

$$v_0 \rho_0 W_0 = v_1 \rho_1 W_1 \tag{2.67}$$

$$W_0^2 h_0 \rho_0 v_0^2 + P_0 = W_1^2 h_1 \rho_1 v_1^2 + P_1 \tag{2.68}$$

$$W_0 h_0 = W_1 h_1 \tag{2.69}$$

where the subscript "0" denotes the unshocked wind quantities, and "1" the post-shock quantities. For the first second post-shock (calculated with $\Delta t = \int_{\psi_1}^{\psi_2} (\partial v/\partial r)^{-1} d\psi$, see section 2.2.3), we hold the density constant while decreasing velocity as r^{-2}. After this, we assume the wind obeys a purely homologous outflow, with constant velocity and density decreasing as r^{-2} through the end of the simulation.

2.2 Computational Method

The physics of our model for the NDW is fully contained in the equations above. To obtain the properties of the steady-state wind, we will integrate a form of equations (2.61)–(2.65) from the surface of the PNS, where the wind is launched, to a far radius of 10^{10} cm. There are some important factors that must be considered, however, in order to translate these equations into a robust numerical simulation.

2.2.1 EOS Considerations

Our equations are closed by the Helmholtz equation of state (Timmes & Swesty, 2000) for radiation-dominated material. This equation of state was derived specifically for astrophysical scenarios like the NDW, in which electrons and positrons are arbitrarily relativistic and degenerate. This EOS is tabulated, however, with respect to density, temperature, and electron fraction, whereas the equations we have derived describe the entropy rather than the temperature. To make use of the tabulated Helmholtz EOS, we must derive an equation for the temperature evolution of the wind. We begin with

$$\frac{dT}{dr} = \left(\frac{\partial T}{\partial s}\right)_{\rho,Y_e} \frac{ds}{dr} + \left(\frac{\partial T}{\partial \rho}\right)_{s,Y_e} \frac{d\rho}{dr} + \left(\frac{\partial T}{\partial Y_e}\right)_{s,\rho} \frac{dY_e}{dr}. \tag{2.70}$$

Substituting from equations (2.61)–(2.65), we have

$$\frac{dT}{dr} = \Gamma^{Ts}_{\rho Y_e} \frac{S_E}{ve^{\Lambda}WT} - \rho\Gamma^{T\rho}_{sY_e}\left(\frac{W^2}{v}\frac{dv}{dr} + \frac{2}{r} + \frac{GM}{r^2e^{2\Lambda}}\right) + \Gamma^{TY_e}_{s\rho}\frac{S_{Y_e}}{ve^{\Lambda}W} \tag{2.71}$$

and inserting equation (2.62)

$$\frac{dT}{dr} = \Gamma^{Ts}_{\rho Y_e} \frac{S_E}{ve^{\Lambda}WT} - \rho\Gamma^{T\rho}_{sY_e}\left(\frac{W^2}{r}\frac{f_2+\delta f_2}{f_1+\delta f_1} + \frac{2}{r} + \frac{GM}{r^2c^2}\frac{c^2-c_s^2}{e^{2\Lambda}}\right) + \Gamma^{TY_e}_{s\rho}\frac{S_{Y_e}}{ve^{\Lambda}W}. \tag{2.72}$$

This will replace equation (2.63) as one of the equations we integrate, and the entropy will be calculated through the tabulated EOS instead.

2.2.2 Initial Conditions

To obtain a solution to the differential equations we have found, we require a set of initial conditions. Specifically, we require an initial velocity, temperature, electron fraction, and wave action. The initial velocity we leave as a free parameter, calculated such that the wind becomes transonic at the critical point (see section 2.2.3 below). Qian & Woosley (1996) argue that at the surface of the PNS, neutrino heating and cooling will be in equilibrium, i.e.,

$$\dot{q}_{\nu_e} + (\dot{q}_{\bar{\nu}_e} + \dot{q}_{e^+})Y_e = \dot{q}_{e^+} + (\dot{q}_{e^-} + \dot{q}_{\nu_e})Y_e. \tag{2.73}$$

The $\dot{q}_i$ are temperature dependent, so we employ a rootfinding algorithm to simultaneously calculate the initial temperature and electron fraction based on this condition. Finally, the initial effective wave luminosity $\mathcal{L}$ is simply equal to the specified wave luminosity L_w.

A number of parameters must also be specified before integrating the equations. These include the PNS mass and radius, the electron neutrino and antineutrino luminosities and energies, the location of the wind termination shock, and the wave luminosity and frequency. We can select these arbitrarily from a chosen parameter space, or extract them from a preexisting data set.

2.2.3 Circumventing the Critical Point

As the evolution equations indicate, a singularity exists when $f_1 + \delta f_1 = 0$, commonly referred to as the transsonic point. A physical wind solution must become trans-sonic in order to escape the PNS gravity well, so the singularity must be handled by our code. A singularity will cause problems for a numerical integrator, so we must find a way to effectively remove or circumvent it to make the equations tractable. We do so by introducing an auxiliary integration variable ψ, and splitting equation (2.62) into separate differential equations for v and r in terms of ψ:

$$\frac{d\ln r}{d\psi} = f_1 + \delta f_1 \tag{2.74}$$

$$\frac{d\ln v}{d\psi} = f_2 + \delta f_2. \tag{2.75}$$

We can similarly recast the other evolution equations:

$$\frac{d\ln T}{d\psi} = \frac{f_1+\delta f_1}{ve^{\Lambda}WT}\left(\Gamma^{Ts}_{\rho Y_e}\frac{S_E}{T}+\Gamma^{TY_e}_{s\rho}S_{Y_e}\right) - \frac{\rho}{T}(f_1+\delta f_1)\Gamma^{T\rho}_{sY_e}\left(\frac{W^2}{r}\frac{f_2+\delta f_2}{f_1+\delta f_1}+\frac{2}{r}+\frac{GM}{r^2c^2}\frac{c^2-c_s^2}{e^{2\Lambda}}\right) \tag{2.76}$$

$$\frac{d\ln Y_e}{d\psi} = \frac{r}{vY_e}(f_1+\delta f_1)\frac{S_{Y_e}}{e^{\Lambda}W} \tag{2.77}$$

$$\frac{d\ln \mathcal{L}}{d\psi} = -\frac{r}{l_d}(f_1+\delta f_1) \tag{2.78}$$

To determine where the waves begin to shock, we also must track the value of the integral in equation (2.37). We define

$$I = \int_0^r \sqrt{\frac{2c_s\omega\mathcal{N}}{v_g\rho}}dr' \tag{2.79}$$

so that

$$\frac{dI}{dr} = \sqrt{\frac{2c_s\omega\mathcal{N}}{v_g\rho}} \tag{2.80}$$

and thus

$$\frac{dI}{d\psi} = \sqrt{\frac{2c_s\omega\mathcal{N}}{v_g\rho}}f_1 r. \tag{2.81}$$

When I is equal to the right-hand side of equation (2.37), shock heating begins in the wind. We model this via the dissipation length l_d through an interpolation function:

$$J = 2\left(1+e^{2\pi c_s^2/I\omega(\gamma+1)}\right)^{-1}, \tag{2.82}$$

so that J approaches 1 as I approaches the shock condition. We then treat l_d as

$$l_d = \left(\frac{1-J}{10^{200}}+\frac{J}{l_{d,\mathrm{phys}}}\right)^{-1}, \tag{2.83}$$

where $l_{d,\mathrm{phys}}$ is given by the expression in equation (2.54), and 10^{200} is a very large number representing an infinite dissipation length. At small radii, l_d is essentially infinite and no shock heating occurs. Once the wind approaches the point where the waves should begin shocking, l_d smoothly transitions to its physical value. A smooth transition is helpful for the integrator and is perhaps more realistic than a sharp transition.

With our equations recast in terms of ψ, no infinities will be encountered by the integrator, but we can still identify the trans-sonic trajectory by checking if $f_1+\delta f_1$ and $f_2+\delta f_2$ pass through zero at the same point.

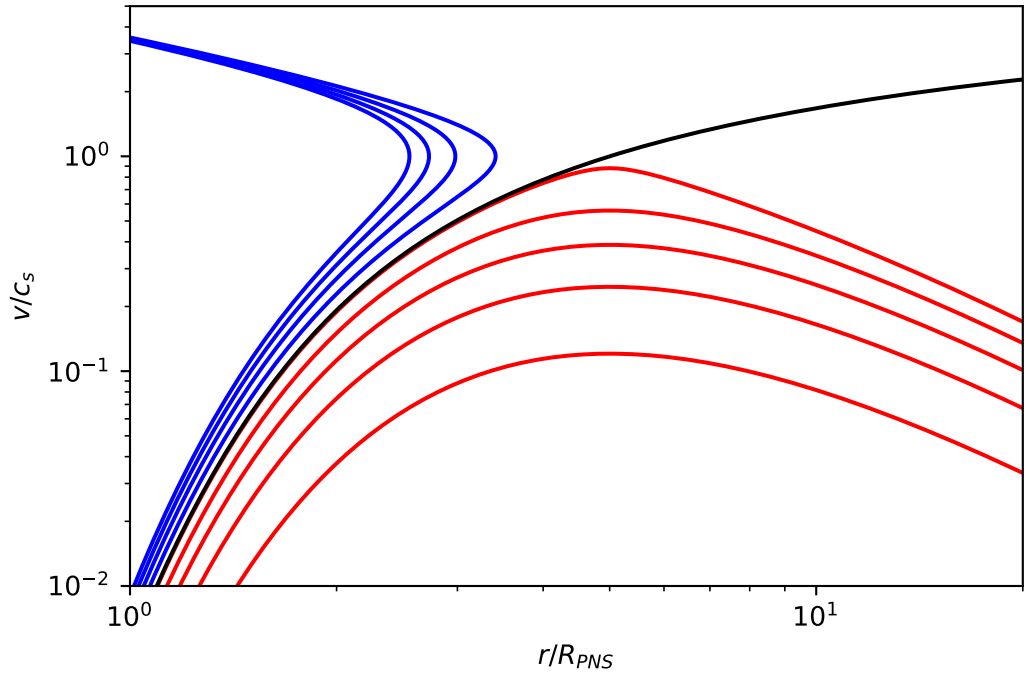

Figure 2.1 The solution families for a simplified wind model without wave contributions. Blue curves show unphysical double-valued solutions; red curves show breeze solutions that eventually fall back onto the PNS; and the black curve shows the trans-sonic wind solution.

2.2.4 Numerical Integration Method

To obtain robust profiles for these differential equations, we employ a fourth-order singly-diagonally implicit Runge-Kutta numerical integration method (Kennedy & Carpenter, 2016) with an adaptive step size in ψ. Solutions to our differential equation set fall into 3 categories (illustrated in Figure 2.1): unphysical solutions, breeze solutions, and the desired trans-sonic solution. An overly fast initial velocity leads to an unphysical double-valued solution as the initially positive $d\ln r/d\psi$ becomes negative before $d\ln v/d\psi$, curving the solution back to $r = 0$. A slow initial velocity leads to $d\ln v/d\psi$ becoming negative first, and the wind slows down and does not become unbound. Given sufficient time, the material would fall back to the surface of the PNS in a breeze solution. For a given set of PNS parameters, there exists exactly one initial velocity value for which the solution becomes transsonic and the wind material becomes unbound from the PNS. We use a rootfinder to determine this velocity, comparing the values of $d\ln r/d\psi$ and $d\ln v/d\psi$ when one

passes through zero. When they cross zero simultaneously, because even machine precision is not sufficiently precise to obtain the transsonic solution, we run the integration taking the absolute values of $f_1 + \delta f_1$ and $f_2 + \delta f_2$ instead of their signed values. This generates a machine-precision accurate transsonic solution. We integrate this solution to a maximum radius of $r = 10^{10}$ cm, transitioning to a homologous outflow when the wind reaches the termination shock radius $R_{\rm WT}$. This yields radius, velocity, temperature, and density profiles describing the wind, and other quantities such as the entropy can be extracted as well. We also track the various neutrino reaction rates for use in nucleosynthesis calculations.

2.2.5 Nucleosynthesis Calculations

Our goal in this work is to determine the impact of wave effects on the nucleosynthetic processes at work in the NDW. To that end, we employ the SkyNet reaction network (Lippuner & Roberts, 2017). SkyNet takes density and temperature profiles as a function of time, and tracks the evolution of over 7000 different nuclides based on their reaction rates. Reaction rates are taken from the REACLIB library, and include strong, weak, symmetric fusion, and spontaneous fusion reactions. Inverse reactions are calculated via detailed balance, and charged-current neutrino reactions on nucleons can optionally be included as well. To obtain time-dependent temperature and density profiles from our steady-state models, we take $t(\psi) = \int_0^\psi (\partial v/\partial r)^{-1}$. These profiles are then extended to late times ($t = 10^9$ s) with a t^{-3} power law to capture nuclear decays. SkyNet takes these profiles and returns an array of nuclide abundances for each time step it calculates, yielding both a final abundance distribution for the nuclides formed in the wind as well as a time evolution of those abundances.

CHAPTER 3

PROTO-NEUTRON STAR CONVECTION AND THE R-PROCESS

The contents of this chapter are adapted from Nevins & Roberts (2023), which has been published in The Monthly Notices of the Royal Astronomical Society.

3.1 Background

The origins of the various chemical elements is one of the fundamental questions of nuclear astrophysics. In their seminal paper, Burbidge et al. (1957) proposed rapid neutron captures onto heavy ($A \geq 12$) seed nuclei, followed by β-decays back toward stability, in a high-energy, high-neutron density environment as the source of many of the heaviest elements found in the solar system. The site of this "r-process" has been a topic of much study in recent decades. The visual counterpart to GW170817 provided exciting evidence of r-processing in the ejecta of a binary neutron star merger (Drout et al., 2017), but several studies have cast doubt on compact object mergers as the sole r-process site, with some form of supernovae favored as an additional site (Côté et al., 2019; Cavallo et al., 2021; Kobayashi et al., 2023; Van der Swaelmen et al., 2023). Many studies have also noted discrepancies between the abundance distributions of the heaviest (third-peak) r-process elements and lighter (first-peak) elements, indicating perhaps an additional weak r-process site that only forms lighter elements (Arcones & Montes, 2011). The neutrino-driven wind was theorized to be a promising site for r-processing (Woosley & Baron, 1992), and the simulations of Woosley et al. (1994) catapulted it into the spotlight as a leading candidate for the primary site of the r-process. These simulations found wind entropies in excess of 400 k_{B} baryon^{-1} with an electron fraction of $Y_e \approx 0.4$, which allowed a robust, solar-like r-process to proceed.

Subsequent work, however, failed to reproduce these optimistic results, consistently yielding entropies a factor of 2–3 smaller than those initially reported (Witti et al., 1994; Qian & Woosley, 1996; Otsuki et al., 2000; Thompson et al., 2001). Detailed theoretical work by Hoffman et al. (1997) determined an approximate criterion for strong, third-peak r-processing based on the nearly constant asymptotic entropy, dynamical timescale, and electron fraction of the wind (see section

1.2.1 for the sensitivity of NDW nucleosynthesis to these parameters):

$$\eta \equiv \frac{s^3}{\tau_d Y_e^3} \gtrsim 10^{10}, \tag{3.1}$$

evaluated at $T \approx 0.5\,\mathrm{MeV}$, indicates a wind likely to undergo a third-peak r-process. No simulated winds met this criterion except in the most extreme conditions. Yet, if a reasonable secondary heating source could be found to boost the entropy of the wind, Hoffman et al. (1997) hypothesized that an r-process could become likely.

A number of factors were investigated in the following years that could affect the value of η in the wind. The models derived by Qian & Woosley (1996) and Hoffman et al. (1997) were purely Newtonian, and did not incorporate corrections from general relativity (though they did provide estimates of the effects in a post-Newtonian calculation). A number of publications bore out their predictions that GR corrections would have a positive effect on the entropy (Cardall & Fuller, 1997; Otsuki et al., 2000; Thompson et al., 2001), but the increase was insufficient. A PNS mass $\gtrsim 2\,M_\odot$ was still required to obtain high enough entropies to predict a strong r-process. Other research focused on magnetic fields: a strong magnetic field could trap material near the PNS, exposing it to more neutrino heating and raising the entropy. Again, to obtain a high enough entropy, extreme conditions—a magnetar-strength field—were required (Thompson, 2003; Suzuki & Nagataki, 2005; Metzger et al., 2007). Rapid rotation, which accelerates the wind (decreasing τ_d) proved helpful, but high magnetic field strengths were still required. To make matters worse, investigations of PNS neutrino spectra indicated that, rather than being very neutron rich with $Y_e \lesssim 0.4$, the electron fraction in the wind was likely $Y_e \gtrsim 0.48$, with the wind becoming more proton-rich over time (Fischer et al., 2010; Hüdepohl et al., 2010; Roberts et al., 2012a; Martínez-Pinedo et al., 2012; Pllumbi et al., 2015; Xiong et al., 2019). Wanajo (2013) performed a thorough study of NDW r-processing taking into account many of these factors, and found that unless extremely massive PNSs are formed, no r-process is predicted. Our base-case models (neglecting wave contributions) agree with these results, as Figures 3.1 and 3.2 indicate. NDWs in magnetorotational supernovae with high PNS magnetic fields and rapid rotation are recognized as a plausible r-process site (Desai et al., 2022; Van der Swaelmen et al., 2023; Prasanna et al., 2024) due to the high wind entropies

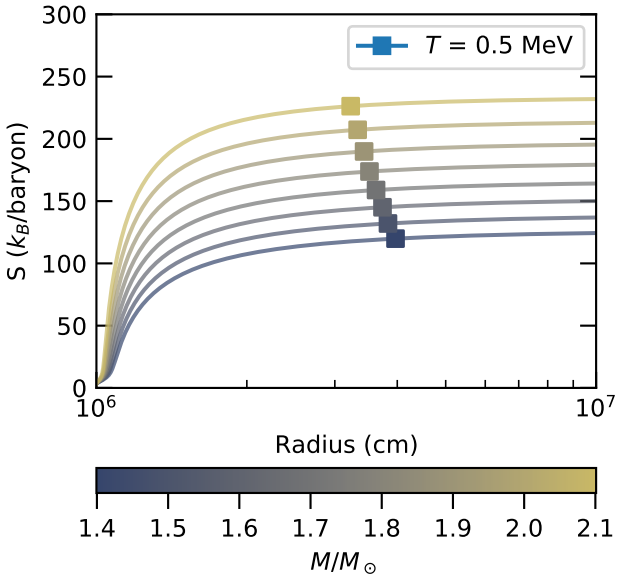

Figure 3.1 Entropy versus radius profiles for PNSs of varying mass, with a fixed total neutrino luminosity of 6×10^{51} ergs^{-1}, and $L_w = 0$. We find comparable behavior to Wanajo (2013), with asymptotic entropies well below the 400 k_B baryon^{-1} found by Woosley et al. (1994). The point at which $T = 0.5$ MeV, roughly where seed formation begins, is marked with a square.

that can attain, but outside these relatively extreme conditions the NDW is generally considered an unlikely site for the r-process.

There remains at least one physical factor likely to affect the NDW that has not seen much consideration, and which could thoroughly alter this outlook: the effects of waves propagating through the wind. Suzuki & Nagataki (2005) examined magnetic field-driven Alfvén waves, and found that they could act as an effective heat source to enable r-processing if they carried enough energy (that is, if the magnetic field were strong enough). Metzger et al. (2007) briefly introduced PNS convection as another means of generating waves, and predicted that if the luminosity carried by waves exceeded a fraction of $\sim 10^{-4}$ of the neutrino luminosity, the entropy would increase enough to drive an r-process. In fact, the predicted luminosity of convection-driven gravito-acoustic waves is likely to fall in the range of 10^{-5} to 10^{-2} L_ν (see chapter 1). Vigorous PNS convection is a common feature of modern 3D supernova simulations (e.g., Nagakura et al., 2020; Nagakura et al., 2021), so finding strong r-processing in a realistic convective PNS parameter space would have important ramifications for galactic chemical evolution predictions. The contents of

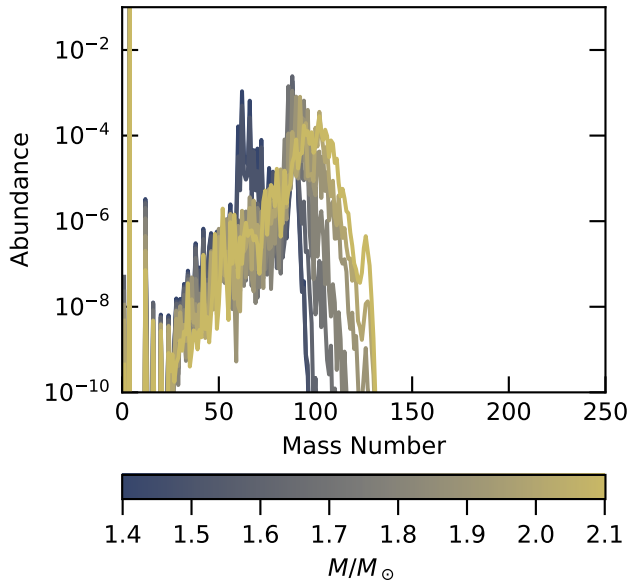

Figure 3.2 Final abundances for the wind profiles of Figure 3.1. We find that no r-processing takes place for proto-neutron stars of reasonable masses with $Y_{e,\mathrm{eq}} = 0.48$, when wave effects are excluded.

this chapter (the results of which have been published as Nevins & Roberts, 2023) follow up on this prediction, carefully examining the impact of convection-generated gravito-acoustic waves on a possible r-process in a neutron-rich NDW. For the simulations in this section (unless otherwise noted), we assume an equilibrium electron fraction of $Y_{e,\mathrm{eq}} = 0.48$ with an average electron neutrino energy of 12 MeV. The average electron antineutrino energy is then calculated to satisfy equation (1.1). This will yield a reasonable yet still neutron-rich NDW in accord with the studies cited above, allowing for the possibility of r-processing without artificially enhancing its likelihood.

We focus in this chapter on qualitative analysis of how wave effects alter the wind dynamics and nucleosynthesis rather than detailed, integrated abundance yields. To that end, the parameters that are fed into our model ($R_{\mathrm{PNS}}, M_{\mathrm{PNS}}, L_\nu, \langle\epsilon_{\nu_e}\rangle, R_{\mathrm{WT}}, L_w, \omega$) are varied independently, allowing us to freely explore the parameter space. We assume equal neutrino luminosities in all flavors, and the average electron antineutrino energy is determined by $Y_{e,\mathrm{eq}}$ and the neutrino luminosities. Unless otherwise noted, we use the canonical $R_{\mathrm{PNS}} = 10\,\mathrm{km}$, and take $\epsilon_{\nu_e} = 12\,\mathrm{MeV}$, $\omega = 2 \times 10^3\,\mathrm{s}^{-1}$, and $R_{\mathrm{WT}} = 5 \times 10^8\,\mathrm{cm}$ as fiducial values.

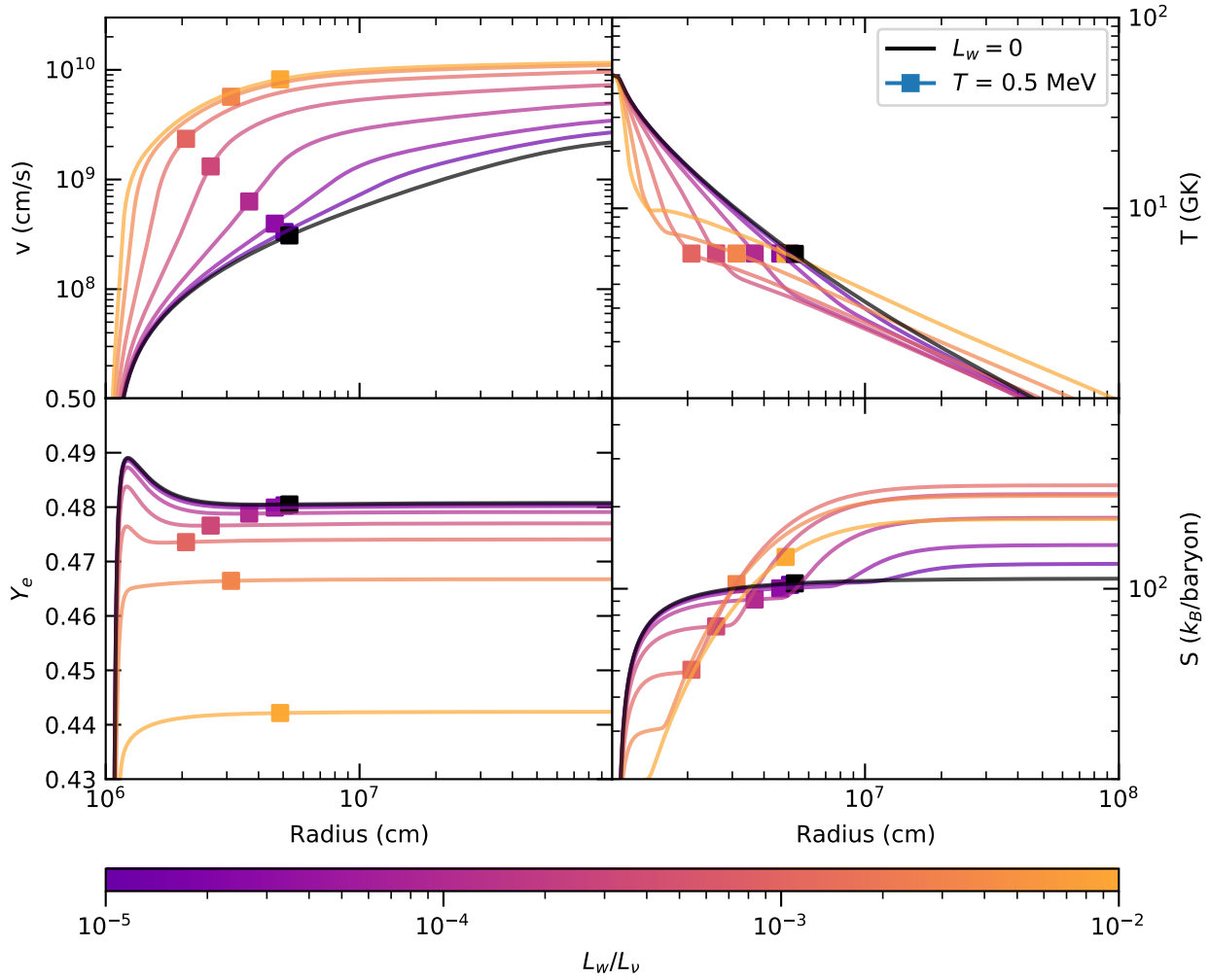

Figure 3.3 Radial profiles of the velocity, density, temperature, and entropy in the NDW. Different lines correspond to different L_w. Other parameters in the wind models were fixed to $M_{\rm NS} = 1.5\,M_\odot$, $L_\nu = 3 \times 10^{52}\,{\rm erg\,s^{-1}}$, and $\omega = 2 \times 10^3\,{\rm s^{-1}}$. The approximate beginning of seed formation for each model is marked a square.

3.2 Wind Dynamics

As described in chapter 1, propagating waves affect the NDW in two primary ways: momentum deposition via mechanical stress, and energy deposition via shock formation. Figure 3.3 shows these effects for a fiducial PNS parameter set with $M_{\rm PNS} = 1.5\,M_\odot$ and $L_\nu = 3 \times 10^{52}\,{\rm erg\,s^{-1}}$, and the results are qualitatively similar for more extreme parameter sets. Clearly, above $L_w/L_\nu \approx 10^{-5}$, the inclusion of wave effects has a significant impact on the dynamics of the wind. Although L_w in these models is a relatively small fraction of the total neutrino luminosity, it is a large fraction of

the neutrino energy that couples to the wind, which goes as

$$\frac{\dot{q}_\nu}{L_{\nu,\mathrm{tot}}} \sim 1.5 \times 10^{-4} L_{\bar{\nu}_e,51}^{2/3} \left(\frac{R}{10\,\mathrm{km}}\right)^{2/3} \left(\frac{1.4\,M_\odot}{M_{\mathrm{PNS}}}\right). \tag{3.2}$$

At small radii, before the waves shock, they accelerate the NDW but do not provide any heating. This results in increasing velocities with L_w/L_ν, and therefore lower densities at a given radius by the relation $\dot{M}_{\mathrm{PNS}} = 4\pi r^2 e^\Lambda W \rho v$. Additionally, since the acceleration of the wind is no longer provided solely by neutrino heating, the amount of neutrino heating that occurs is lowered, which results in both lower entropies before the wave-heating activation radius, and in lower electron fractions at all points in the wind. As the wave contribution increases, fewer neutrino captures are required to unbind material from the potential well of the PNS and the NDW is accelerated to higher velocities at smaller radii. Both of these effects work to reduce the number of weak interactions in the wind and prevent the electron fraction in the wind from reaching $Y_{e,\mathrm{eq}}$, which results in more neutron-rich conditions at the beginning of nucleosynthesis. The changes in Y_e begin prior to the waves forming weak shocks, indicating that the wave stress, rather than shock heating, is the primary contributor. These effects will therefore be present regardless of any uncertainty in the shock heating mechanism. We observe a spike in Y_e at small radii due to electron-positron capture when degeneracy is lifted at high temperatures. The electron fraction then relaxes towards $Y_{e,\mathrm{eq}}$, but may not reach it due to the wave contributions.

The radius at which the waves shock and the rate at which they damp will depend on their frequency content, with the shock formation radius approximately scaling as ω^{-1} (see equation (2.37)) and the damping length $l_d \propto \omega^{-1}$ for a fixed L_w. Therefore, larger wave frequencies will result in wave heating impacting the thermodynamic conditions of the NDW at smaller radii and higher temperatures. In Figure 3.4, we show the impact of varying ω on the entropy of the wind. Clearly, larger ω results in a higher entropy at higher temperature, which is potentially more favorable for later r-processing. The limiting case ($\omega \to \infty$) corresponds to instantaneous shock formation in the wind, but also implies a damping length that goes to zero. Nevertheless, we also show a case with fixed ω in l_d but assuming instantaneous shock formation, as this has been assumed in previous work looking at secondary heating mechanisms in the NDW (Suzuki & Nagataki, 2005; Metzger

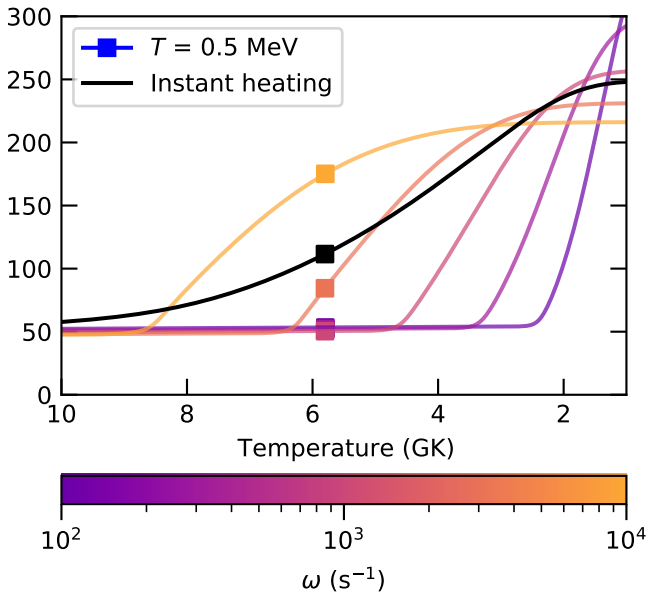

Figure 3.4 Early entropy profiles for a 1.5 $M_\odot$ neutron star with $L_\nu = 3 \times 10^{52}$ erg s^{-1} and $L_w = 10^{-3} L_\nu$ with varied wave frequencies. For higher frequencies, the shock heating begins to increase the entropy in the wind earlier and has a larger impact where seed nuclei are formed. The impact of the shock prescription is illustrated by the black line, which shows the evolution of the entropy if the waves (with $\omega = 2 \times 10^3$ s^{-1}) shock immediately instead of when equation (2.37) dictates.

et al., 2007). It is not clear what shock formation radii are favored, given the uncertainty in the range of frequencies excited by PNS convection and the approximate nature of equation (2.37).

Subsequent to the waves shocking, the entropy rapidly increases in all models. Shock formation occurs at temperatures between 2 and 10 GK depending on L_w/L_ν (and ω, see Figure 3.4). The extra entropy production provided by $\dot{q}_w$ is large compared to neutrino heating because of the low temperatures at which it occurs compared to the temperatures where the bulk of the neutrino heating takes place ($\sim$ 30 GK in our simulations). For the largest L_w/L_ν, the entropy can reach asymptotic values of 300, which is quite large compared to even the largest entropies found for models that do not experience wave heating. Nevertheless, a significant amount of the entropy production occurs during or after the temperatures over which seed nuclei for the r-process are produced ($\sim$ 2–8 GK). Therefore, estimating the likelihood of r-process nucleosynthesis from the η metric (see equation (3.1)) is difficult as s is no longer nearly constant while seed production occurs. Before the shock formation radius, the waves reduce both s and τ_d[1]. This can hinder or abet an alpha-rich freezeout

[1]We define the dynamical timescale τ_d at a given point in the wind as $T/\dot{T}$, similar to the $r/\dot{r}$ used by Hoffman

depending on the relative strength of these two effects. After shock formation, s is increased relative to the $L_w = 0$ case, but potentially at temperatures that are too low to impact the alpha-richness of the NDW. Therefore, to better understand the impact of gravito-acoustic wave heating on the wind, detailed nucleosynthesis calculations are required.

3.3 Nucleosynthesis

We now turn our attention to the nucleosynthesis data obtained from applying the SkyNet reaction network to the thermodynamic profiles generated in the previous section. First, we consider the impact of varying L_w/L_ν for a fixed $\omega = 2 \times 10^3\ \mathrm{s}^{-1}$. The final abundances for NDW models with $M_{\mathrm{NS}} = 1.5\,M_\odot$ and $L_\nu = 3 \times 10^{52}\,\mathrm{erg\,s}^{-1}$ are shown in Figure 3.5. These correspond to the NDW models shown in Figure 3.3. In the absence of wave heating, this parameter set only undergoes an α-process that terminates with a peak around mass 90 (Woosley & Hoffman, 1992) and is far from the conditions necessary for producing the third r-process peak. Increasing L_w, we find that the peak of the abundance distribution increases in mass until $L_w/L_\nu \approx 10^{-4}$. Further increase of L_w from this point briefly reduces the mass of the peak of the abundance distribution, but above $L_w/L_\nu \approx 10^{-3}$ a strong r-process emerges. The final abundances for NDW models with $M_{\mathrm{NS}} = 1.9\,M_\odot$ and $L_\nu = 6 \times 10^{52}\,\mathrm{erg\,s}^{-1}$ are shown in Figure 3.6. Between $L_w/L_\nu = 10^{-5}$ and $L_w/L_\nu = 10^{-4}$, these models produce both the second and third r-process peaks, but between $L_w/L_\nu \approx 10^{-4}$ and $L_w/L_\nu \approx 10^{-3}$ production of the third peak is again cutoff and the peak of the abundance distribution is pushed down to lower mass. As L_w/L_ν is increased above 10^{-3}, a strong r-process re-emerges.

For both sets of parameters, we find the interesting behavior that r-process nucleosynthesis is inhibited for L_w/L_ν in the approximate range of 10^{-4}–10^{-3}. This turnover in the maximum mass number is due to the competition between the decreasing dynamical timescale (τ_d) with L_w, which inhibits seed formation, and the decreasing entropy (s) with L_w, which facilitates seed production by increasing the density at which alpha recombination occurs (Hoffman et al., 1997). Figure 3.7 illustrates the correlation between the quantity $s^3/Y_e^3\tau_d$ and the total abundance above mass 150.

et al. (1997).

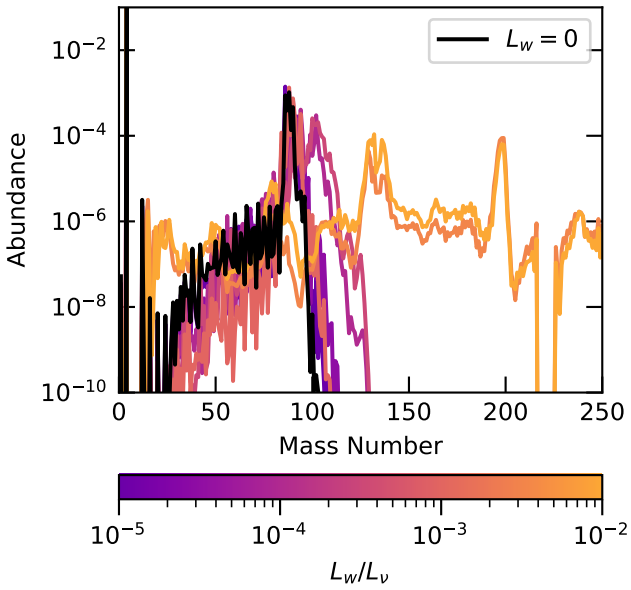

Figure 3.5 Final nucleosynthesis results, using temperature and density profiles for a 1.5 $M_\odot$ neutron star, with $L_\nu = 3 \times 10^{52}\,\mathrm{erg\,s^{-1}}$ and using a wave frequency of $2 \times 10^3\,\mathrm{s^{-1}}$. A clear peak around mass 200 is indicative of a strong r-process taking place.

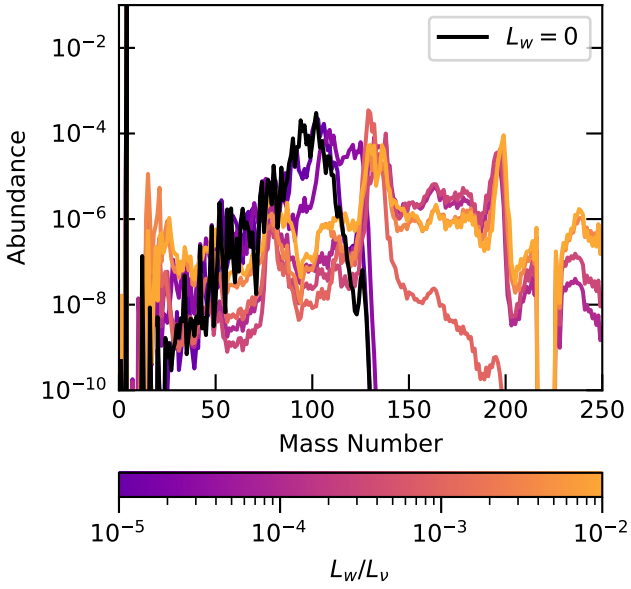

Figure 3.6 Final nucleosynthesis results, using temperature and density profiles for a 1.9 $M_\odot$ neutron star, with $L_\nu = 6 \times 10^{52}\,\mathrm{erg\,s^{-1}}$ and using a wave frequency of $2 \times 10^3\,\mathrm{s^{-1}}$. A clear peak around mass 200 is indicative of a strong r-process taking place.

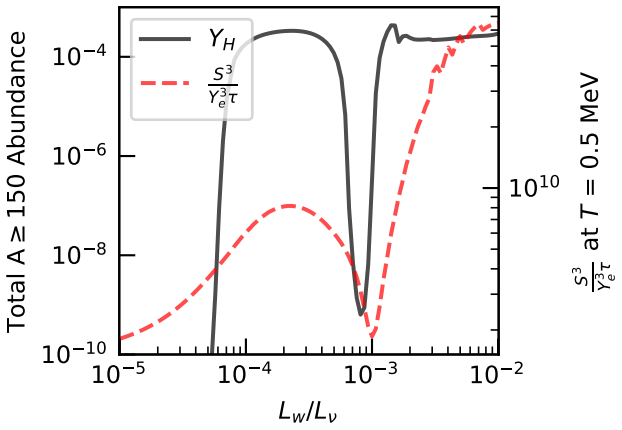

Figure 3.7 Comparison of the total, summed final abundances of all nuclides with mass $A \geq 150$ (representative of the strength of any r-process taking place) with the quantity $s^3/Y_e^3\tau_d$ evaluated when seed formation begins. The relationship between $s^3/Y_e^3\tau_d$ and Y_H is necessarily approximate due to the presence of wave heating during seed formation. The relationship found in Hoffman et al. (1997) was derived under the assumption of constant entropy, which is not generally true in our models. Nevertheless, we still observe a strong correlation between the two quantities, which helps to provide a qualitative explanation for the variation in heavy element nucleosynthesis near $L_w/L_\nu = 10^{-3}$. These results are for the same parameters as those in Figure 3.6, with a finer grid in L_w/L_ν.

Despite entropy no longer being constant during seed formation, we do observe a fairly strong correlation between r-process strength and this quantity. We find that as the wave luminosity is increased, τ_d decreases slightly faster than the entropy, but eventually asymptotes to a minimum value of a few times 10^{-4} s. The entropy continues to steadily decrease, which creates the trough in $s^3/Y_e^3\tau_d$ as a function of L_w and gives rise to the window of inhibited r-processing we observe around $L_w/L_\nu = 10^{-3}$. At higher L_w, shock heating begins prior to alpha recombination, drastically increasing the entropy. This, coupled with the reduced electron fraction at high L_w, reinvigorates a strong r-process.

Second, we consider the impact of varying ω on gravito-acoustic NDW nucleosynthesis. As was noted above, increasing ω results in an earlier activation of shock heating. In Figure 3.8, we show the final abundances for $M_{\rm NS} = 1.5\,M_\odot$, $L_\nu = 3 \times 10^{52}\,{\rm erg\,s^{-1}}$, and $L_w/L_\nu = 10^{-3}$. For $\omega < 10^4\,{\rm s^{-1}}$, the nucleosynthesis is similar to the models with $L_w/L_\nu \approx 10^{-3}$ that efficiently form seed nuclei, as discussed in the preceding paragraphs. Comparing to Figure 3.4, shock heating begins only after the beginning of seed formation and therefore the resulting increase in entropy

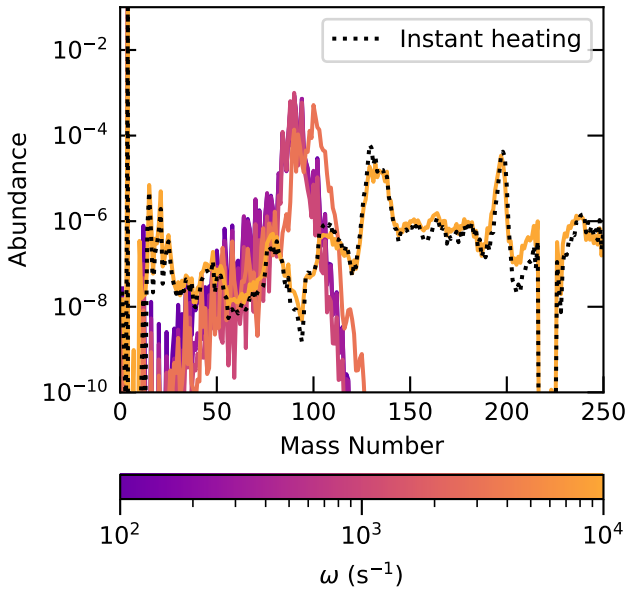

Figure 3.8 Final abundances for the NDW profiles shown in Figure 3.4. For high frequencies, the shock heating begins early enough to drive a strong r-process even for a 1.5 $M_\odot$ neutron star. Instantaneous shock formation is illustrated by the black dashed line, showing the final abundances for a wind that immediately experiences shock heating from waves with $\omega = 2 \times 10^3$ s^{-1}.

only has a limited impact on the nucleosynthesis. On the other hand, for the largest frequency considered ($\omega = 10^4$ s^{-1}), a full r-process pattern extending through the third peak is produced. Here, the wave heating due to weak shocks begins before the start of seed formation. Therefore, the substantial increase in the entropy inhibits seed formation, and leaves a large neutron-to-seed ratio when alpha capture ends. This is mainly driven by the impact of ω on the shock heating activation radius, and less so by the variation in l_d with ω. This is illustrated by the model shown in Figure 3.8 that assumes $\omega = 2 \times 10^3$ s^{-1} but an instantaneous activation of shock heating. This results in nucleosynthesis that is very similar to the $\omega = 10^4$ s^{-1} model.

Therefore, as a limiting case given the uncertainty in the shock activation radius and to compare to previous work (Suzuki & Nagataki, 2005; Metzger et al., 2007), we show in Figure 3.9 final abundances for varied L_w/L_ν for $\omega = 2 \times 10^3$ s^{-1}, $M_{\rm NS} = 1.5\,M_\odot$, $L_\nu = 3 \times 10^{52}$ ergs^{-1}, but with instantaneous activation of the shock heating. The results are noticeably different than those shown in Figure 3.5, which shows models with the same parameters but without instantaneous shock heating. For instantaneous activation, the average mass of the abundance distribution increases

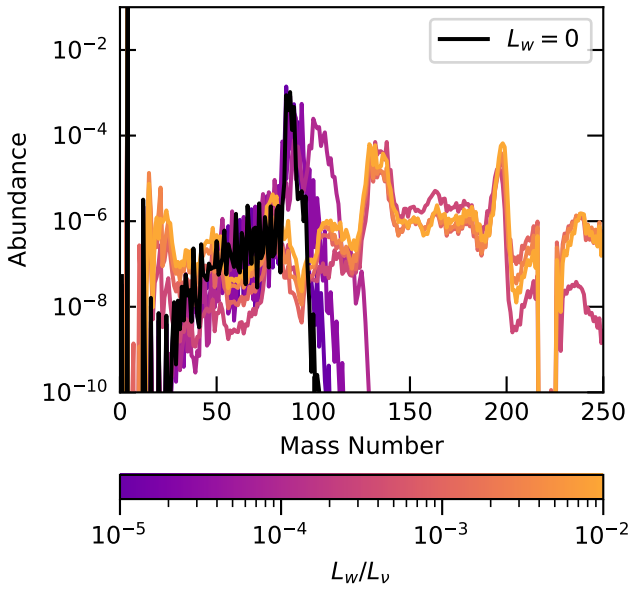

Figure 3.9 Final abundances using the same parameters as in Figure 3.5, but assuming that shock heating begins instantaneously in the wind. We see that a strong r-process takes place even for moderate L_w.

monotonically with L_w/L_ν and for even moderate wave luminosities is able to produce a full r-process. This illustrates that uncertainty in the shock formation radius translates into significant uncertainty in the predicted nucleosynthesis for gravito-acoustic NDWs.

To illustrate the important impact of the reduced electron fraction from the wave contributions, we show in Figure 3.10 abundance distributions from a wind with $M_{NS} = 1.9\,M_\odot$, $L_\nu = 6 \times 10^{52}\,\mathrm{erg\,s^{-1}}$, and $Y_{e,\mathrm{eq}} = 0.52$. In the absence of wave effects, the neutrino spectrum used here should preclude any r-processing whatsoever. The wind would undergo α-recombination, leaving only free protons to capture onto seed nuclei. However, with wave effects included, we find similar r-processing regimes to those obtained with neutrino energies tuned to $Y_e = 0.48$. In the wave stress regime, with $5 \times 10^{-4} \lesssim L_w/L_\nu \lesssim 5 \times 10^{-3}$, the change in Y_e is not large enough to make the wind neutron rich, but the faster outflow caused by the wave stress prevents a robust α-recombination from occurring. R-process elements are then synthesized from the remaining free neutrons in the wind, despite the wind being overall proton-rich. This gives rise to the suppressed, actinide-free r-process patterns in Figure 3.10. Note that charged-current neutrino interactions are not being considered in these calculations; we could expect to see heavy nucleosynthesis via

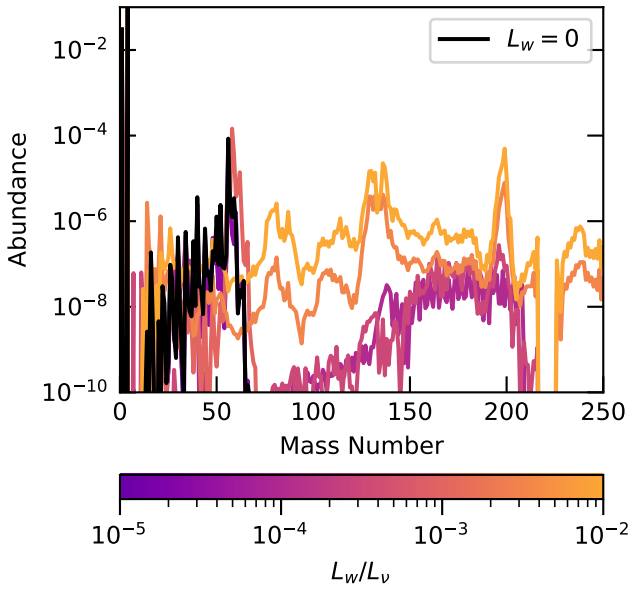

Figure 3.10 Final abundances using the same parameters as in Figure 3.6, but with antineutrino energies tuned to $Y_{e,\mathrm{eq}} = 0.52$. We see r-processing regimes appear, despite a neutrino spectrum that would otherwise have precluded r-processing entirely.

the νp-process if they were. Between the r-processing regimes, we again find a region where the combined entropy and dynamical timescale in the wind favor strong seed formation and thus no r-processing, regardless of Y_e or an inhibited α-recombination. At high L_w, the wind becomes neutron-rich again, and early wave heating suppresses seed formation enough to drive a strong r-process. Despite a neutrino spectrum predicting a proton-rich wind, a high wave luminosity can allow a strong r-process to proceed. This will be explored and elaborated further in chapter 4.

3.4 Parameter Study

Our investigation thus far has demonstrated that wave effects can allow for strong NDW r-processing for certain parameter sets. To better quantify the sensitivity of r-processing to different parameters, and to determine how common it is likely to be, we survey the likely parameter space in PNS mass, neutrino luminosity, and wave luminosity. In Figure 3.11, we show the total final abundance of nuclei with mass number $A \geq 150$ as a function of L_ν and L_w/L_ν for a variety of PNS masses. Here, we have used $Y_{e,\mathrm{eq}} = 0.48$, $\omega = 2 \times 10^3\ \mathrm{s}^{-1}$, and assumed the shock formation radius is given by equation (2.37). We find the abundance of nuclei with $A \geq 150$ to be an effective proxy for the strength of the r-process in the wind (see e.g. Figure 3.6). Two r-processing

regimes appear. For the highest neutrino and wave luminosities, shock heating begins early enough in the wind to drive a strong r-process. This shock heating regime is fairly insensitive to PNS mass but very dependent on wave frequency, which sets how early shock heating can begin in the wind. The second r-processing regime, driven by acceleration due to the wave stress, is strongly dependent on mass but insensitive to wave frequency. We see this regime emerge at a PNS mass of around $1.8\,M_\odot$, and grow to dominate the parameter space for the most massive neutron stars. The non-monotonic dependence of the average mass number of the final abundances is also visible here. At higher masses, the wave stress contribution is able to drive strong r-processes even for very low neutrino and wave luminosities, where shock heating begins too late to strongly affect the nucleosynthesis. We have also run similar calculations with $Y_{e,\mathrm{eq}} = 0.45$. These show qualitatively similar behavior to the results shown in Figure 3.11, except that the onset of wave stress-driven r-process nucleosynthesis is shifted to lower PNS mass.

In order to quantify the impact of the reduced electron fraction due to the wave stress contribution, we show in Figure 3.12 the same parameter set as in Figure 3.11, but with Y_e fixed to a constant value of 0.48. We find that including a self-consistent Y_e evolution results in a noticeable broadening of the region in L_ν-L_w/L_ν space where the r-process occurs, especially the wave stress-dominated regime at lower L_w and L_ν. This is perhaps to be expected, as the change in Y_e is driven primarily by the wave stress reducing the amount of neutrino heating needed to unbind the wind material. We also observe generally higher yields of r-process material when Y_e evolution is included, due to the higher number of free neutrons available.

Finally, in Figure 3.13, we show the impact of instantaneous shock formation on nucleosynthesis across the entire parameter space (once again with $Y_{e,\mathrm{eq}} = 0.48$ and $\omega = 2 \times 10^3\,\mathrm{s}^{-1}$, and self-consistently evolving Y_e). In this case, we find third peak r-process production for nearly all considered neutrino luminosities and PNS masses when $L_w/L_\nu \gtrsim 2 \times 10^{-4}$. Although the acceleration of the wind due to the wave stress plays a role in determining the nucleosynthesis in these models, the impact of the waves is mainly driven by the shock heating that they provide.

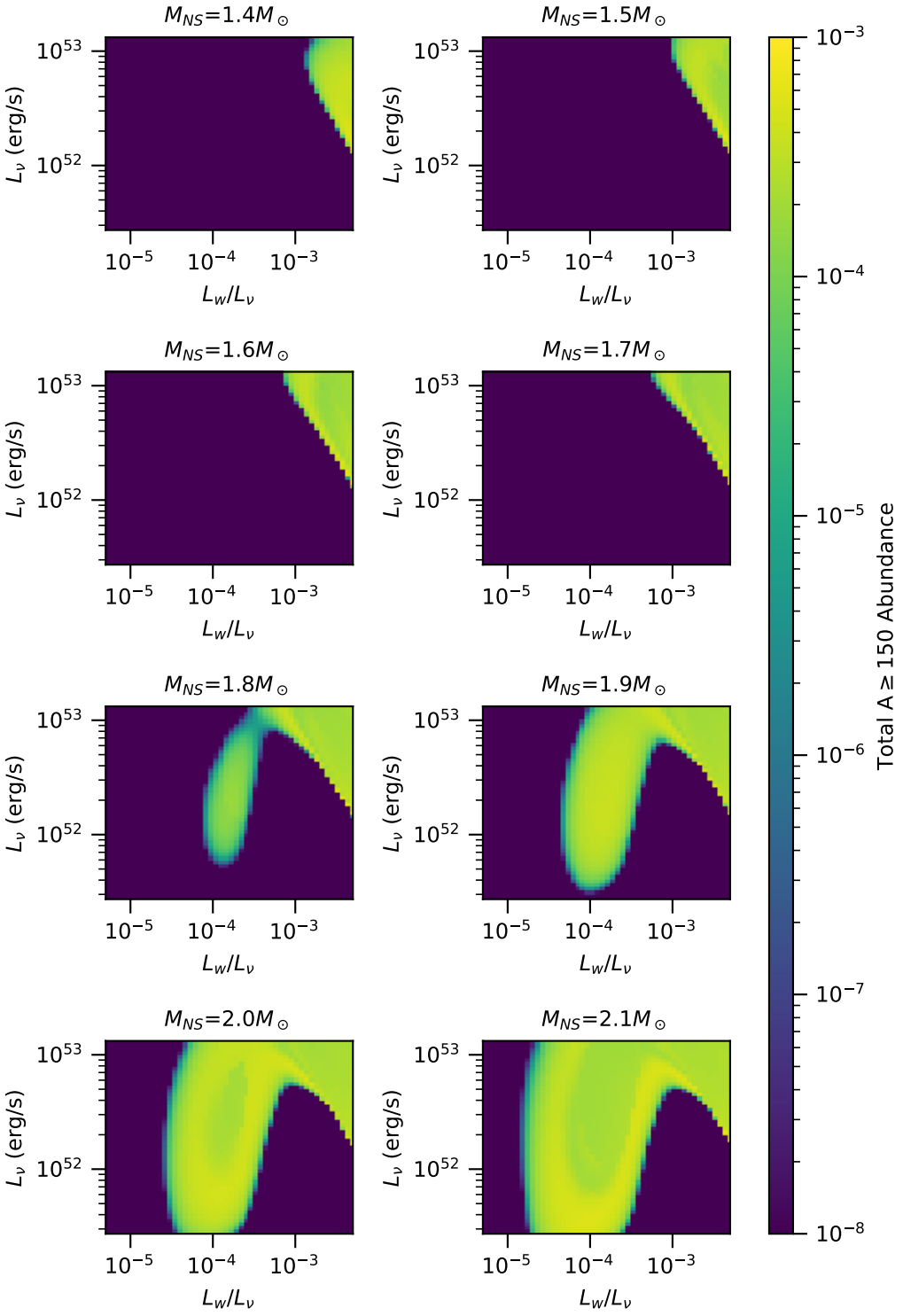

Figure 3.11 A measure of r-process strength across our parameter space, using a wave frequency of 2×10^3 s^{-1} and $Y_{e,\mathrm{eq}} = 0.48$, and using the shock heating prescription from equation (2.37). Two regimes of r-process production emerge: a region of high wave and neutrino luminosities across all masses, driven by shock heating; and a region of moderate wave and neutrino luminosities driven by the wave stress, which becomes significant at larger neutron star masses.

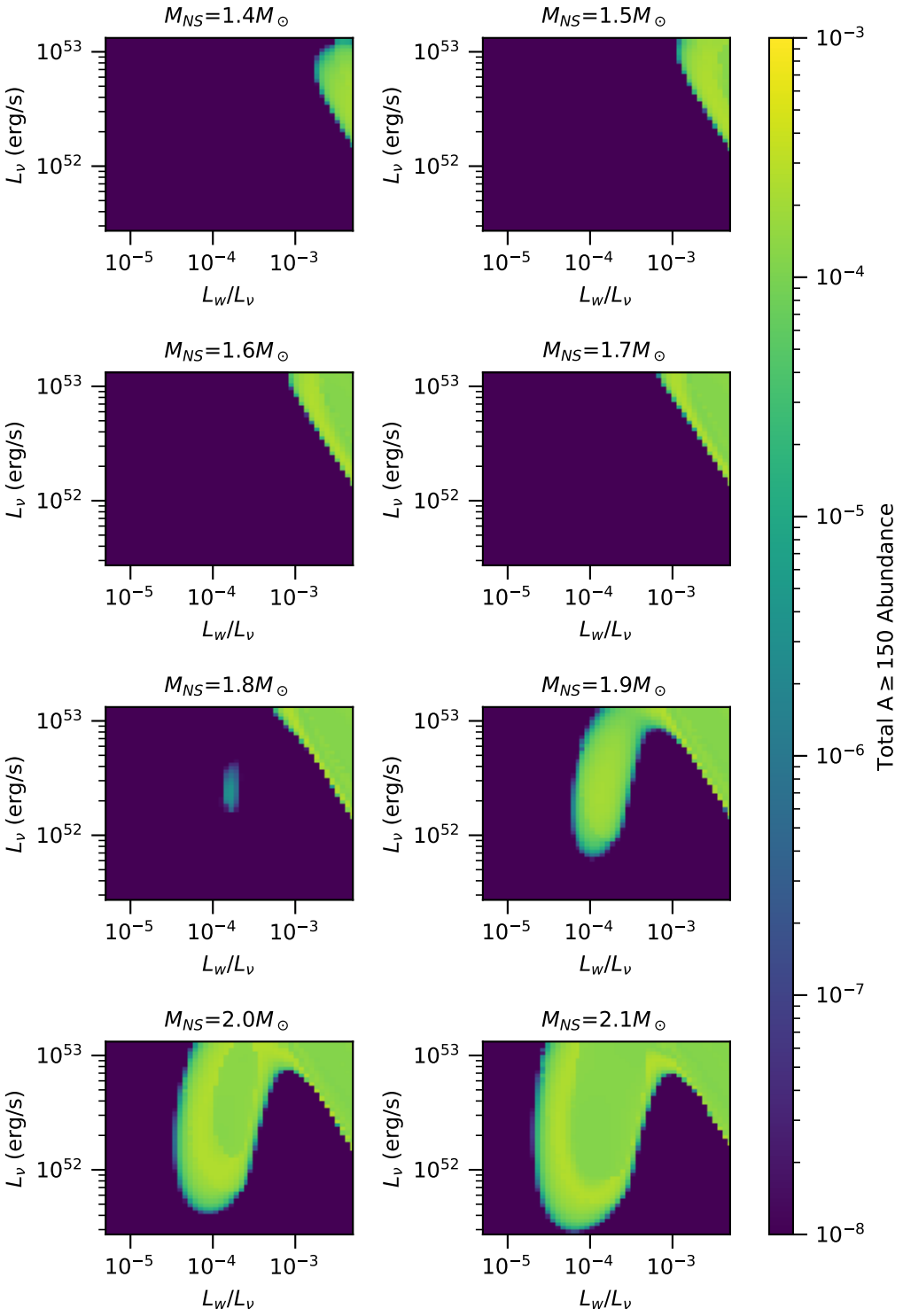

Figure 3.12 A measure of r-process strength across our parameter space, using identical parameters as Figure 3.11 but with Y_e fixed at 0.48. The same two r-processing regimes emerge, but the wave stress regime is pushed to higher masses and neutrino luminosities by the lowered neutron abundance.

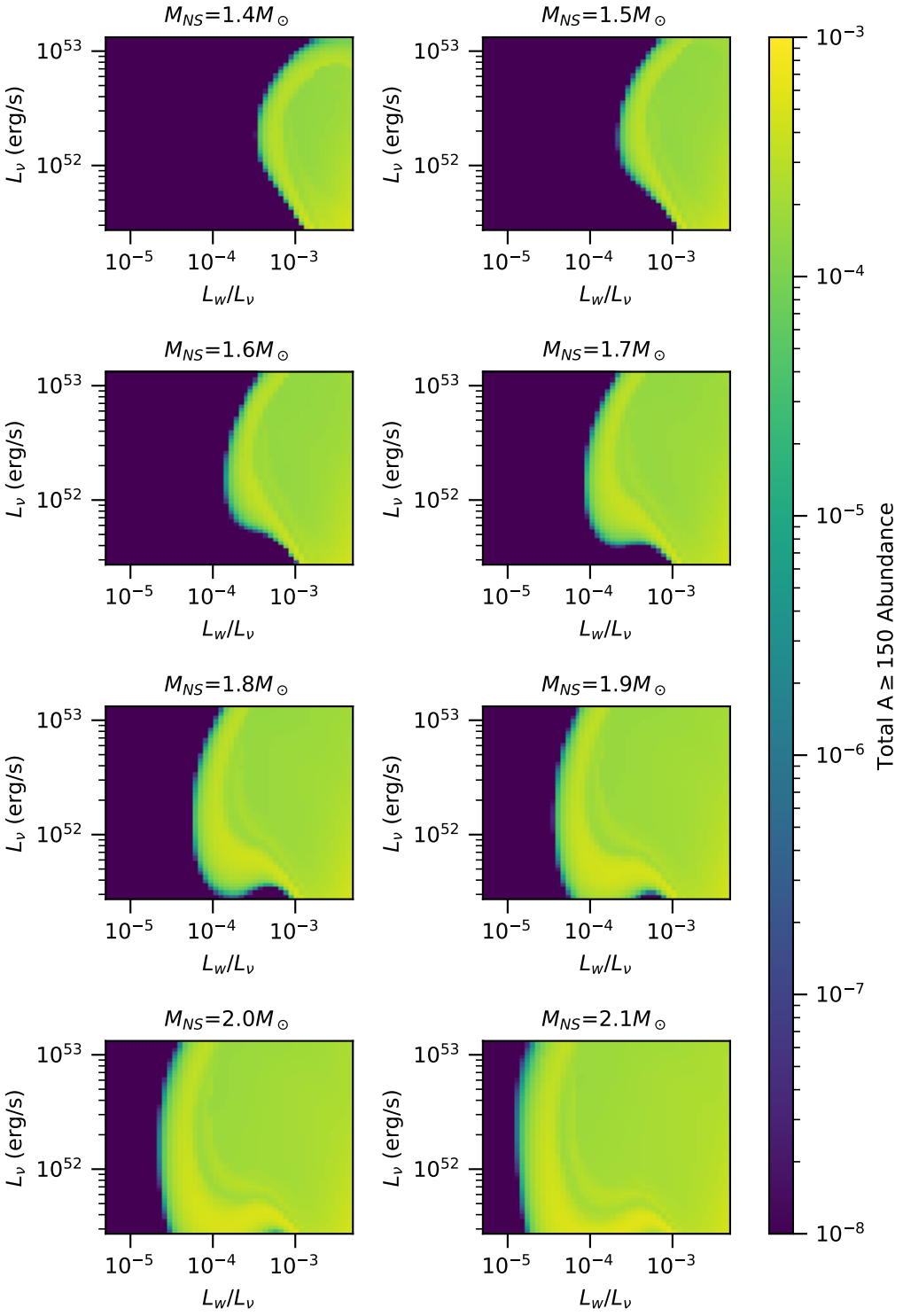

Figure 3.13 A measure of r-process strength across our parameter space, using a wave frequency of 2×10^3 s^{-1} and $Y_{e,\mathrm{eq}} = 0.48$, and assuming the waves immediately shock and begin to deposit heat into the wind. We see that for higher, but still quite reasonable wave luminosities, r-processing takes place nearly independent of PNS mass and neutrino luminosity. The r-processing parameter space broadens to very low wave luminosities at higher masses as the wave stress becomes significant.

3.5 Conclusions

In this chapter we have investigated the impact of gravito-acoustic waves launched by PNS convection on the dynamics and nucleosynthesis of the neutrino-driven wind. When these waves propagate through the NDW, they impose additional stresses on the wind and also may shock and provide an extra source of heating. Using steady-state, spherically symmetric models for the wind that include the impact of an acoustic wave energy flux, we surveyed the parameter space of the gravito-acoustic wave luminosity and frequency that is expected to be produced by PNS convection. The presence of shock heating in the wind precludes reliance upon the common predictive metric $s^3/Y_e^3\tau_d$, as entropy is no longer nearly constant during seed formation. Therefore, using the results of our hydrodynamic models, we then performed calculations of nucleosynthesis for the marginally neutron-rich compositions that may be encountered in some NDWs.

For $L_w \gtrsim 10^{-5}L_\nu$, the waves strongly impact the dynamics of the wind via two mechanisms, acceleration due to wave stresses and entropy production via wave shock heating. Acceleration of the NDW by wave stresses reduces the dynamical timescale, but also reduces the entropy and electron fraction of the wind since a faster wind has less opportunity to undergo neutrino heating. Depending on L_w/L_ν, this competition between reduced dynamical timescale and reduced entropy can make conditions more or less favorable for strong r-process nucleosynthesis.

Similarly to previous work (Suzuki & Nagataki, 2005; Metzger et al., 2007), we find that if the wave energy is deposited (in our case through shock heating) before r-process seed nucleus formation begins, the entropy of the wind at seed formation is substantially increased. This in turn results in limited seed formation and more favorable conditions for producing nuclei in the third r-process peak. Here, we found that the exact position of shock formation has a strong impact on the final nucleosynthesis. If wave shock heating begins before a temperature of around 7 GK, the final nucleosynthesis is strongly impacted and even NDWs with modest wave luminosities and fiducial PNS masses can produce a solar-like r-process pattern. If wave shock heating begins below this temperature range, its impacts on nucleosynthesis are muted. For gravito-acoustic waves, the radius of shock formation depends on their frequency, so higher frequency waves are likely to have

a larger impact on nucleosynthesis. For higher PNS masses, wave stress contributions can still drive a strong r-process even if shock heating begins too late to affect seed formation.

At high wave luminosities ($L_w/L_\nu \geq 10^{-3}$), the electron fraction can also be reduced by up to almost 10% as a result of gravito-acoustic wave acceleration of the NDW. This wave-induced reduction in Y_e broadens the regions of the parameter space over which the r-process occurs and can even cause an r-process to be produced (if conditions are otherwise favorable) in winds with neutrino spectra predicted to result in proton-richness.

CHAPTER 4

PROTO-NEUTRON STAR CONVECTION AND THE νP-PROCESS

The contents of this chapter are adapted from Nevins & Roberts (2024), which has been published in The Monthly Notices of the Royal Astronomical Society.

4.1 Background

Historically, the r-process has been the focal point of discussion regarding heavy element nucleosynthesis. There are, however, other channels by which the heavy elements can be formed. In neutrino-rich environments, the νp-process is the most promising of these. The νp-process was first proposed by Fröhlich et al. (2006) as a primary nucleosynthetic process that is active in neutrino-rich environments like the NDW. The νp-process, similar to the rp-process, forms heavy nuclei by proton captures onto seed nuclei followed by beta decays toward stability. Unlike the r-process, which can proceed to the dripline relatively uninhibited regardless of atomic number, Coulomb repulsion forces the rp-process to proceed closer to stability. This results in longer β-decay lifetimes for certain waiting-point nuclei, and when charged-current neutrino reactions are neglected it is impossible for the classical rp-process to form nuclei heavier than ^{64}Ge in the NDW due to its long β decay lifetime (Pruet et al., 2005). Waiting-point nuclei like ^{64}Ge can be bypassed, however, by capturing free neutrons created by charged-current antineutrino interactions on free protons. This modified rp-process, called the νp-process, potentially allows for formation of heavy elements up to $A = 100$ and beyond with even a small flux of free neutrons. Since the primary nucleosynthesis flows will be on the proton-rich side of stability, this process could be the source of p-nuclei such as ^{92,94}Mo and ^{96,98}Ru. The source of these nuclei and their relative abundances have been problematic for some time (e.g., Arnould & Goriely, 2003), but a νp-process in the NDW has been shown to be a viable source for at least some of these nuclides (Wanajo, 2006; Bliss et al., 2018b). Figures 4.1 and 4.2 show entropy and final abundance curves for a fiducial proton-rich wind absent any wave effects. We find, as in the neutron-rich case, the expected dependence of asymptotic entropy on mass. Our nucleosynthesis calculations are in general agreement with Pruet

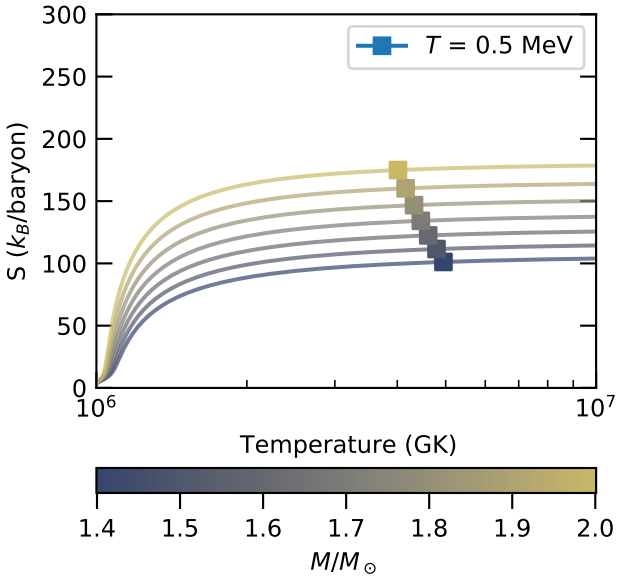

Figure 4.1 Entropy versus radius for PNSs of varying mass, with the total neutrino luminosity (in all flavors) fixed to a fiducial value of 3×10^{52} erg s^{-1}, and $L_w = 0$.

et al. (2006) and Wanajo et al. (2011), with heavy element synthesis terminating around $A = 120$ for high entropy winds.

While there remains substantial uncertainty in the neutrino spectrum of cooling PNSs, several recent studies have indicated that the wind becomes increasingly proton-rich at late times (e.g. Martínez-Pinedo et al., 2014; Fischer et al., 2020; Pascal et al., 2022). Convection in the PNS, which Nagakura et al. (2021) recently showed to be significant across a broad range of progenitors for the first few seconds of PNS lifetime, also seems to lead to more proton-rich NDWs (Pascal et al., 2022). This may be counteracted, however, by the mechanical effects of convection-driven waves accelerating the NDW, reducing neutrino captures and leading to a more neutron-rich wind (chapter 3). Nonetheless, the growing consensus over the last decade has been that the NDW is likely to be either slightly neutron-rich or proton-rich at earlier times, becoming increasingly proton-rich at late times. A proton-rich NDW naively should not undergo an r-process, but the νp-process is likely to be active instead and may allow for the formation of heavy nuclei.

A number of parameter studies have explored how the hydrodynamic conditions of the wind affect a possible νp-process (e.g. Pruet et al., 2006; Wanajo, 2006; Wanajo et al., 2011; Arcones et al., 2012; Eichler et al., 2017). As in the case of the r-process, the entropy and dynamical

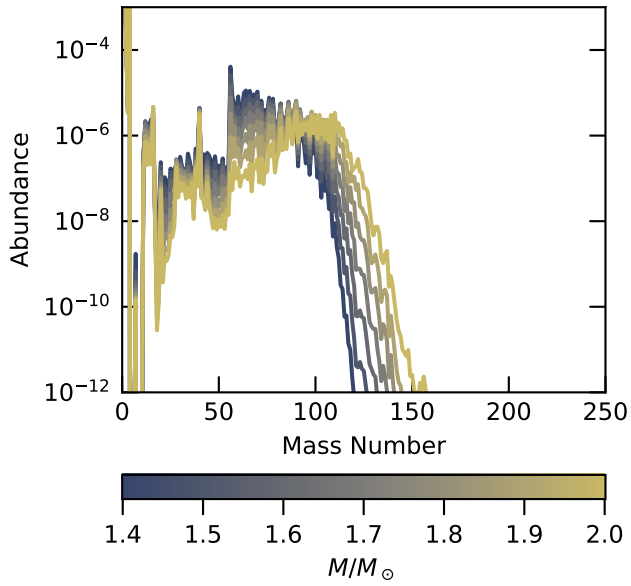

Figure 4.2 Final abundances for the wind profiles shown in figure 4.1, in the absence of wave effects (i.e., $L_w = 0$). We find some limited heavy element formation up to about $A = 130$, with modest PNS mass dependence. Higher PNS masses lead to higher asymptotic entropies in the wind, which are generally favorable for heavier element nucleosynthesis.

timescale of the wind play key roles in determining the ratio of free nucleons to seeds, which places a natural limit on how heavy of nuclei can be formed (Wanajo, 2006; Wanajo et al., 2011). The electron fraction also affects this ratio, both by dictating how many free nucleons are left after α recombination (assuming a complete α recombination), and by determining the number of free protons which can undergo antineutrino capture and transform into neutrons (Wanajo et al., 2011; Eichler et al., 2017). In chapter 3, we found that the presence of gravito-acoustic waves can substantially increase the entropy of the wind once the waves begin to shock, possibly allowing a νp-process to proceed to higher mass numbers as seed formation is inhibited. However, the additional heating and momentum flux provided by the waves had the additional effects of reducing the dynamical timescale of the wind and reducing the electron fraction, driving the wind towards neutron-richness. The reduced electron fraction will likely inhibit a strong νp-process by reducing the potential neutron flux. The effect of a faster outflow is not immediately clear. While it will reduce the efficiency of seed formation (see chapter 3), it will also reduce the amount of possible antineutrino captures in the wind, and thus the available neutron flux. A third key factor is the wind

termination shock, when the NDW impacts the slower-moving ejecta behind the main supernova shock. The νp-process is most efficient at temperatures between 1.5 and 3 GK, and a termination shock within this temperature range will prolong efficient νp-processing.

Our aim in this chapter is to explore the effect of gravito-acoustic waves on heavy element nucleosynthesis in proton-rich winds. We anticipate this will primarily affect nucleosynthesis via the entropy and electron fraction, but we will also briefly explore the role of the wind termination shock in the presence of these waves. We are mainly interested in two aspects of heavy nucleosynthesis: how the active nucleosynthetic processes are affected by the presence of these waves; and what the heaviest elements are that can be formed in a proton-rich wind affected by gravito-acoustic waves. Understanding the impact of waves on the νp-process has the potential to impact our understanding of both the origin of the heavy elements generally, and the origin of the light p-nuclides ^{92,94}Mo and ^{96,98}Ru specifically. Given the significant impact these waves can have in a marginally neutron-rich wind, up to driving a full solar-like r-process, we present here a similar parameter study considering how these waves affect a proton-rich wind and the strength of the νp-process there. We find that the presence of gravito-acoustic waves in the NDW has a substantial impact on νp-process nucleosynthesis and can allow much heavier elements to be formed than would otherwise be possible.

The model and parameter space explored in this chapter are identical to those in chapter 3, with two important differences. First, the antineutrino energies in this chapter are tuned to produce $Y_{e,\mathrm{eq}} = 0.6$ to simulate a proton-rich wind (unless otherwise stated), based on simulations such as Pascal et al. (2022). Second, the SkyNet reaction network is adjusted to include the following charged-current neutrino and antineutrino interactions on nucleons:

$$\nu_e + n \longleftrightarrow e^- + p$$

$$\bar{\nu}_e + p \longleftrightarrow e^+ + n.$$

These were neglected in chapter 3, as they had no noticeable effects on nucleosynthesis in a neutron-rich wind. They are however necessary to capture a possible νp-process.

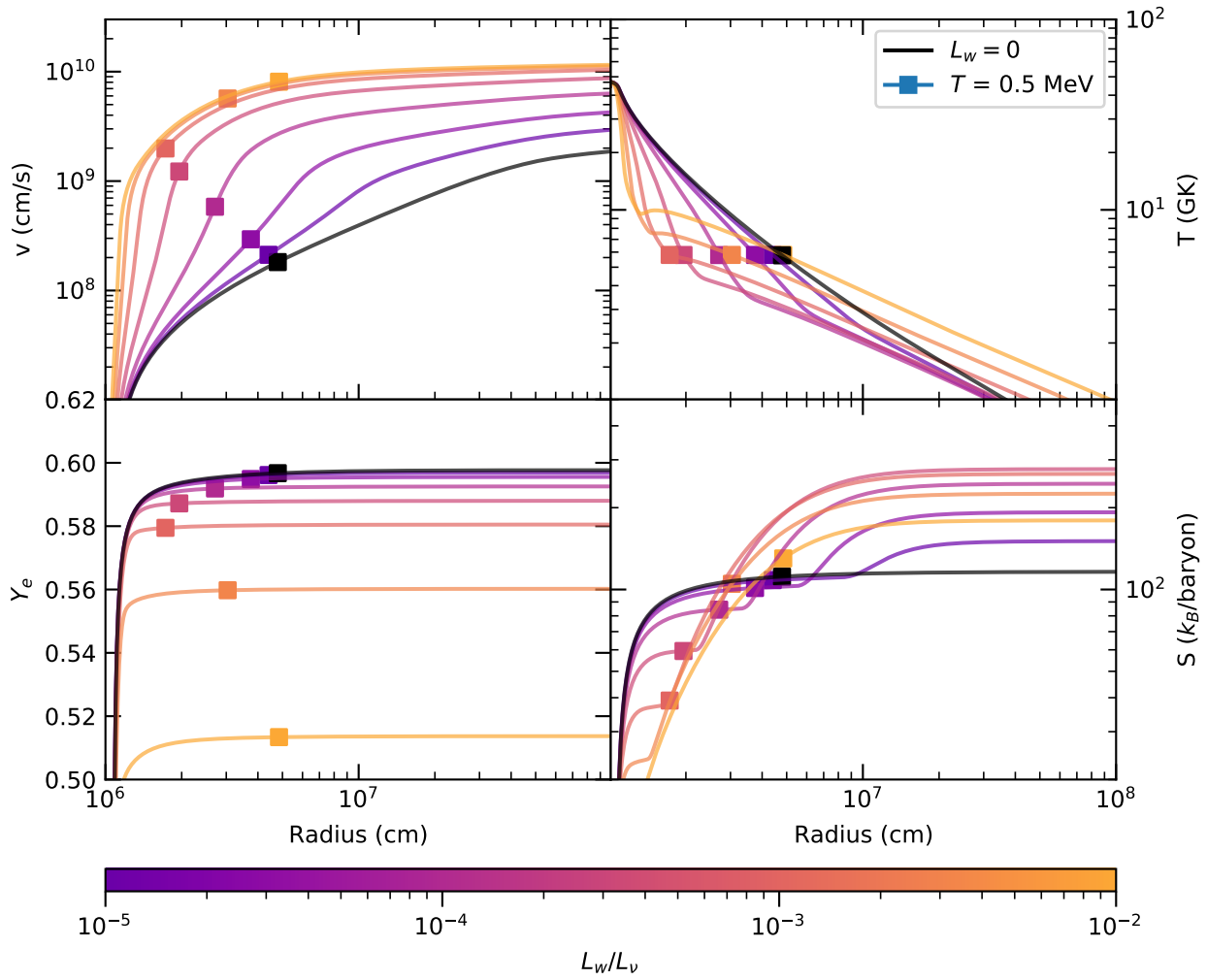

Figure 4.3 Radial profiles of the velocity, electron fraction, temperature, and entropy in the NDW. Different lines correspond to different L_w. Other parameters in the wind models were fixed to $M_{\rm NS} = 1.5\,M_\odot$, $L_\nu = 3 \times 10^{52}\,{\rm erg\,s^{-1}}$, and $\omega = 2 \times 10^3\,{\rm s^{-1}}$. The approximate beginning of seed formation at $T = 0.5\,{\rm MeV}$ for each model is marked with a square.

4.2 Wind Dynamics

Figure 4.3 shows a set of profiles describing the behavior of the NDW in the presence of wave effects for a fiducial parameter set. Our results are expectedly similar to those in chapter 3, with the exception of the increased electron fraction due to the antineutrino energies we assume here. As the wind is heated and accelerated by high wave luminosities, the number of neutrino captures required to unbind the material decreases, preventing the electron fraction from reaching its neutrino capture rate-equilibrium value of $Y_{e,\rm eq} = 0.6$. At the very highest wave luminosities, these winds become almost neutron-rich, despite the assumed neutrino spectrum. This reduction

in Y_e will have a substantial impact on the νp-process in these models, as fewer free protons will be available to produce neutrons via antineutrino captures after seed nucleus formation (Wanajo et al., 2011).

Another important feature to note is the onset of shock heating, visible as a sharp increase in the entropy. For higher wave luminosities, this takes place near or before the onset of seed nucleus formation at approximately 6 GK. We also see a clear acceleration of the wind as the wave luminosity is increased, reducing the dynamical timescale over which seed nuclei can form. Results for a more extreme parameter set, with higher mass and L_ν, are qualitatively similar, with one notable difference being higher Y_e at large L_w. Increasing the neutrino luminosity can counteract the reduction in neutrino captures caused by high L_w, pushing the electron fraction closer to its equilibrium value. A high wave luminosity coupled with a low neutrino luminosity could result in a neutron-rich wind, even though the neutrino spectrum dictates a proton-rich equilibrium Y_e.

4.3 Nucleosynthesis

We now consider the nucleosynthesis resulting from the wind models described in the preceding section. Figure 4.4a shows the final abundances produced by the fiducial wind profiles shown in figure 4.3. Two distinct families emerge in the abundance patterns. For low to moderate L_w, we see a structure that is generally similar to the νp-process patterns that emerge from the $L_w = 0$ case, with a broad peak near $A = 100$ that shifts towards higher mass numbers with increasing L_w. As in the neutron-rich case, heavy nucleosynthesis is suppressed in a small window near $L_w/L_\nu = 10^{-3}$ due to competition between reduced entropy and reduced dynamical timescale causing increased seed formation (see chapter 3). At $L_w \gtrsim 10^{-3} L_\nu$, the waves shock prior to seed formation, allowing again for heavier nucleosynthesis. We see what could be described as a suppressed r-process emerge, reaching to mass numbers near $A = 210$.

For a more extreme parameter set, with higher mass and L_ν, we observe similar abundance families. Figure 4.4b shows the abundances produced by this parameter set with a higher PNS mass ($M_{\rm NS} = 1.9\,M_\odot$) and neutrino luminosity ($L_\nu = 6 \times 10^{52}\,{\rm erg\,s^{-1}}$). Under these conditions, the

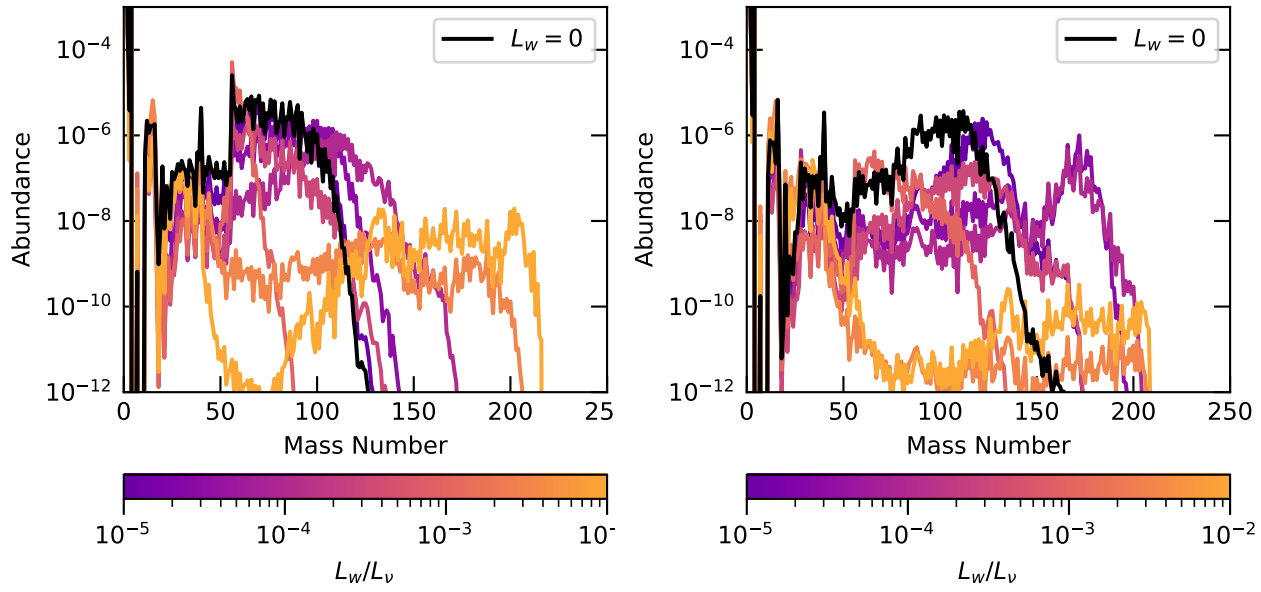

(a) Fiducial parameter set

(b) Extreme parameter set

Figure 4.4 Final nucleosynthesis patterns for varied wave luminosities, with other parameters held constant. We assume a wave frequency of $\omega = 2 \times 10^3\,\mathrm{s}^{-1}$ for both panels. *Left*: a fiducial parameter set with $M_{\mathrm{NS}} = 1.5\,M_\odot$ and $L_\nu = 3 \times 10^{52}\,\mathrm{erg\,s}^{-1}$. *Right*: a more extreme parameter set with $M_{\mathrm{NS}} = 1.9\,M_\odot$ and $L_\nu = 6 \times 10^{52}\,\mathrm{erg\,s}^{-1}$. For both parameter sets, we observe two distinct families of abundance patterns. For $L_w/L_\nu \lesssim 2 \times 10^{-4}$, the nucleosynthesis is characteristic of a νp-process, which can proceed to very high mass numbers in the high-entropy environment of a massive, $1.9\,M_\odot$ PNS. At higher wave luminosities, the nucleosynthesis shifts to a suppressed r-process pattern reminiscent of that predicted by Meyer (2002).

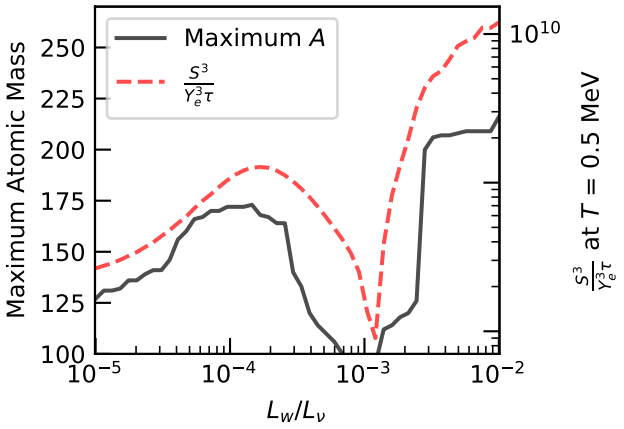

Figure 4.5 A comparison of the diagnostic quantity s^2/τ, evaluated at $T = 0.5\ MeV$, with the maximum atomic mass produced with a final abundance greater than 10^{-12}, for the same PNS parameters (M_{NS}, L_ν, ω) as in figure 4.3. We see that the strength of the νp-process is correlated with this quantity, with the fast-outflow r-process seeming to appear once it crosses a certain threshold value at high L_w.

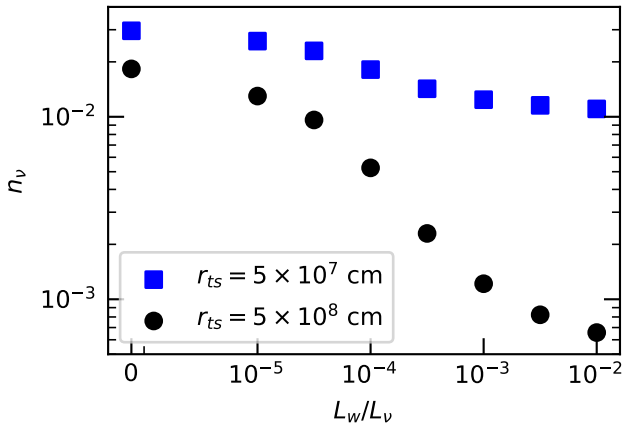

Figure 4.6 Time integrated antineutrino capture rates per baryon (n_ν) from $T = 3$ GK through the end of the simulation (see Pruet et al., 2006). The black dots correspond to the wind profiles shown in figure 4.3, which have a wind termination shock imposed at $r_{\rm ts} = 5 \times 10^8$ cm, while the blue squares show n_ν for the same set of models but with a wind termination shock imposed at 5×10^7 cm. In both cases, the additional momentum flux and shock heating from the waves reduces the number of neutrino captures as the wave luminosity is increased. An earlier wind termination shock causes the material to remain at smaller radii longer and undergo more neutrino captures.

νp-process is able to proceed all the way to $A \approx 200$, with the peak shifting to near $A = 175$ for moderate L_w. Heavy nucleosynthesis is again suppressed near $L_w/L_\nu = 10^{-3}$, and revives when shock heating begins to affect seed formation. The suppressed r-process pattern again emerges at high L_w, albeit with lower overall abundances.

The diagnostic quantity s^2/τ (similar to $s^3 Y_e^{-3} \tau^{-1}$ in neutron-rich winds; see Hoffman et al., 1997) is helpful in explaining how the strength of the νp-process varies with L_w, L_ν, and mass. The entropy dependence of seed formation is reduced by one power relative to the neutron-rich case since seed formation proceeds through the triple-alpha pathway in proton-rich conditions rather than the effective four-body reaction $^4\mathrm{He}(\alpha,\gamma)^8\mathrm{Be}(n,\gamma)^9\mathrm{Be}(\alpha,n)^{12}\mathrm{C}$. The νp-process, just like the r-process, is limited by the free-nucleon-to-seed-nucleus ratio. A higher s^2/τ implies a higher proton-to-seed ratio, which will allow heavier nuclei to be formed. Figure 4.5 shows the correlation, especially for low to moderate L_w, between s^2/τ and the heaviest nuclide formed in the wind. Although the two quantities are correlated throughout most of the L_w/L_ν range, in the range $2 \times 10^{-4} \lesssim L_w/L_\nu \lesssim 10^{-3}$, a discrepancy between the two arises. This is driven by two factors. First, the faster outflow due to wave heating at smaller radii reduces the electron fraction

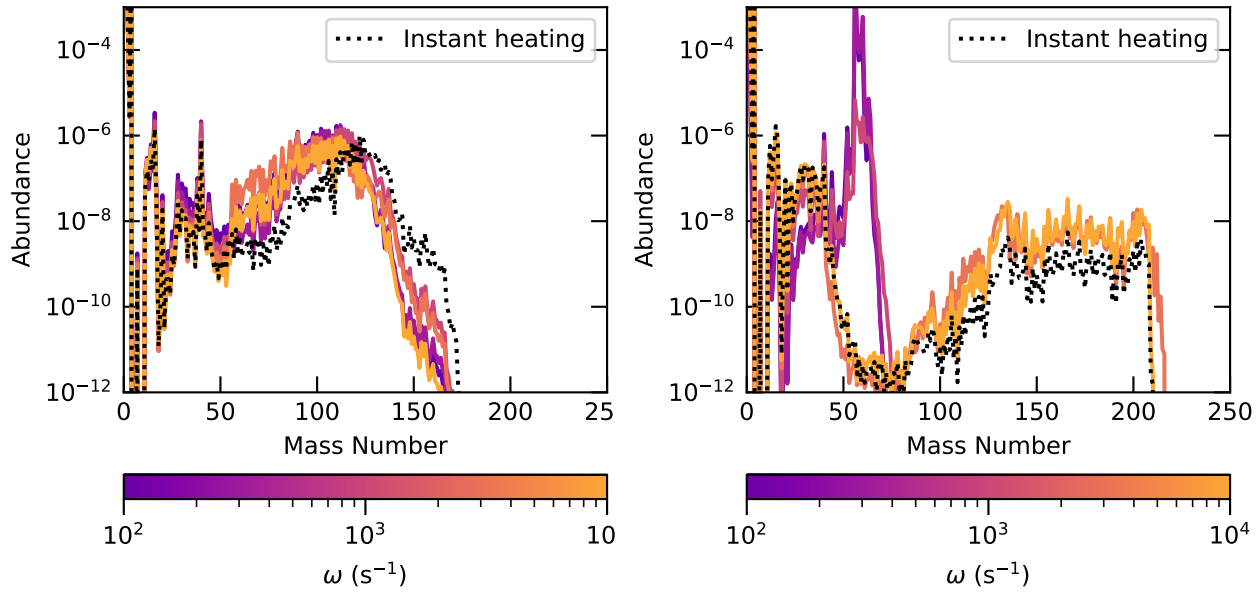

(a) νp-process ($L_w/L_\nu = 1 \times 10^{-4}$)

(b) r-process ($L_w/L_\nu = 5 \times 10^{-3}$)

Figure 4.7 Final nucleosynthesis results for a fiducial $1.5\,M_\odot$ PNS with $L_\nu = 3 \times 10^{52}\,\mathrm{erg\,s^{-1}}$, highlighting the frequency (ω) dependence of the two nucleosynthetic processes. *Left*: $L_w/L_\nu = 1 \times 10^{-4}$ to produce a νp-process. The final abundance pattern depends very weakly on wave frequency. *Right*: $L_w/L_\nu = 5 \times 10^{-3}$ to produce a fast-outflow r-process. The fast-outflow r-process requires a minimum wave frequency of approximately $\omega = 10^3\,\mathrm{s^{-1}}$ to operate, but above that minimum there is not a strong frequency dependence. For low ω, shock heating occurs after α recombination is complete and seed formation is well underway, and thus has a negligible effect on nucleosynthesis. For a sufficiently high ω, the waves shock early enough to disrupt α recombination, allowing for an r-process.

of the outflow at the beginning of nucleosynthesis (see chapter 3). Second, after seed formation a shorter dynamical timescale implies there is a shorter period of time for p(ν_e, e^+)n to produce neutrons to bypass long-lived waiting point nuclei before the r^{-2} falloff of the neutrino flux shuts off further captures. Our simulations indicate that this second effect is dominant, and the reduced electron fraction plays a lesser role. To illustrate this, figure 4.6 shows the reduction in antineutrino captures (i.e. the electron antineutrino capture rate integrated from $T = 3\,\mathrm{GK}$ through the end of the simulation) in the νp-processing regions of the wind as the wave luminosity is increased. Above this range of L_w, shock heating begins early enough to be the dominant effect in the wind and drives suppressed r-processing up to $A \gtrsim 200$.

A closer analysis of the nucleosynthesis calculations reveals that the abundance patterns we

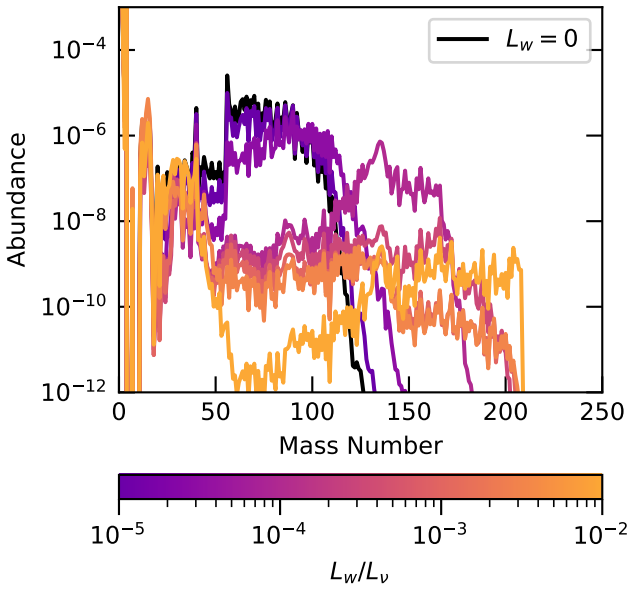

Figure 4.8 Final nucleosynthesis results, using temperature and density profiles for a 1.5 $M_\odot$ neutron star, with $L_\nu = 3 \times 10^{52}$ erg s^{-1}, $\omega = 2 \times 10^3$ s^{-1}, and assuming shock heating begins immediately in the wind (i.e. $R_s = R_{\rm NS}$). We observe a smoother transition from a νp-process at low L_w to a fast-outflow r-process at high L_w.

observe are the product of several different processes that take place at different temperatures. For lower wave luminosities, a robust α-recombination takes place, and we observe a subsequent νp-process at temperatures near 3 GK, followed by a neutron capture epoch when the wind enters (n, γ) - (γ, n) equilibrium, driving the final abundances to the neutron-rich side of stability. This matches the predictions of Pruet et al. (2006) for winds with enhanced entropy. The νp-process is very entropy-dependent, so we do not see nucleosynthesis up to $A = 200$ in the relatively low-entropy fiducial case. At higher PNS masses (i.e. higher entropies) it can proceed farther, and produces the peak near $A = 175$ that we see in figure 4.4b. In the range $2 \times 10^{-4} \lesssim L_w/L_\nu \lesssim 10^{-3}$, we see the νp-process is curtailed in both the fiducial and extreme cases. This is due to both the increased seed formation we previously observed in this region (see chapter 3), as well as a reduction in neutron production. The additional acceleration from wave stresses reduces the number of neutrino captures at early times, keeping Y_e closer to neutron richness and reducing the number of free protons available for neutron production during νp-processing. Additionally, the faster outflow reduces the time in which neutron production via antineutrino capture can proceed, decreasing total

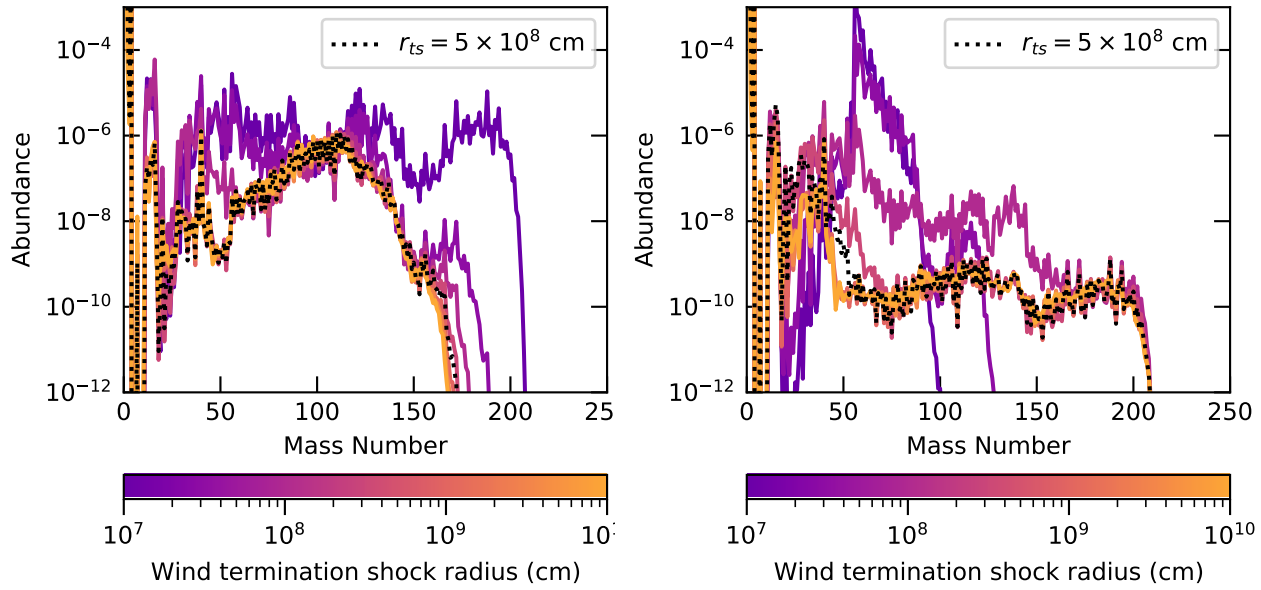

(a) νp-process ($L_w/L_\nu = 1 \times 10^{-4}$) (b) r-process ($L_w/L_\nu = 5 \times 10^{-3}$)

Figure 4.9 Final nucleosynthesis results for a fiducial 1.5 $M_\odot$ PNS with $L_\nu = 3 \times 10^{52}$ erg s^{-1} and $\omega = 2 \times 10^3$ s^{-1}, highlighting the wind termination shock location ($r_{\rm ts}$) dependence of the two nucleosynthetic processes. The $r_{\rm ts} = 5 \times 10^8$ cm case used in our other plots is highlighted for comparison. *Left*: $L_w/L_\nu = 1 \times 10^{-4}$ to produce a νp-process. An earlier shock is beneficial for the νp-process, keeping the material in the optimal 1.5–3 GK temperature window that Wanajo et al. (2011) and Arcones et al. (2012) observed. *Right*: $L_w/L_\nu = 5 \times 10^{-3}$ to produce a fast-outflow r-process. An early shock can delay α capture freezeout by keeping the material at high temperatures longer, leading to rampant seed formation and stifling the r-process. A later shock allows the wind to cool, "freezing in" the low seed count caused by the additional wave heating and allowing the fast-outflow r-process to proceed. Kuroda et al. (2008) similarly observed that a later termination shock is optimal for r-processing.

neutron production during νp-processing. This reduction is shown in figure 4.6.

At the highest wave luminosities, the early shock heating prevents a robust α-recombination phase, leaving a noticeable abundance of both free protons and free neutrons and drastically reducing seed production. Running the nucleosynthesis calculations without neutrino reactions shows that these neutrons are not created in-situ, confirming that this is not a νp-process; the bulk of the neutrons are left over from an incomplete α-recombination phase. As the temperature continues to drop, charged particle reactions freeze out and a neutron capture epoch ensues. In the fiducial parameter set (figure 4.4a), the lower neutrino luminosity leads to a lower electron fraction, providing a larger reservoir of neutrons, which results in more pronounced r-process peaks near

A = 140 and 200. In the more extreme parameter set (figure 4.4b), the higher neutrino luminosity reduces the number of free neutrons, and thus the r-process pattern is more suppressed. The abundance patterns for the high L_w case, especially those in figure 4.4b, agree very closely with those predicted by Meyer (2002) for r-processing in very fast outflows. It is important to note that, as figure 4.3 indicates, the r-processing here occurs in proton-rich conditions, with antineutrino energies that predict an equilibrium Y_e of 0.6.

Incidentally, reviewing the high L_w nucleosynthesis calculations for neutron-rich winds (e.g. Figure 3.5 of chapter 3) we find that this same process was operating in those winds. We did not see the same final abundance patterns because the free neutron abundance was high enough that the subsequent period of neutron capture washed out any trace of the earlier process, yielding a standard r-process abundance distribution.

4.3.1 Wave Frequency

The frequency of the waves excited by PNS convection plays an important role in determining where and how the waves will shock. Though there is substantial uncertainty in the shock mechanism in this context, we expect higher frequencies to shock earlier and deposit their energy faster than lower frequencies (see section 2.1.4.3). In figures 4.7a and 4.7b, we present a typical νp- and fast outflow r-process with varied wave frequencies, as well as one abundance profile from a wind in which we assume the waves shock instantly in the wind, to illustrate the effect of the uncertainty in the shock formation prescription. In the case of the νp-process, we see very little frequency dependence because of the low wave luminosity, which limits how early the shocks can form in the main prescription we assume (see chapter 3, section 3.2). Even when the shocks form instantly, the waves are not carrying enough energy to strongly alter the nucleosynthesis. Since the νp-process only operates at lower wave luminosities ($L_w/L_\nu \lesssim 10^{-3}$), we expect this to be consistent across the parameter space.

The fast-outflow r-process shows a stronger frequency dependence, in the form of what appears to be a minimum cutoff frequency. Because this r-process only operates at high wave luminosities ($L_w/L_\nu \gtrsim 10^{-3}$), if the waves shock early enough, they will deposit enough energy to strongly

affect the resulting nucleosynthesis. At very low frequencies, the waves do not shock until seed formation has already taken place, so the r-process is stifled. Once above the cutoff frequency, the waves shock early enough to disrupt α recombination, and the final abundance pattern is not strongly affected by further increasing the frequency.

There is substantial uncertainty in the shock mechanism for the waves we are considering, and they may shock much earlier than predicted (see figure 10 and the discussion in chapter 3). In figure 4.8, we present abundance profiles assuming the waves shock instantly, so that any heat deposition will affect every stage of nucleosynthesis. We observe what appears to be a smoother transition from a νp-process at low wave luminosities, to a fast-outflow r-process at high wave luminosities, with higher free neutron abundances altering the abundance patterns as L_w is increased.

4.3.2 The Role of the Wind Termination Shock

Because of the strong dependence of the νp-process on the location of the wind termination shock found in previous work (e.g. Arcones et al., 2012), we now turn our attention there. Figure 4.9a shows how the final abundance pattern for a typical νp-process varies with the location of the wind termination shock. Previous studies have found that an early wind termination shock at temperatures of around 2 GK is optimal for facilitating a strong νp-process. Our wind models cool very rapidly, so this optimal temperature range occurs very early on. We can see that, as expected, the smallest shock radius is favored for the νp-process. An early shock keeps the wind at higher temperatures and smaller radii longer, which allows more time for both proton captures and neutron production via antineutrino capture to proceed (see figure 4.6).

For the fast-outflow r-process, a later shock is optimal. This is in at least qualitative agreement with Kuroda et al. (2008), who observed less robust r-processes with early shock radii, and little change in abundance patterns once the radius was increased above 3000 km. We see in figure 4.9b that the r-process cannot proceed for very early termination shocks. A sufficiently early termination shock can occur at high enough temperatures to restart α capture reactions after their initial freezeout, and the slow-moving shocked material takes much longer to cool than the fast-moving wind. Seed formation proceeds rapidly in such cases, and we see a robust α process

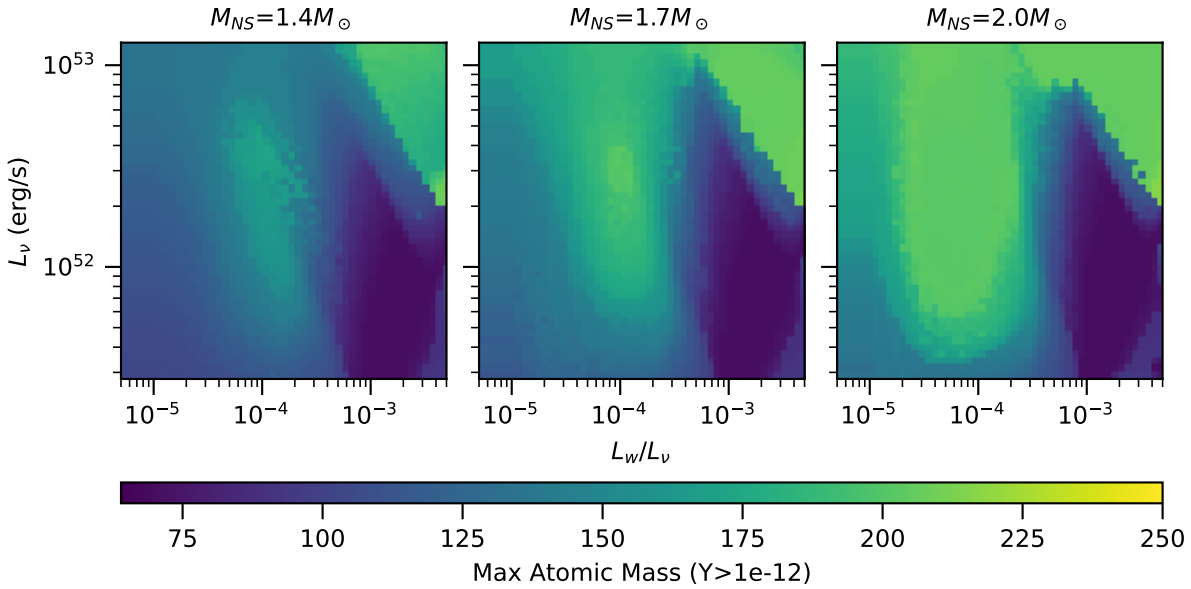

Figure 4.10 This plot shows the highest atomic mass produced in a significant amount ($Y \geq 1{\times}10^{-12}$), giving a measure of how far heavy element nucleosynthesis is able to proceed. We observe similar heavy nucleosynthesis regimes as in the neutron-rich case, with a mass-dependent wave-stress driven νp-process regime at moderate wave luminosities, and a shock-heating driven, mass-independent r-processing regime at high L_w and L_ν. We do not observe any actinide production in these models.

emerge, forming large amounts of iron-peak elements and precluding an r-process. Once the shock is moved beyond approximately 1000 km the r-process can proceed with full vigor, and when the shock is moved beyond approximately 3000 km the final abundance pattern is no longer sensitive to its location.

4.4 Parameter Study

In figure 4.10, we show a plot of the maximum atomic mass that is produced with a final abundance greater than 10^{-12} for a given parameter set. This gives a helpful measure of how far the νp-process is able to proceed as a function of PNS mass, neutrino luminosity, and wave luminosity as a fraction of neutrino luminosity. For these plots, we have taken $\omega = 2000\,\mathrm{s}^{-1}$, $Y_{e,\mathrm{eq}} = 0.6$, $r_{\mathrm{ts}} = 5 \times 10^8\,\mathrm{cm}$, and used the shock prescription in equation (2.37). We observe similar nucleosynthesis regimes as in the neutron-rich case in chapter 3. For high L_ν and L_w, we see very heavy nuclei being formed as shock heating begins early enough to inhibit seed

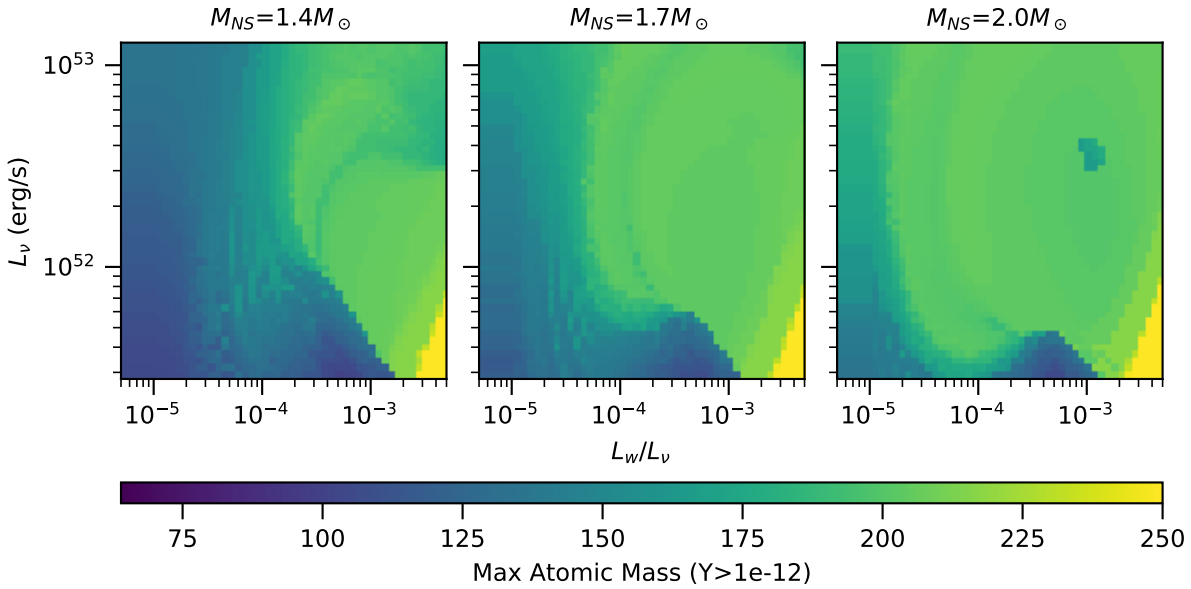

Figure 4.11 This plot is the same as figure 4.10, but assuming that shock heating begins immediately in the wind. Similar to the neutron-rich case, we see a smoother transition between and blending of the wave-stress and shock-heating regimes of heavy nucleosynthesis. The high L_w, low L_ν region of strong heavy element production is revealed to be a full r-process proceeding all the way to the actinides, as wave effects drive the wind to neutron-richness.

formation, and the high entropy and fast outflow prevent a complete α-recombination, leading to a fast-outflow r-process. Because the fast-outflow r-process depends on early shock heating by the waves disrupting α-recombination, the sharp cutoff line of this region indicates that the minimum wave luminosity to obtain such an r-process is of order $10^{50}\,\mathrm{erg\,s^{-1}}$, and is relatively independent of neutrino luminosity. We also observe no actinide production in any region of this parameter space, which could lead to an observable signature of these winds.

We also see a PNS mass-dependent nucleosynthesis regime driven by the wave stress emerge, as in the neutron-rich case. The nucleosynthesis patterns here are broadly consistent with a νp-process, and exhibit the expected correlation between the wave luminosity, the diagnostic quantity s^2/τ, and the maximum atomic mass produced shown in figure 4.5. The non-monotonic connection between wave luminosity and maximum mass produced is very clearly illustrated here. At low wave luminosities, the effect on s^2/τ dominates, and the reduction in seed formation allows more massive nuclides to form. For $L_w/L_\nu \gtrsim 5\times10^{-4}$, unless the neutrino luminosity is high enough

to make $L_w \gtrsim 10^{50}\,\mathrm{erg\,s^{-1}}$ and drive fast-outflow r-processing, the reduction in neutrino captures caused by the additional acceleration becomes dominant, and the νp-process is stifled by a lack of free neutrons. Nucleosynthesis shifts toward the iron peak, and heavy nuclides cannot form. Both the fast-outflow r-process and the νp-process benefit from higher asymptotic entropies, so we see a positive correlation between PNS mass and the maximum atomic mass nuclides formed in the wind.

Because of the uncertainty surrounding when and where shock formation will take place in the wind, in figure 4.11 we show the same parameter space as in figure 4.10, but assuming that the waves instantly shock and deposit their energy into the wind. Just as in the neutron-rich case, we see the shock-heated heavy nucleosynthesis regime (here the fast-outflow r-process) broadens in both L_w and L_ν, and the wave pressure regime becomes difficult to distinguish as it emerges. Because shock heating is assumed to begin instantly, α-recombination is affected even at low wave luminosities, and we see a smooth transition from νp-processing to fast-outflow r-processing as in figure 4.8. At high masses (i.e. higher entropies), the parameter space is dominated by heavy nucleosynthesis of some kind. Interestingly, we notice a new regime emerge when instant shock heating is assumed: for low L_ν and high L_w, the wind material becomes neutron-rich, and a full, third-peak, actinide-producing r-process appears. The rapid acceleration and additional heat provided by the waves, coupled with a low neutrino luminosity, result in a wind that undergoes comparatively few charged-current neutrino interactions and maintains a Y_e well below its equilibrium value. We emphasize again that the neutrino spectra of these proto-neutron stars predicts an equilibrium electron fraction of 0.6, yet we observe regions of the parameter space (albeit extreme) that predict a full r-process.

4.5 Conclusions

In this chapter, we have continued our exploration of the effects of convection-driven acoustic waves on nucleosynthesis in the neutrino-driven wind, now focusing on winds predicted to be proton-rich and with an eye toward the νp-process. As in chapter 3, we have surveyed the parameter space of PNS masses, neutrino luminosities, wave luminosities, and wave frequencies, as well as considering the impact of the wind termination shock and different shock heating prescriptions.

Using a steady-state, one-dimensional wind code and the SkyNet reaction network, we have performed nucleosynthesis calculations to determine the predicted abundance profiles and reaction flows expected in these winds. For the bulk of our calculations, we assume a PNS neutrino spectrum that yields an equilibrium Y_e of 0.6, in the range predicted by many recent simulations.

As in the neutron-rich case, we find that wave luminosities of $L_w \gtrsim 10^{-5} L_\nu$ have a substantial impact on wind dynamics and nucleosynthesis. At modest wave luminosities ($L_w \lesssim 10^{-3} L_\nu$), the faster expansion caused by the wave stress contribution decreases seed formation efficiency, leaving a higher ratio of free protons to seed nuclei and enhancing the νp-process. The resulting nucleosynthesis flows are able to produce elements up to mass 208 and beyond, though not reaching the actinides. This is a strong enhancement from our models that neglect wave effects, which only reach up to around mass 130.

We find these wave driven effects at modest luminosities can have competing impacts on νp-process nucleosynthesis in the NDW:

1. Gravito-acoustic wave driven acceleration and shock driven energy deposition impacts nuclear seed production for the νp-process. Acceleration of the NDW due to wave stresses both reduces the dynamical timescale and also reduces the amount of neutrino heating that occurs (which in turn reduces the asymptotic entropy of the NDW). Additionally, after the gravito-acoustic waves become non-linear and shock, they deposit heat in the NDW and increase the entropy. Since seed production in proton-rich winds depends on the parameter s^2/τ, with seed production decreasing with increasing values of this parameter, the impact of waves on seed production can behave non-monotonically with L_w. For $L_w \lesssim 2 \times 10^{-4} L_\nu$, we find the decreased dynamical timescale dominates and seed production decreases with increasing L_w. For $2 \times 10^{-4} L_\nu \lesssim L_w \lesssim 2 \times 10^{-3}$, seed production increases with L_w as the entropy reduction due to wave stresses dominates. For $L_w \gtrsim 2 \times 10^{-3} L_\nu$, wave shock heating increases both the entropy and dynamical timescale to the extent that even alpha production is impacted.

2. Acceleration of the NDW by gravito-acoustic waves reduces the time available for p($\bar{\nu}_e$, e^+)n to occur and thus reduces the total number of neutrons that are produced per seed nucleus. This reduces the maximum nuclear mass to which the νp-process proceeds, but at lower wave luminosities the effects on seed formation via the increased entropy and decreased dynamical timescale dominate. At $2 \times 10^{-4} \lesssim L_w/L_\nu \lesssim 10^{-3}$, the reduced neutron flux becomes significant enough to curtail νp-processing somewhat.

3. For larger gravito-acoustic wave luminosities, the acceleration of the NDW by these waves can reduce the number of neutrino captures that occur before alpha particle formation. Since material in the PNS atmosphere is in beta equilibrium and as a result is very neutron rich, the reduced number of neutrino captures as the outflow starts tends to decrease the proton richness of the wind. This effect was seen for neutron rich winds, where it helped to make conditions more favorable for r-process nucleosynthesis, but in proton rich winds where the νp-process might occur this effect reduces the number of free protons that are available to undergo p($\bar{\nu}_e$, e^+)n once seeds have been formed. This also contributes to the reduction in maximum nuclear mass attained by the νp-process seen for moderate wave luminosities.

At higher wave luminosities ($L_w \gtrsim 10^{-3} L_\nu$) and higher neutrino luminosities ($L_\nu \gtrsim 10^{52}$ erg s^{-1}), we find an interesting result: the early shock heating in this region of the parameter space prevents a complete α recombination phase in the wind, preserving an abundance of free neutrons much higher than the persistent abundance created by charged-current neutrino interactions. This, coupled with the reduced seed formation due to higher entropy, allows a suppressed r-process to take place, similar to that predicted by Meyer (2002) for fast-moving winds. Though this r-process does not reach to the actinides, it can reach to the third r-process peak and beyond. For a substantial region of the parameter space, we find that winds from a neutron star with a neutrino spectrum predicted to result in a firmly proton-rich wind can undergo an (albeit suppressed) r-process. When we consider an alternative prescription for the shock heating, in which the waves immediately shock upon entering the wind, not only does this region of suppressed r-processing broaden, but

we find an even more extreme possibility: the combination of acceleration due to wave stresses and additional heating from the shocked waves reduces the amount of neutrino heating needed to unbind the wind to such a degree that the wind actually becomes neutron-rich, and undergoes a full, third-peak r-process reaching the actinides. While this only occurs in a small corner of the parameter space, its mere possibility demonstrates the dramatic changes that can be caused by the presence of waves in the NDW.

CHAPTER 5

INTEGRATED NUCLEOSYNTHESIS FROM CONVECTIVE PROTO-NEUTRON STARS

5.1 Introduction

Having seen in the preceding chapters the dramatic effects convection-driven waves can have on the neutrino-driven wind, we now calculate robust predictions of the nucleosynthesis in such winds. The steady-state approximation is valid for calculating the dynamics of the wind because the properties of the PNS (mass, neutrino luminosities, convective frequency, etc.) vary slowly in comparison to the dynamical timescale of the wind. These PNS properties do change with time, however, and because NDW nucleosynthesis depends heavily on properties such as PNS mass and neutrino luminosity, the time variation of these properties must be accounted for in order to obtain accurate nucleosynthesis results.

A number of such studies have been done using parameterized models of the properties of the PNS, e.g., radius and neutrino luminosity. Arcones & Montes (2011) considered whether the NDW could explain a certain range of solar system abundances by using an integrated set of simple steady-state models with a time-varying neutrino luminosity. Wanajo (2013) examined r-process nucleosynthesis in the NDW using a series of steady-state models, with the PNS mass fixed to a set value and the neutrino luminosity (in all flavors) given by $L_\nu(t) = L_{\nu,0}(t/t_0)^{-1}$. The PNS radius was also varied as a function of the neutrino luminosity. The resulting abundances from these models were integrated with respect to time and weighted by the mass loss rate (see Equation [2.12]) to determine the total elemental abundance yields from a wind lasting 10 s post-bounce. Friedland et al. (2023) used a similar method, by combining a steady-state model with a time-dependent component and integrating a number of these models for a parameterized $L_\nu(t)$. Ekanger et al. (2022) took a more robust approach and used neutrino luminosities and energies taken from a PNS simulation done by Pons et al. (1999). Their wind models, however, were highly parameterized, and they did not appear to consider the time evolution of $R_{\rm PNS}$.

Other time-dependent factors such as PNS mass, average neutrino energies, and location of the

wind termination shock also play a key role in determining the dynamics and nucleosynthesis of the wind. Furthermore, the convective parameters examined in this work are also time-varying, and as we have shown in previous chapters, can have a dramatic impact on nucleosynthesis. Ideally, all this could be explored in full 3D simulations, and efforts are being made to do so (e.g., Zha et al., 2024; Wang & Burrows, 2024), but these simulations are limited by extreme computational complexity and cannot yet explore the full behavior of the wind, which can last ~ 10 s post-bounce. The most robust and computationally-feasible approach, at present, is to integrate NDW nucleosynthesis yields for a full, self-consistent, time-dependent PNS parameter set fed into a robust wind code, which can easily explore the full wind timescale. Such an investigation was performed by Fischer et al. (2010), who modeled the core collapse, PNS evolution, and NDW properties for a few different progenitor stars. We emulate their approach in this chapter. We extract key parameters from a robust 1D supernova code, STIR, which produces self-consistent explosions and also provides the PNS convection data we require, and then we compute a number of steady-state models with time-varying PNS parameters and integrate their yields. This integrated nucleosynthesis from our models using realistic PNS evolution from STIR provides a much more accurate picture of the nucleosynthesis in the NDW, and gives us additional insight into the effects of convection-driven waves.

5.2 Overview of STIR

Though supernovae are fundamentally 3D, the complexity and compute-time requirements of 3D simulations makes 1D, spherically symmetric models an extremely useful tool in parameter studies. A long-standing problem in 1D, however, is the explodability of the simulated stars. Historically, it was (almost) impossible to find a stellar model that would explode in 1D without some ad-hoc method of dumping energy into the core to drive the explosion[1]. One key reason is the lack of turbulence in 1D models, which acts as an additional source of pressure to support an explosion (Couch & Ott, 2015), and also has important effects on the neutrino properties (Roberts et al., 2012b). To remedy this, Couch et al. (2020) developed a 1D code, Supernova Turbulence

[1] An exception to this is the z9.6 model, a zero-metallicity 9.6 $M_\odot$ progenitor that explodes self-consistently in 1D, which we consider in this chapter.

In Reduced-dimensionality (STIR), which, like Roberts et al. (2012b), uses mixing-length theory to simulate the effects of turbulence and convection without the added complexity of increased dimensionality. This resolves both convection in the main supernova explosion, which allows for self-consistent explosions in 1D, as well as convection in the PNS. The methods used by Couch et al. (2020) did not incorporate lepton gradients in their calculations for PNS convection, however, and the resulting PNS convection did not comport with 3D simulations. Substantial improvements have now been made to STIR (Couch et al., in prep.). To briefly summarize, the major improvements are as follows.

1. A full rederivation of the STIR equations was performed, using a Favre average (Pope, 2000) of the Navier-Stokes equation. STIR is now explicitly energy-conserving, while it was only approximately so before.

2. A hybrid equation-of-state was implemented that accurately resolves the transition from NSE abundances to the Helmholtz EOS (Timmes & Swesty, 2000) as the ejecta expand and cool when the simulation is run to later times. This, combined with the Favre-averaged rederivation, allow simulations to be run to much later times than were previously possible.

3. Lepton gradients are included in the calculation of the Brunt-Väisälä frequency, which enables an accurate calculation of convection in the PNS. STIR now accurately reproduces 3D results for convection in both the explosion and the PNS.

With these improvements, STIR can now provide accurate, self-consistent PNS parameters for use in our wind code.

5.3 Integrating STIR

A number of parameters need to be extracted from STIR for our neutrino wind model. The neutrino luminosity L_ν and mean energy $\langle \epsilon_\nu \rangle$ for each flavor are explicitly reported by STIR and can easily be transferred. The PNS radius and mass are defined, respectively, as the radius and mass of the region for which the density exceeds 10^{12} g cm^{-3}. The wind termination shock occurs where the fast-moving transonic wind collides with slower-moving material at the trailing edge of

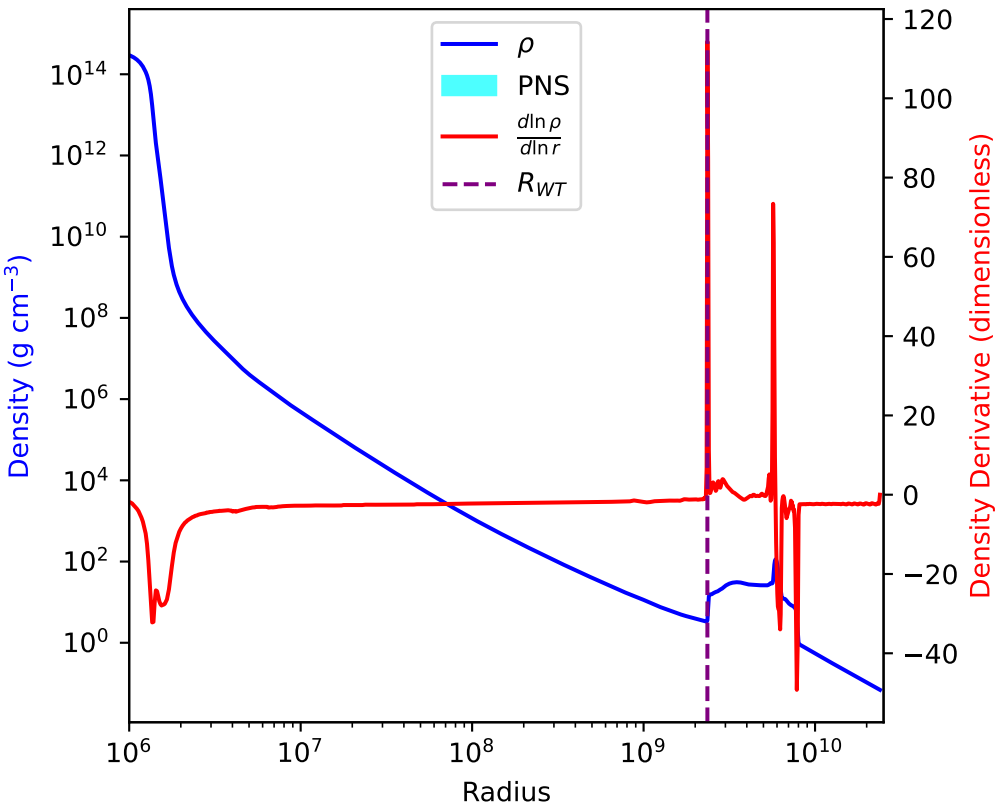

Figure 5.1 Diagram showing how the PNS radius and wind termination shock radius are determined from STIR's output, for the z9.6 progenitor without convection, 3 s post-bounce. The PNS radius is defined as the boundary of the region having density greater than 10^{12} g cm^{-3}. The location of the wind termination shock, where the supersonic wind impacts the trailing edge of the primary supernova shock, is located where the derivative of the density with respect to radius is maximized.

the primary supernova shock, which can be seen in STIR snapshots as a region of increased density in the ejecta that moves outward with time. The trailing edge of the primary shock is then easily detected as the location at which the derivative of density with respect to radius is maximized (see Figure 5.1).

5.3.1 Convection

STIR reports the convective velocity $v_{\rm con}$ as a function of radius for each timestep, which allows us to determine the initial value of L_w prior to the attenuation experienced when the waves pass through the evanescent region. Wave generation is concentrated in the outermost pressure scale height of the convective region (Goldreich & Kumar, 1990), so we take the average of the convective

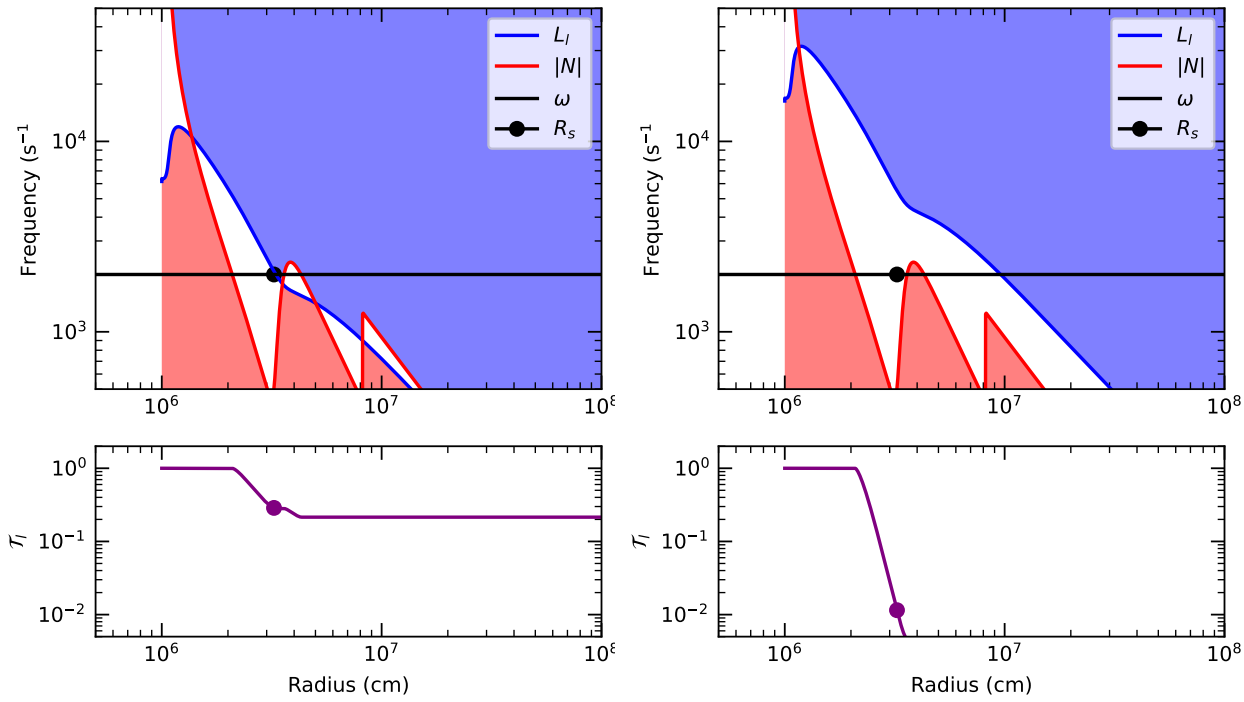

(a) $l = 2$ (b) $l = 6$

Figure 5.2 Wave branches for a fiducial PNS with $M_{\rm NS} = 1.5\,M_\odot$, $L_\nu = 3 \times 10^{52}\,{\rm erg\,s^{-1}}$, $\omega = 2 \times 10^3\,{\rm s^{-1}}$, and a low initial wave luminosity $L_w/L_\nu = 10^{-4}$ for two modes, $l = 2$ (*left*) and $l = 6$ (*right*). Where the wave frequency (black line) is in the red-shaded zone, the waves are gravitational. In the blue zone, the waves are acoustic, and in the white zones, they are evanescent. The transmission coefficient as a function of radius is shown in the bottom panels; it decreases only where the waves are evanescent. The point at which the waves become nonlinear and begin to deposit heat in the wind is marked with a dot. For lower wave luminosities, which become nonlinear later, higher angular modes have lower transmission coefficients where wave heating begins.

luminosity, $4\pi r^2 \rho v_{\rm con}^3$, between the edge of the convective zone (r_2) and one pressure scale height below it (r_1), multiplied by the convective mach number, and weighted by mass:

$$L_w = \frac{\int_{r_1}^{r_2} 4\pi r^2 \rho v_{\rm con}^3 \,(v_{\rm con}/c_s)\,(4\pi r^2 \rho) dr}{\int_{r_1}^{r_2} 4\pi r^2 \rho dr}. \tag{5.1}$$

We can similarly calculate the convective frequency, which is equal to the frequency of the waves (Gossan et al., 2020),

$$\omega = \frac{\int_{r_1}^{r_2} \frac{\pi v_{\rm con}}{2H} (4\pi r^2 \rho) dr}{\int_{r_1}^{r_2} 4\pi r^2 \rho dr}, \tag{5.2}$$

where H is the pressure scale height. Explicitly calculating the initial wave luminosity and frequency allows us to improve our wind model as well. Whereas the initial wave luminosity, convective Mach

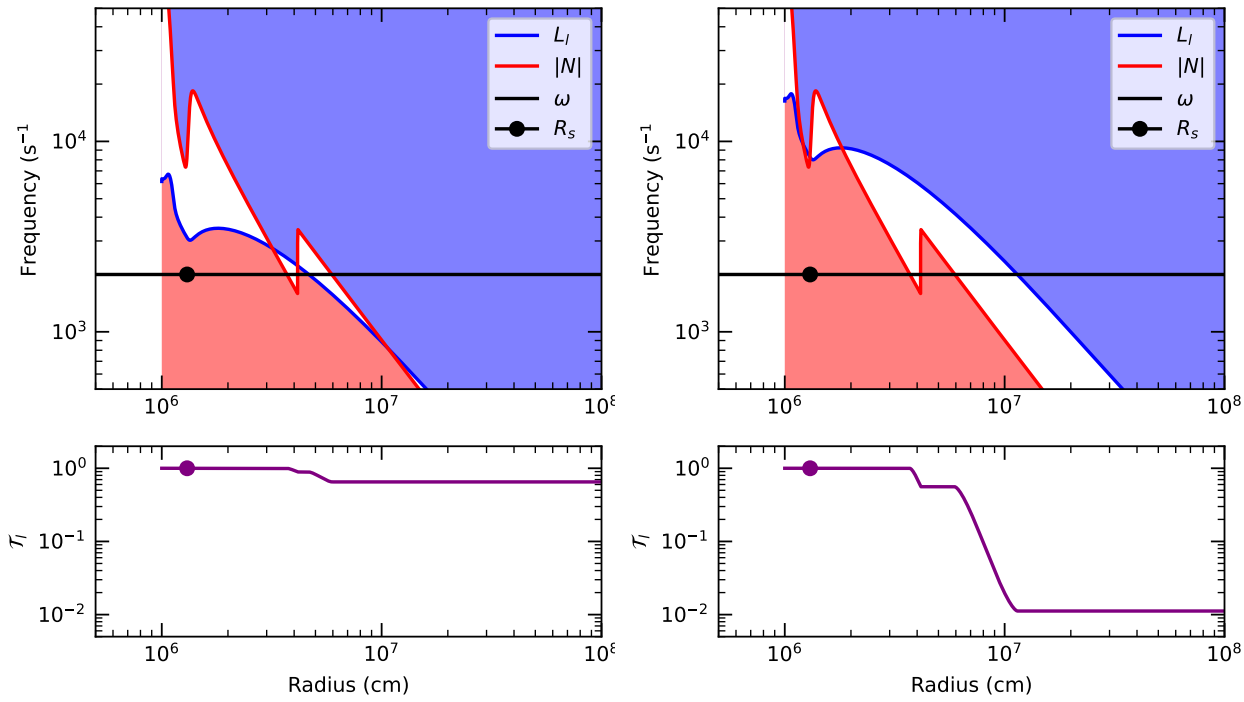

(a) $l = 2$ (b) $l = 6$

Figure 5.3 Wave branches for a fiducial PNS with $M_{\rm NS} = 1.5\,M_\odot$, $L_\nu = 3 \times 10^{52}\,{\rm erg\,s^{-1}}$, $\omega = 2 \times 10^3\,{\rm s^{-1}}$, and a high initial wave luminosity $L_w/L_\nu = 10^{-2}$ for two modes, $l = 2$ (*left*) and $l = 6$ (*right*). Where the wave frequency (black line) is in the red-shaded zone, the waves are gravitational. In the blue zone, the waves are acoustic, and in the white zones, they are evanescent. The transmission coefficient as a function of radius is shown in the bottom panels; it decreases only where the waves are evanescent. The point at which the waves become nonlinear and begin to deposit heat in the wind is marked with a dot. For higher wave luminosities, the waves become nonlinear before encountering the evanescent region.

number, and transmission efficiency were previously all combined into a single parameter L_w/L_ν, we now have the first two explicitly specified by STIR. The third can be specified as well: instead of setting the transmission efficiency by hand, we can calculate it *in situ* by tracking the character of the waves (gravitational, evanescent, or acoustic) as a function of radius. To do so, we calculate two frequencies. The first is the Brunt-Väisälä frequency,

$$N^2 = -\frac{g}{\rho}\left[\frac{d\rho}{dr} - \frac{dP}{dr}\left(\frac{\partial\rho}{\partial P}\right)_s\right]. \tag{5.3}$$

The second is the Lamb frequency, $L_l^2 = l(l+1)c_s^2 r^{-2}$, which depends on the angular mode l of the waves. If the wave frequency ω is less than both N and L_l, the waves are gravitational in character. If ω lies between N and L_l, the waves are evanescent, and if ω is greater than both, the waves are

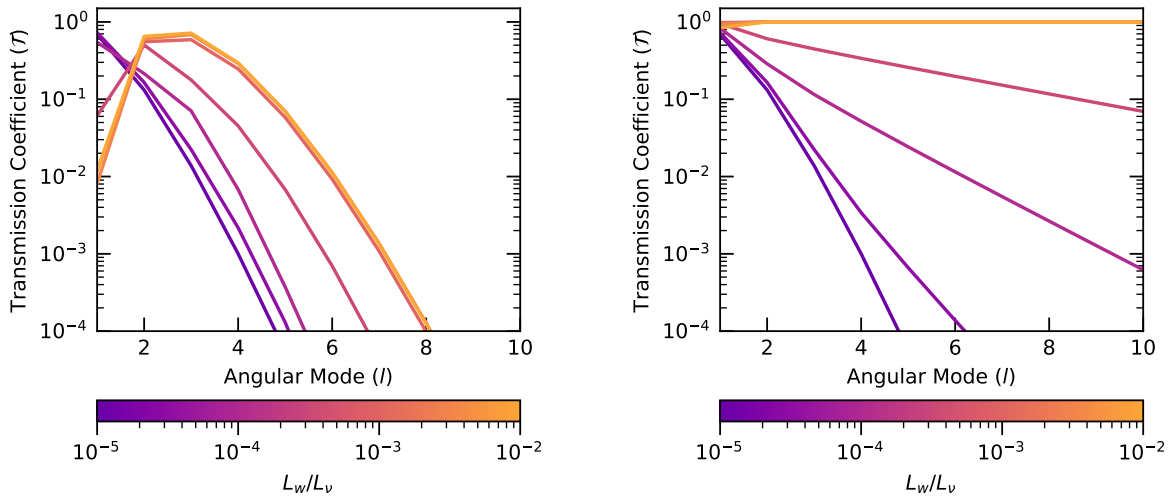

(a) Asymptotic wave transmission efficiency

(b) Wave transmission efficiency at nonlinearity

Figure 5.4 Wave transmission efficiencies for different angular modes, for a fiducial PNS with $M_{\rm NS} = 1.5\,M_\odot$, $L_\nu = 3 \times 10^{52}\,{\rm erg\,s^{-1}}$, $\omega = 2 \times 10^3\,{\rm s^{-1}}$, and varied wave luminosities. We confirm the findings of Gossan et al. (2020) that the asymptotic transmission efficiency (*left*) peaks at $l = 2$ and $l = 3$ for initial wave luminosities near $L_w/L_\nu = 10^{-2}$. The transmission efficiency when the waves become nonlinear and begin to heat the wind (*right*) is more relevant for our purposes, and decreases with l.

acoustic. The evanescent region is then defined as the region in which the frequency of the waves is between the Brunt-Väisälä and Lamb frequencies. Equivalently, the evanescent region is defined as the region for which

$$k_l^2 = \frac{\left(|N|^2 - \omega^2\right)\left(L_l^2 - \omega^2\right)}{\omega^2 c_s^2} < 0. \tag{5.4}$$

Sample representations of these regions for $l = 2$ and $l = 6$ in a fiducial wind are shown in the upper panels of Figures 5.2 and 5.3. Knowing where the waves enter and exit the evanescent region allows us to explicitly calculate the tunneling efficiency $\mathcal{T}$, rather than treating it as a free parameter. For a given angular mode,

$$\mathcal{T}_l = \exp\left[-2\int_{r_1}^{r_2} |k_l| dr\right], \tag{5.5}$$

where r_1 and r_2 denote the boundaries of the evanescent region. Because the tunneling efficiency is cumulative across any and all evanescent regions the waves encounter, we can rewrite $\mathcal{T}_l$ as

$$\mathcal{T}_l(r) = e^{-2\phi_l(r)}, \tag{5.6}$$

where

$$\phi_l(r) = \int_0^r |k_l|\theta(-k_l^2)dr' \tag{5.7}$$

with $\theta(x)$ denoting the Heaviside step function. The total wave luminosity in a given angular mode that reaches to a radius r in the wind is then

$$L_w^l(r) = \mathcal{T}_l(r)L_{w,0}^l, \tag{5.8}$$

where $L_{w,0}^l$ is the initial wave luminosity generated in that angular mode by the PNS convection. The total effective wave luminosity acting to accelerate and heat the wind at a given radius (neglecting dissipation for now) is then

$$\mathcal{L} = \sum_{l=1}^{l_{\rm con}} \mathcal{T}_l(r)L_{w,0}^l. \tag{5.9}$$

Examples of the evolution of $\mathcal{T}_l$ are shown in the lower panels of Figures 5.2 and 5.3.

Following Gossan et al. (2020), we assume a flat spectrum up to a certain maximum value $l_{\rm con} = r_{\rm con}/H$ (rounded down to the nearest integer), where $r_{\rm con}$ is the outer radius of the convective zone of the PNS, and H is the pressure scale height at $r_{\rm con}$. Then $L_{w,0}^l = L_w/l_{\rm con}$ for all angular modes, where L_w is the total convective luminosity of the PNS at the surface, given by Equation (5.1). Since $L_{w,0}^l$ is thus independent of l, the total effective wave luminosity becomes

$$\mathcal{L} = \frac{L_w}{l_{\rm con}} \sum_{l=1}^{l_{\rm con}} \mathcal{T}_l(r). \tag{5.10}$$

This effective wave luminosity must also evolve as dissipation occurs in the wind, which Equation (2.65) accounts for. Since these effects are independent of each other, rather than attempting to derive a new expression for the evolution of $\mathcal{L}$, we can simply make the change

$$\mathcal{L} \to \frac{\mathcal{L}}{l_{\rm con}} \sum_{l=1}^{l_{\rm con}} e^{-2\phi_l(r)}, \tag{5.11}$$

where $\mathcal{L}$ appears in the other evolution equations (Equations [2.61]–[2.66]). Equation (5.7) must also be added to the set of evolution equations for all the angular modes $l \in [1, l_{\rm con}]$. Casting Equation (5.7) in terms of our computational integration variable ψ, we have

$$\frac{d\ln\phi_l}{d\psi} = \frac{|k_l|f_1 r}{\phi_l}\theta(-k_l^2). \tag{5.12}$$

Gossan et al. (2020) predict $l_{\rm con} \lesssim 6$, with $l = 2$ and $l = 3$ having the highest tunneling efficiencies. Considering the higher wave luminosities of $L_w \approx 10^{-2} L_\nu$ they used, we find general agreement with the asymptotic values of $\mathcal{T}_l$ peaking at $l = 2$ and $l = 3$ (see Figure 5.4a). Since we focus on the inner regions of the supernova rather than the primary shock, however, the transmission coefficient at the point where the waves become nonlinear and begin to deposit heat is more relevant. We find that $\mathcal{T}_l$ at the point of shock formation monotonically decreases with l (Figure 5.4b). As the initial wave luminosity is increased, the waves become nonlinear earlier, such that they eventually become nonlinear while still in the gravitational branch. In this situation, $\mathcal{T}_l = 1$ for all modes, and the full wave luminosity acts to heat the wind. The dissipation mechanism is less clear when the waves become nonlinear outside of the acoustic branch, but the effect is the same: the energy of the waves is deposited into the wind as heat.

The parameters extracted from STIR ($M_{\rm PNS}, R_{\rm PNS}, L_{\nu_e}, L_{\bar{\nu}_e}, \langle \epsilon_{\nu_e} \rangle, \langle \epsilon_{\bar{\nu}_e} \rangle, R_{\rm WT}, L_w, \omega$) are used to assemble an ensemble of steady-state models for integration. We sample the parameters from STIR every 10 ms, starting a full second post-bounce to allow time for the primary shock to resolve and a steady-state wind to form, and going through the end of the simulation. With all of the wind model parameters specified by STIR, the only free parameters in our model are those that feed into STIR itself: the properties of the progenitor star and the various MLT parameters. STIR has no free parameters that alter the neutrino physics, and no part of the PNS is excised during the simulation. The only free parameters in STIR are the various MLT coefficients, which are of order unity and tuned to match 3D convective profiles.

5.4 Results from STIR: Model z9.6

The first step in analyzing convection-influenced neutrino winds is to compare winds with convection-driven waves to winds without. One-dimensional supernova models without some additional energy source, or convection in the case of STIR, are notorious for not exploding. There are, however, a few progenitor models that do explode without help, including the z9.6 progenitor (A. Heger, private communication) we examine here. This is a $9.6\,M_\odot$ star with zero metallicity, which explodes in STIR both with and without convection enabled. We ran models for

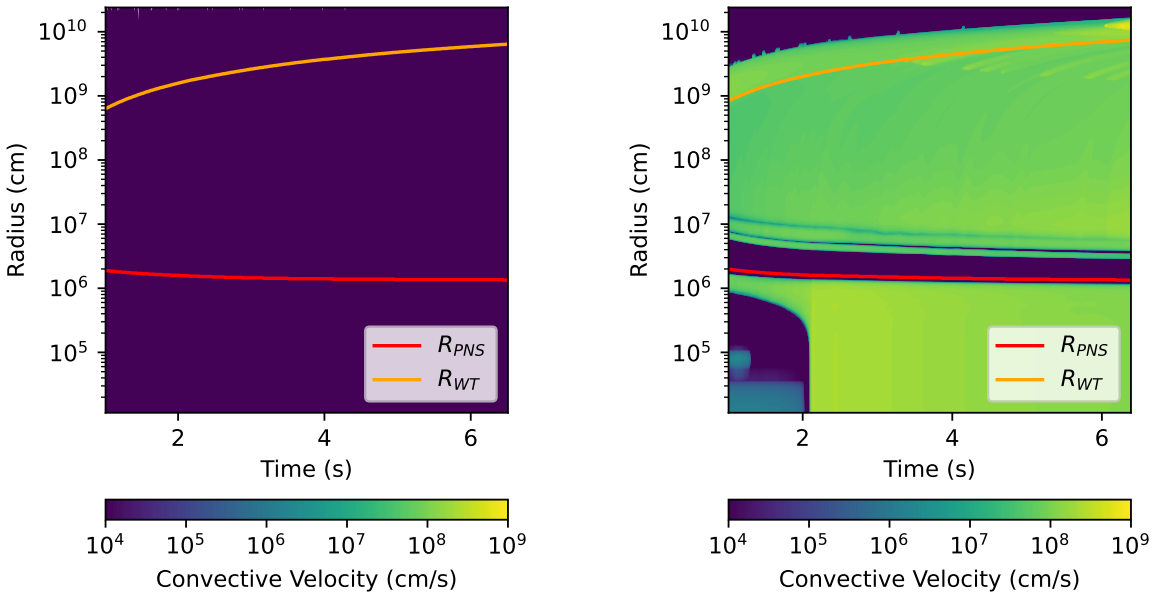

(a) Without convection

(b) With convection

Figure 5.5 Convective velocity reported by STIR as a function of time (post-bounce) and radius, with the PNS and wind termination radii highlighted, for the non-convective (*left*) and convective (*right*) z9.6 models. Just after 2 s post-bounce, the PNS becomes fully and vigorously convective.

this progenitor, both with and without convection, out to ≈ 6 s post-bounce. We discard the first second of each model to allow time for a transonic wind to form.

5.4.1 PNS Parameters

Figures 5.5–5.6 show a number of different PNS parameters from STIR, comparing the model with convection to the model without. The mass of the PNS formed in the explosion does not depend strongly on the presence or absence of convection, with $M_{\rm PNS} \approx 1.35\,M_\odot$ in both cases. The radius and rate of contraction are almost unchanged, as is the expansion rate of the primary shock (Figure 5.5). A close examination shows that in the convective PNS, turbulent pressure causes the PNS radius to contract more slowly, and the primary shock to move outward more quickly. A more stark difference is visible in the neutrino luminosities (Figure 5.6). Both the electron neutrino and electron antineutrino luminosities at early times increase when convection is present, as predicted by, e.g., Roberts et al. (2012b) and Pascal et al. (2022). The values we obtain for PNS mass, radius, and (anti)neutrino luminosity in the convective model are in general agreement with the findings of

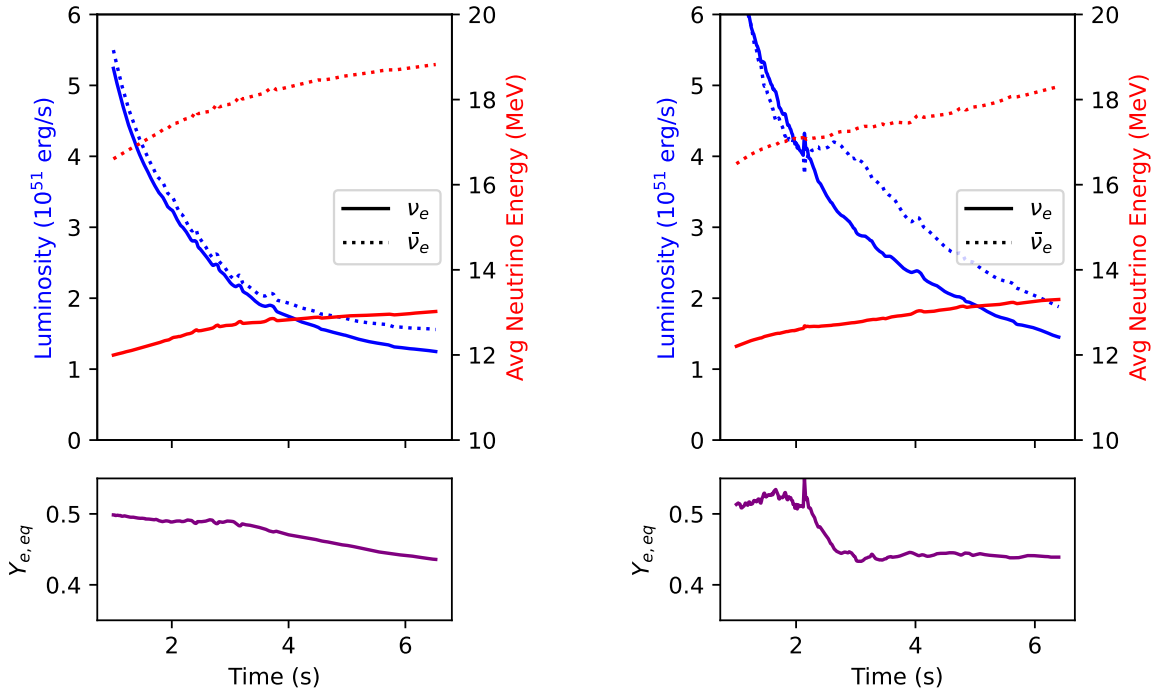

(a) Without convection

(b) With convection

Figure 5.6 PNS neutrino luminosities and average energies from approximately 1 to 6 s post-bounce, both with and without PNS convection. The convective PNS has higher neutrino luminosities at early times, which accords with prior work. Unlike some prior work, we do not observe the electron neutrino and antineutrino energies converging at late times, regardless of convection. In the bottom panels, the predicted equilibrium Y_e in the NDW based on the neutrino parameters is shown. The neutrino properties we observe predict an increasingly neutron-rich wind, unlike most recent prior work.

Wang & Burrows (2024), who examined this same progenitor in 3D, though only to approximately 1 s post-bounce. The average neutrino energies from STIR differ significantly, however, from some prior work, which predicts that the electron neutrino and antineutrino energies should converge at late times (e.g., Fischer et al., 2010; Mirizzi et al., 2016; Pascal et al., 2022). In both the convective and non-convective models, we find that the average energies maintain an approximately constant offset of 5–6 MeV and increase with time. As a result of this neutrino average energy behavior, we find that $Y_{e,\mathrm{eq}}$ moves steadily towards neutron-richness. Both the convective and non-convective models find equilibrium electron fractions more neutron-rich than the most optimistic predictions of Roberts et al. (2012a), and at late, instead of early, times.

Examining the convective model more closely (Figures 5.5 and 5.7), we find that the PNS

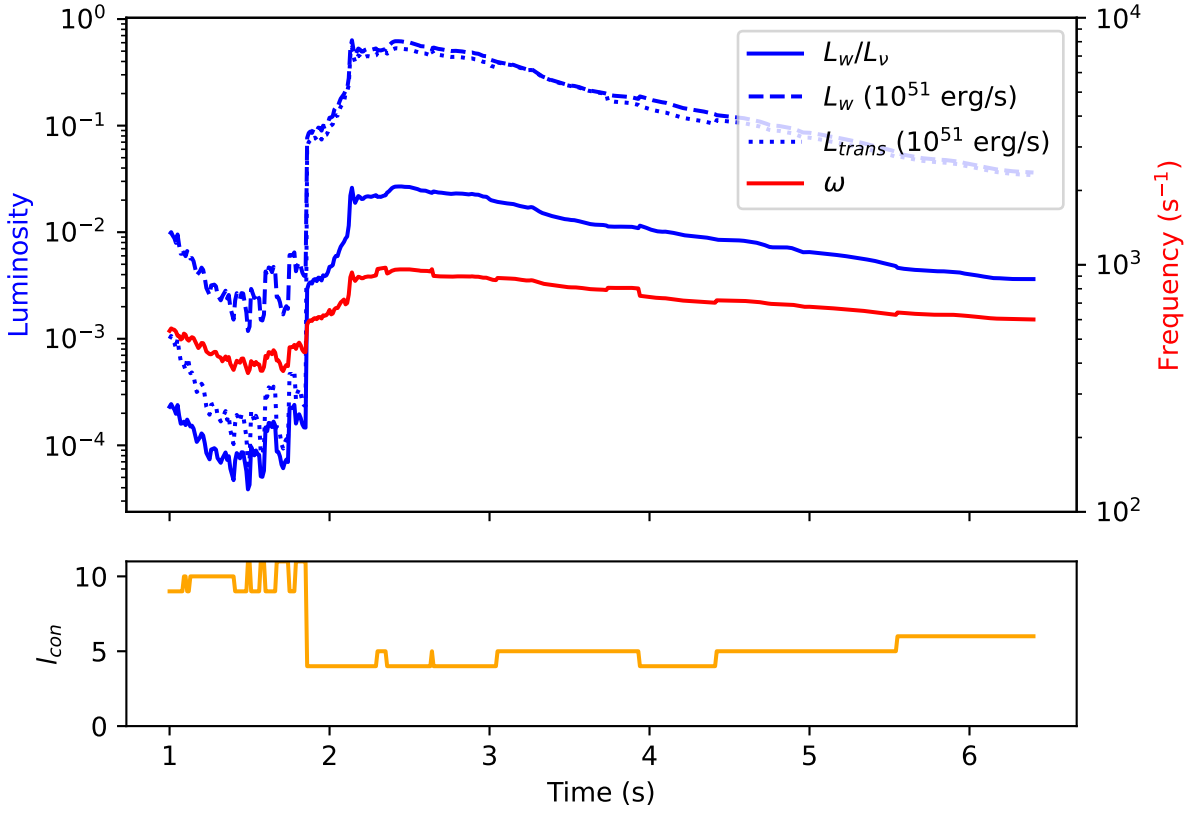

Figure 5.7 PNS convective frequency and wave luminosity from approximately 1 to 6 s post-bounce. Luminosities shown are L_w/L_ν (*solid*), L_w (*dashed*), and $L_{\rm trans}$, the luminosity still present in the wind when the waves become nonlinear, i.e., equation (5.10) evaluated at $r = R_s$ (*dotted*). Convection increases rapidly near $t = 2$ s, becomes most robust at about 2.5 s post-bounce, and then gradually diminishes. We find lower wave luminosities and frequencies compared to Gossan et al. (2020), as well as higher angular modes being excited. Comparing to Wang & Burrows (2024), we find lower L_w, likely due to different calculation methods, but similar values of $L_{\rm trans}$ at early times. Our convective frequencies, however, are much higher than the $\sim 100\,{\rm s}^{-1}$ they report.

becomes fully and vigorously convective at 2 s post-bounce, with the convective luminosity peaking at around 2.5 s post-bounce and subsequently tapering off. The wave luminosity as a fraction of the neutrino luminosity remains above 10^{-3}, which is high enough to substantially impact NDW nucleosynthesis, through the end of the simulation. Where Gossan et al. (2020) predicted initial wave luminosities of order L_ν out to 0.6 s post-bounce, we find $L_w/L_\nu \sim 10^{-3}$ at the start of our model, with a peak value of $L_w/L_\nu \approx 10^{-2}$. The wave luminosity still present in the wind at the point of nonlinearity ($L_{\rm trans}$, Figure 5.7), approximately equal to the acoustic luminosity of Wang & Burrows (2024), is in good agreement with their results at early times, though the absolute wave

luminosities (our L_w, their $L_{\rm PNS}$) differ substantially, likely due to different calculation methods. We also find convective frequencies of $\omega \lesssim 10^3\,{\rm s}^{-1}$ for most of the simulation, slightly lower than the $\omega \gtrsim 10^3\,{\rm s}^{-1}$ found by Gossan et al. (2020). These frequencies are substantially higher than the $\sim 100\,{\rm s}^{-1}$ found by Wang & Burrows (2024) in 3D. Our models predict the excitation of more angular modes, up to $l \approx 10$ at early times when the convective region is small, compared to the maximum of $l = 6$ predicted by Gossan et al. (2020). We attribute this to a difference in calculating the maximum value of l: whereas Gossan et al. (2020) used the full width of the convective region to determine $l_{\rm con}$, we only use the outermost pressure scale height, to maintain consistency with our calculation of the other convective parameters.

5.4.2 NDW Dynamics

We now turn our attention to the winds launched from these proto-neutron stars. As the properties of the PNS evolve over time, so too do the dynamics of the NDW. When convection is neglected, all the relevant properties change very slowly and smoothly, and the NDW follows suit (Figure 5.8). The entropy of the wind rises as the PNS contracts; the wind becomes more neutron-rich as the electron antineutrino luminosity remains slightly higher than the electron neutrino luminosity; and the average electron antineutrino energy remains much higher than that of the electron neutrinos. Such neutron-rich conditions are not entirely unprecedented: Wang & Burrows (2024) observed substantial amounts of ejecta with $Y_e < 0.5$, with trace amounts having $Y_e < 0.4$. Given the low acoustic luminosities they report compared to the neutrino luminosities, it is unlikely that this was caused by wave effects. The velocity profile, and thus the dynamical timescale of the wind, also varies slowly with time. Even at 6 s post-bounce, the PNS radius remains noticeably larger ($\sim$ 14 km) than the 10 km assumed in chapter 3. This, coupled with the low PNS mass of $\approx 1.35\,M_\odot$, results in overall lower wind entropies than we observed in chapter 3, which will reduce the likelihood of heavy element nucleosynthesis. The likelihood of heavy nucleosynthesis is quantified in the figures-of-merit shown in Figure 5.9. These figures-of-merit are functions of entropy, dynamical timescale, and electron fraction calculated at the point of seed nucleus formation ($R_{\rm seed}$, where $T = 0.5\,{\rm MeV}$). Hoffman et al. (1997) found that the r-process would likely extend to

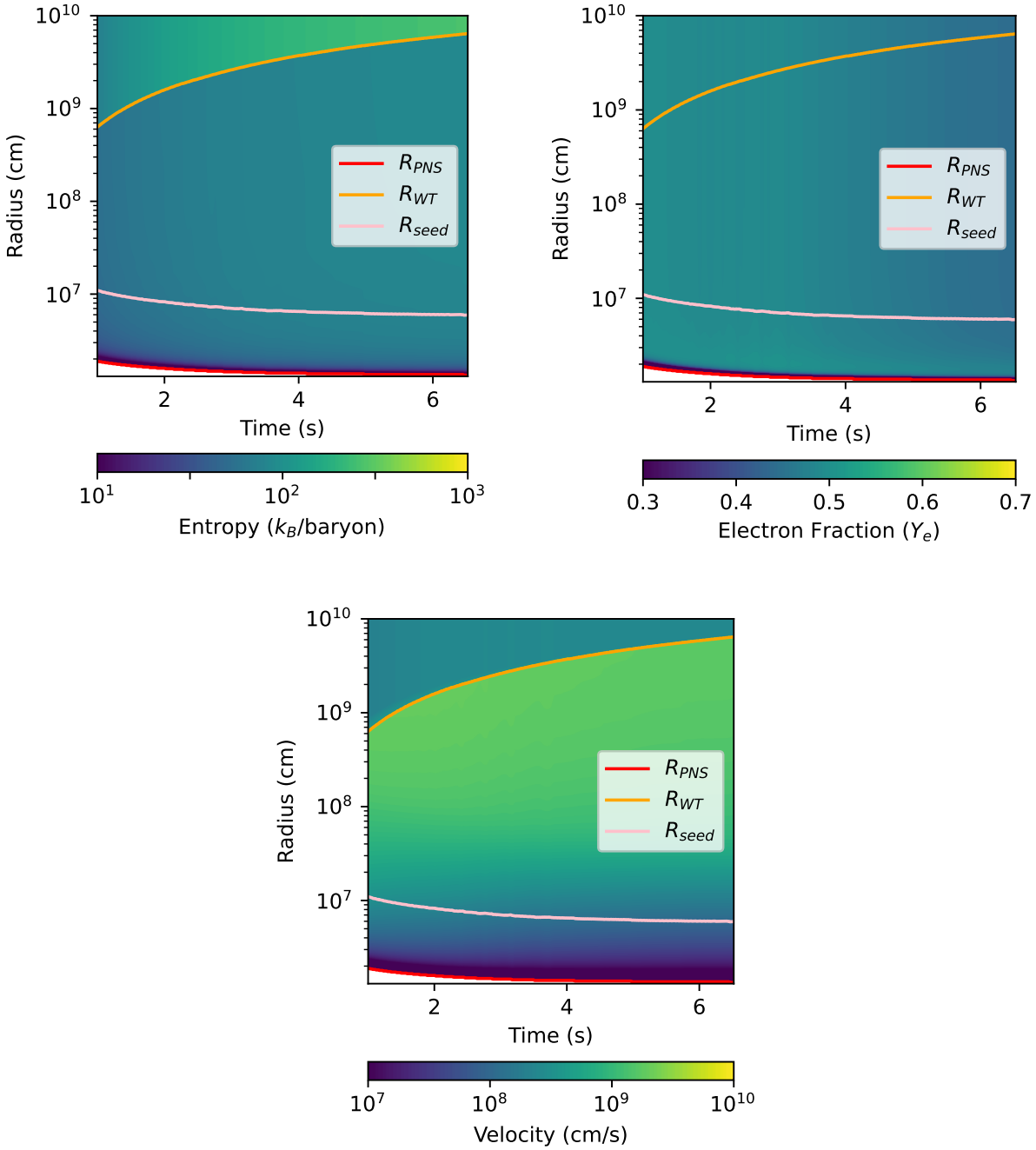

Figure 5.8 Wind entropy (*top left*), electron fraction (*top right*), and velocity (*bottom*) from the steady-state models as a function of time (post-bounce) and radius, with the PNS ($R_{\rm PNS}$), wind termination ($R_{\rm WT}$), wave shock formation (R_s), and seed formation ($R_{\rm seed}$) radii highlighted, for the non-convective z9.6 model. We observe generally low entropies that slowly increase with time, accompanied by a decreasing electron fraction. The velocity profile does not change significantly with time, aside from the movement of the wind termination shock.

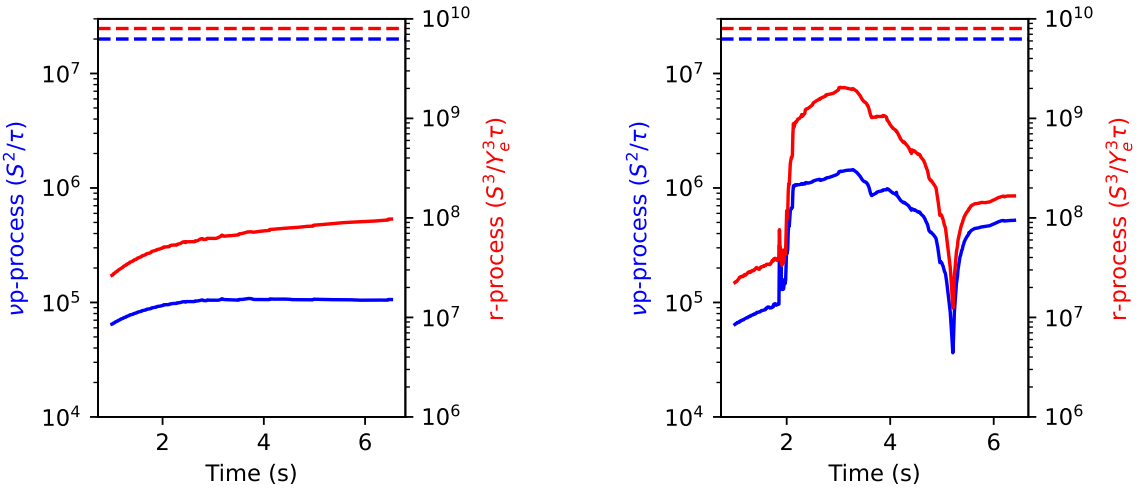

(a) Without convection

(b) With convection

Figure 5.9 Figures of merit for both r-processing ($s^3Y_e^{-3}\tau_d^{-1}$, Hoffman et al., 1997) and νp-processing ($s^2\tau^{-1}$), with critical values for heavy, third-peak nucleosynthesis shown with dashed lines. No heavy nucleosynthesis is expected for winds absent convection. When convection is included, a window of heavier nucleosynthesis opens from $t \approx 2$ to 4 s. Though the entropy of the wind is too low to allow third-peak r-processing, the figure-of-merit becomes high enough to expect some second-peak production.

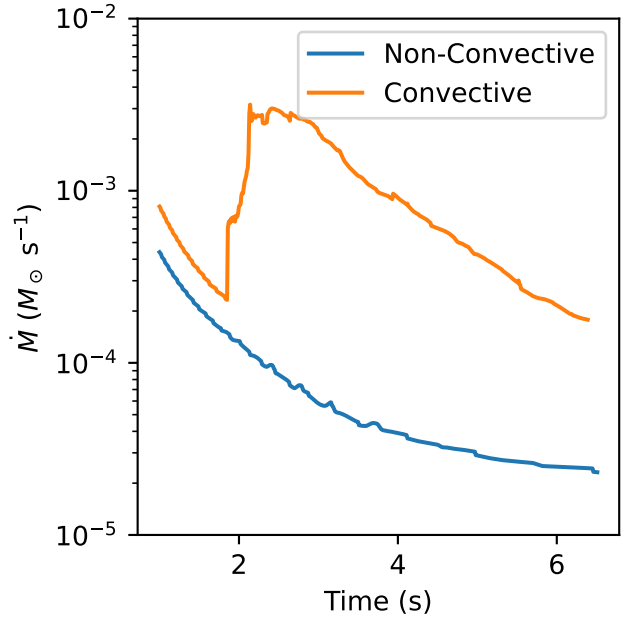

Figure 5.10 PNS mass loss rate due to the NDW, both with and without convection. In the absence of convection, the mass loss rate is approximately monotonic, decreasing with time. When convection is included, propagating waves drive a significant increase in mass loss, evinced by the jump in $\dot{M}$ near $t = 2$ s as the PNS becomes fully convective.

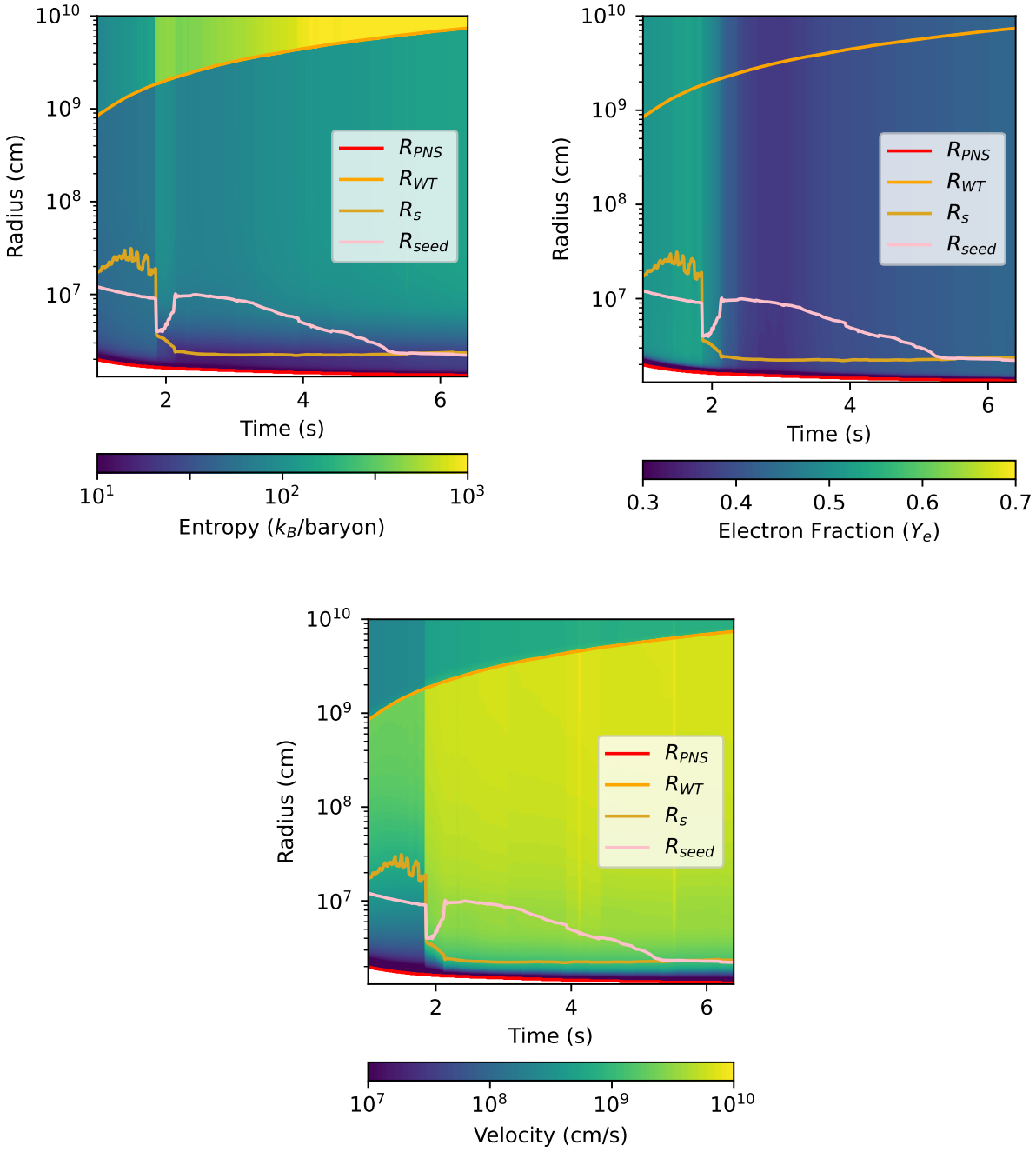

Figure 5.11 Wind entropy (*top left*), electron fraction (*top right*), and velocity (*bottom*) from the steady-state models as a function of time (post-bounce) and radius, with the PNS ($R_{\rm PNS}$), wind termination ($R_{\rm WT}$), wave shock formation (R_s), and seed formation ($R_{\rm seed}$) radii highlighted, for the convective z9.6 model. As the PNS becomes fully convective ($t \approx 2$ s), the asymptotic entropy rises, the electron fraction drops, and the wind is strongly accelerated. When convection becomes vigorous, the waves shock well before seed formation takes place, but the radius of seed formation moves steadily inward over time until the two are simultaneous near $t = 5$ s. At this point, the shock heating by the waves will have minimal impact on the nucleosynthesis, but the acceleration due to the wave stresses will still have a strong effect on the relevant dynamical timescale.

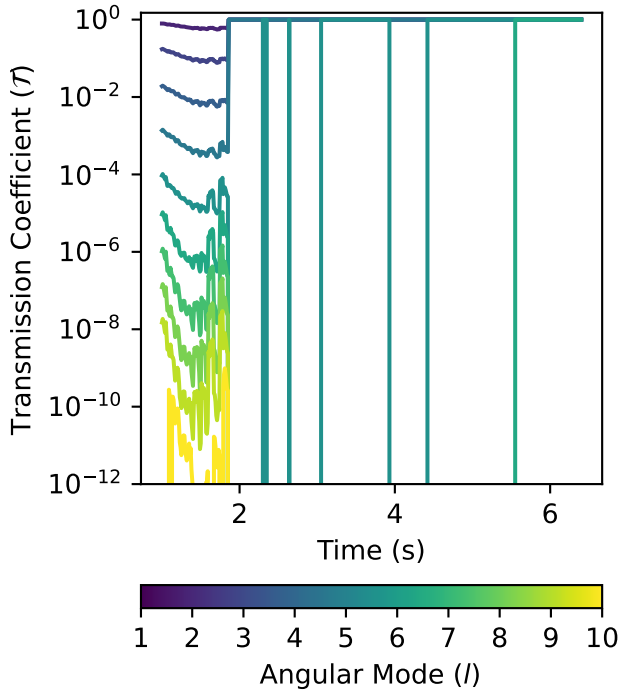

Figure 5.12 Time evolution of the wave transmission coefficients at the point of nonlinearity for different angular modes. At early times, wave energy transmission is dominated by low l modes. When the PNS becomes fully convective at ~ 2 s, the waves (in every mode) become nonlinear while still in the gravitational branch, resulting in 100% of the initial wave luminosity being deposited in the wind as heat.

the third peak for

$$\frac{s^3}{Y_e^3 \tau_d} \gtrsim 8 \times 10^9.$$

Similarly, the νp-process for synthesis of isotopes with $A \gtrsim 200$ is likely to proceed for

$$\frac{s^2}{\tau_d} \gtrsim 2 \times 10^7.$$

We see in Figure 5.9 that the figures-of-merit at the time of seed formation for both strong r-processing and strong νp-processing are well below their threshold values, so we do not expect any heavy element nucleosynthesis in this simulation. Since the wind is driven only by neutrinos, we see the PNS mass loss rate due to the wind decreasing steadily with time (Figure 5.10). Absent convection, a total mass of $\approx 6.9 \times 10^{-5}\, M_\odot$ is ejected in the wind.

The inclusion of convection dramatically changes the dynamics of the wind. While the properties of the PNS still vary slowly compared to the wind's dynamical timescale, the convective

luminosity changes significantly as the PNS becomes fully convective at $t \approx 2\,\mathrm{s}$, and the wind dynamics are altered accordingly (Figures 5.11). The vigorous convection drives the launched waves to become nonlinear while they are still in the gravitational branch, so the full wave luminosity acts to both accelerate and heat the wind (Figure 5.12). The asymptotic entropy of the wind increases with time, again, as the PNS contracts, but the shape of the steady-state curves are significantly altered by shock heating from the waves. The entropy at the time of seed formation is highly variable, due to the sensitive balance between rapid cooling of the wind (due to acceleration from the waves) and reheating of the wind (as the waves form shocks). Though the asymptotic entropy of the wind is maximized at late times, the wind cools so quickly that the seed nuclei form before the waves shock, and their energy deposition does not affect the ensuing nucleosynthesis. With the inclusion of convection, the asymptotic electron fraction is no longer monotonic in time, but becomes extremely neutron-rich near $t = 3\,\mathrm{s}$ due to the combined effects of the high average electron antineutrino energy and the acceleration due to wave stresses, and then slowly rises back toward $Y_e = 0.5$ as convection tapers off . The wind is strongly accelerated by the waves very early on, well before either shock formation or seed formation take place, so the dynamical timescale remains much shorter than the non-convective case after convection becomes vigorous. The figures-of-merit for r- and νp-processing at the time of seed formation (Figure 5.9) are overall much higher when convection is included, with the r-process figure coming within a factor of 5 of the third-peak threshold. Though this wind is unlikely to produce a third-peak r-process, we expect to find second-peak nuclides being synthesized. Based on these results, it is highly likely that a wind from a more massive neutron star would be able to produce third-peak elements. Both figures-of-merit are maximized from $t \approx 2$ to $4\,\mathrm{s}$, and the wind is neutron-rich after $2\,\mathrm{s}$, so any heavy nucleosynthesis will be due to the r-process. Because the waves help to accelerate the wind material, we see a much higher overall mass loss rate due to the wind (Figure 5.10). The rapid increase in $\dot{M}$ near $t = 2\,\mathrm{s}$ is driven by increased wave emission from the PNS becoming fully convective. The total mass loss in the wind is higher when convection is included, with $\approx 3.7 \times 10^{-4}\,M_\odot$ of material being ejected.

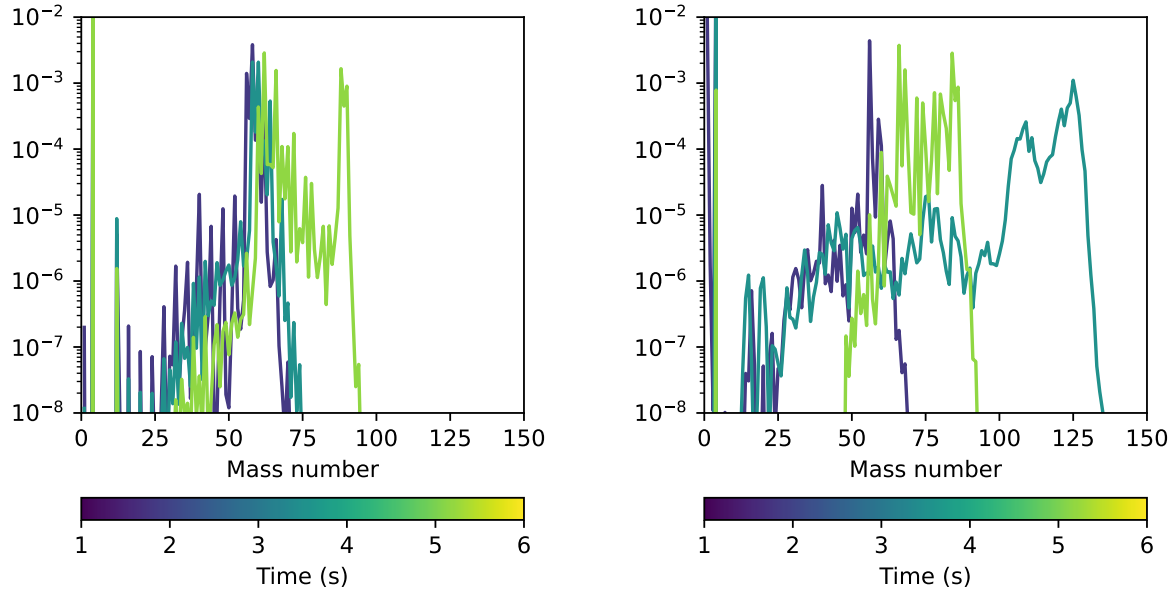

(a) Without convection.

(b) With convection.

Figure 5.13 Snapshot abundance profiles of the NDW at different times. The wind absent convection makes a slow, smooth transition from an iron-peak dominated abundance distribution to a classic weak r-process distribution, resulting in the integrated abundances seen in Figure 5.15. When convection is included, the wind initially yields mainly iron-peak nuclei, and transitions to a stronger second-peak r-process. At late times, an abundance pattern concentrated between mass numbers 50 and 90 emerges, similar to that found by Bliss et al. (2018a) for low-entropy winds from low-mass neutron stars. This gives rise to the sudden jump in $\bar{A}$ seen in Figure 5.14.

5.4.3 Nucleosynthesis

While inspection of the dynamics of the wind can yield helpful predictions of what nucleosynthesis will take place in the wind, the figures-of-merit were derived assuming a constant entropy in the wind (Hoffman et al., 1997). When wave contributions are included, the entropy during nucleosynthesis is no longer approximately constant, so detailed nucleosynthesis calculations are needed. Following the procedure outlined in section 5.1, we calculate the nucleosynthesis for each of the steady-state wind profiles generated from the STIR z9.6 models, and sum the resulting abundance profiles weighted by the mass-loss rate of the corresponding steady-state wind. In the non-convective case, we find good agreement with prior work (e.g., Arcones & Thielemann, 2012; Wanajo, 2013): the wind undergoes an α-process in the slightly neutron-rich conditions found at

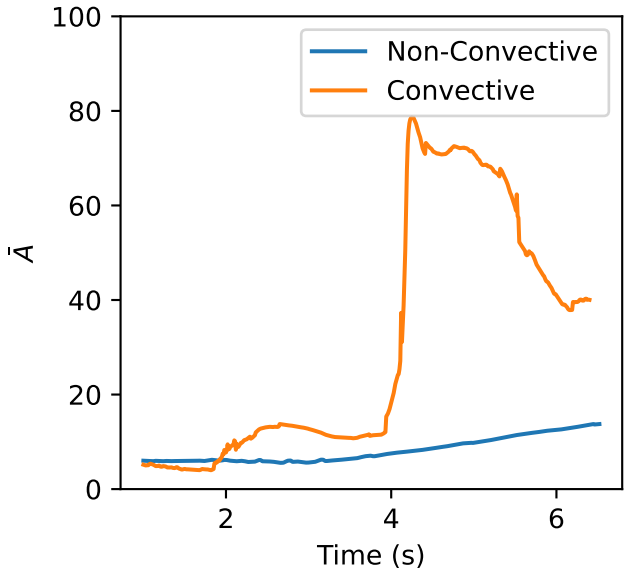

Figure 5.14 Average atomic mass number $\bar{A}$ produced in the NDW as a function of time, both with and without convection. In the absence of convection, $\bar{A}$ remains below 20 at all times, increasing with the figure-of-merit. When convection is included, $\bar{A}$ follows the figure-of-merit, staying below 20, until approximately $t = 4$ s. After this point, it rapidly rises to $\bar{A} \approx 80$ and remains above 40 for the duration of the wind.

early times, and as the wind becomes more neutron-rich, smoothly transitions to a weak r-process producing first-peak nuclides (Figure 5.13). The average atomic mass synthesized in the wind (Figure 5.14) rises smoothly as the wind becomes more neutron-rich with time. The integrated nucleosynthesis (Figure 5.15) is dominated by the iron peak, with a significant amount of first-peak r-process elements also being produced.

When convection is included, higher entropies and more neutron-rich winds yield heavier nucleosynthesis. As Figure 5.13 shows, during the first, proton-rich second of the wind, the yield is dominated by the α-process, which produces mainly iron-peak elements with $\bar{A} \approx 5$ (Figure 5.14). When convection becomes vigorous, the wind becomes extremely neutron-rich and produces a second-peak r-process with $\bar{A} \approx 15$. At late times, as convection tapers off and the wind gradually becomes less neutron-rich, a peculiar abundance profile emerges with yields concentrated between $A = 50$ and 90, with a much higher average atomic mass $\bar{A} > 40$. Figure 5.16 yields additional insight into the nucleosynthesis. The two plots show the beginning ($T = 0.5$ MeV ≈ 5.8 GK) and

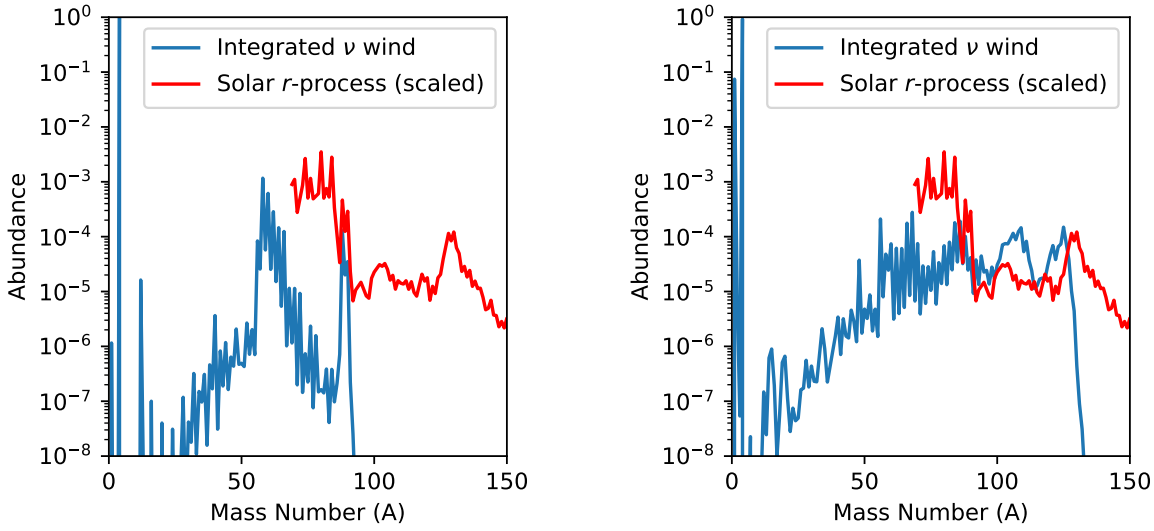

(a) Without convection.

(b) With convection.

Figure 5.15 Integrated nucleosynthesis in the NDW, both with and without convection. A scaled plot of the solar r-process abundances (Arnould et al., 2007) is overlaid for comparison. In the absence of convection, we observe strong iron-peak production with a weak r-process producing only first-peak elements, in agreement with prior work. When convection is included, nucleosynthesis proceeds to much heavier elements, producing much larger amounts of both first- and second-peak r-process material.

end ($T = 2.5\,\mathrm{GK}$) of the α-process, in which the seed nuclei for any possible r- or νp-process are formed, for each timestep, i.e., each steady-state wind for which nucleosynthesis was calculated. They show the abundances of free protons, free neutrons, α particles, and heavy seed nuclei ($A > 4$). When the peculiar abundance profile emerges at $t \approx 4\,\mathrm{s}$, we observe no radical change in these abundances at the start of the α-process. The most notable change is a slight drop in the α abundance, accompanied by a rise in the seed abundance, which indicates a slightly larger number of seed nuclei being produced. At the end of the α-process, however, we see a drastic change in the abundances of free neutrons and α particles. This indicates a strong α-process in which most of the α particles are being captured into heavier nuclei. Most of these α particles, though, are not undergoing a triple-α reaction to form additional seed nuclei, since the seed abundance is unchanged at the end of the α-process. Rather, the α particles and the free neutrons are capturing onto existing seed nuclei to form a large abundance of heavier elements. The result is an abundance distribution concentrated between $A = 50$ and 90, and accompanied by some abundance of surviving α particles, depending

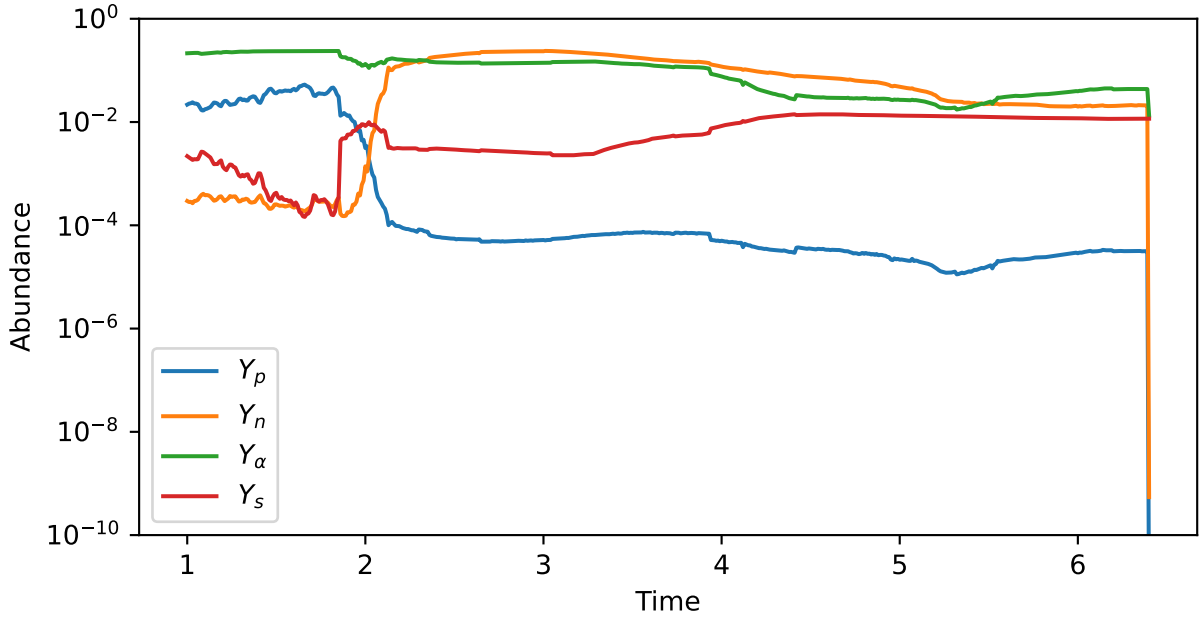

(a) $T = 0.5\,\mathrm{MeV}$.

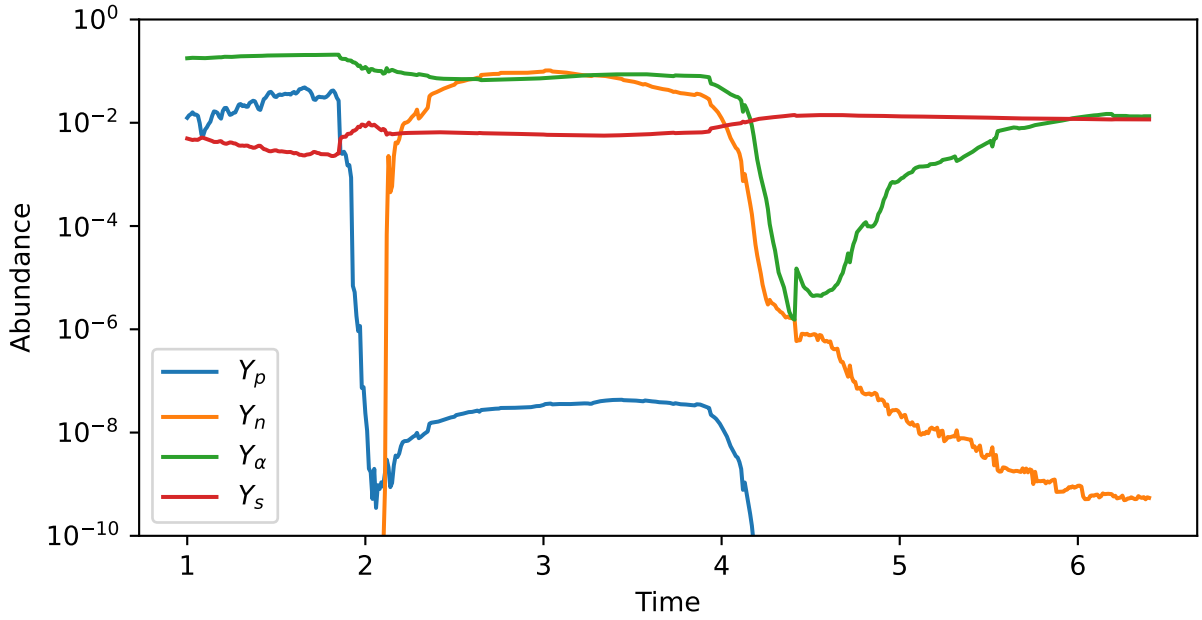

(b) $T = 2.5\,\mathrm{GK}$.

Figure 5.16 Abundances of free protons, free neutrons, α particles, and seed nuclei ($A > 4$) at the start ($T = 0.5\,\mathrm{MeV}$) and end ($T = 2.5\,\mathrm{GK}$) of seed nucleus formation in steady-state winds as a function of time. The late-time $A = 50$–90 abundance pattern at $t = 4\,\mathrm{s}$ arises from a strong period of α-capture and neutron-capture reactions before charged-particle reactions freeze out. The majority of these reactions are not the seed-forming triple-α but rather α captures onto heavier nuclei; the seed abundance remains approximately constant as the steady-state winds pass through that temperature regime, while the α abundance dramatically decreases. No proper r-process takes place in these winds, as the free neutrons are almost entirely captured during the α-process phase.

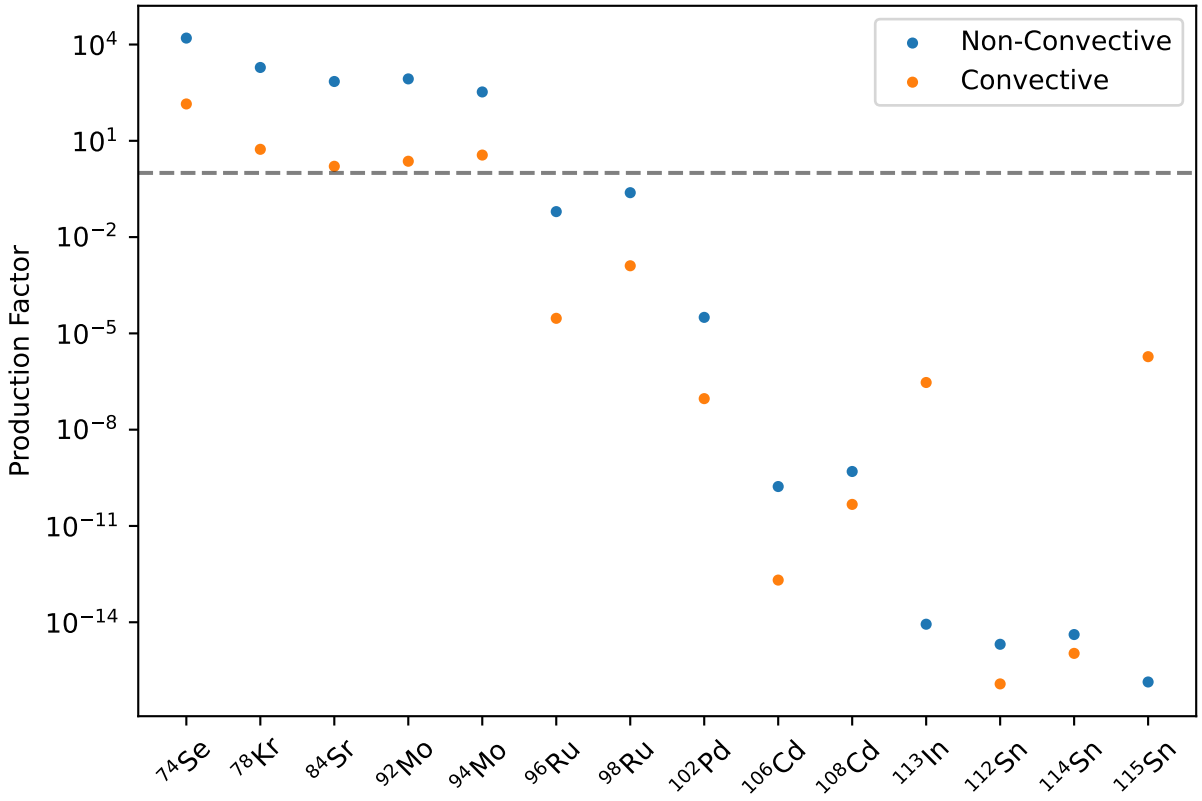

Figure 5.17 Production factors of various p-nuclides of uncertain origin. Despite the wind being neutron-rich for most of its duration, both the convective and non-convective models produce significant abundances of p-nuclides through ^{94}Mo, but produce little to none of the more massive p-nuclides. The non-convective model, which remains generally closer to proton-richness, naturally produces more of these nuclides.

on how efficiently they were captured. Bliss et al. (2018a) observed this abundance pattern for fast, low-entropy, neutron-rich winds, and this matches well with the wind conditions we find at late times. Though the asymptotic entropy of the late-time wind is fairly high, the entropy at the point of seed formation is quite low, well below the entropy at seed formation of the non-convective model; while the outflow speed in the convective case is much higher (Figures 5.8 and 5.11). Overall, the integrated nucleosynthesis (Figure 5.15) in the convective case is dominated by the longer-lasting r- and late-time α-processes, with strong production up to $A \approx 130$.

While our models do not account for the explosive nucleosynthesis taking place in the rest of the supernova ejecta, it is of interest to compare our integrated abundance patterns with the (scaled) solar r-process component (Arnould et al., 2007), which is overlaid in Figure 5.15. In the

non-convective case, the neutrino-driven wind appears to produce a significant peak near $A = 90$, which corresponds to a peak in the solar distribution, and synthesize significant amounts of lighter r-process nuclei. Winds from proto-neutron stars with minimal convection could be a significant source for these "weak r-process" elements, as others have observed (e.g., Wanajo, 2013; Wang & Burrows, 2023). Though in both models the wind is neutron-rich for the majority of its lifespan, the possibility of an incomplete α-recombination due to high wave luminosities (see chapter 4) and the brief proton-rich stage of the convective model together allow for the synthesis of p-nuclides such as ^{92,94}Mo and ^{96,98}Ru. The origin of these nuclei is an outstanding question (Rauscher et al., 2013), as they cannot be produced by either of the traditional s- or r-processes. NDWs have been explored as possible sites for their synthesis, and have been found to be plausible sources for the p-nuclides up to ^{98}Ru (Eichler et al., 2017; Bliss et al., 2018b). Figure 5.17 shows the integrated production factors for various p-nuclides in both of our models. We find agreement with Eichler et al. (2017), with significant production of ^{92,94}Mo in both models, but negligible amounts of the heavier p-nuclides due to the neutron-richness of the winds.

5.5 Conclusions

To circumvent the limitations of steady-state models in predicting nucleosynthesis yields from realistic, time-dependent neutrino-driven winds, we modeled a suite of steady-state winds for realistic time-varying PNS parameters, including convection, and integrated the nucleosynthetic yields. The PNS parameters were sampled from a pair of supernova models run using STIR, a 1D supernova code that uses MLT to simulate convection both in the primary explosion and in the PNS. The models used the same progenitor, a zero-metallicity 9.6 $M_\odot$ star that explodes self-consistently in spherical symmetry, with one model including convective effects and one excluding them. From the STIR simulations, we find a number of interesting results:

1. In both the convective and non-convective models, the electron neutrino and antineutrino average energies do not converge at late times. Rather, they maintain an approximately constant offset of 5–6 MeV throughout the duration of the wind.

2. The equilibrium electron fraction in the wind predicted by the neutrino spectrum (Qian & Woosley, 1996) is increasingly neutron-rich in both models.

3. The PNS becomes fully convective at approximately 2 s post-bounce, later than most 3D models have explored.

Further STIR simulations will be helpful in determining whether the neutrino properties observed in these models are typical of CCNSe, or an artifact of this unique progenitor.

Using PNS parameters sampled from these models, we ran an ensemble of steady-state winds and integrated the resulting nucleosynthesis. The neutrino spectra in both cases led to a neutron-rich wind, and the presence of vigorous PNS convection and highly efficient transmission of the ensuing gravito-acoustic wave energy to the NDW enhanced this effect. In the non-convective case, we observed an increasingly neutron-rich wind that approached $Y_e = 0.4$ at late times. A low wind entropy, due to a light, low-compactness PNS, resulted in a classic weak r-process pattern emerging from this model. Winds from such supernovae, with low-mass remnants and minimal wave generation, could contribute significantly to the production of first-peak r-process elements and some of the lighter p-nuclei such as ^{92,94}Mo.

In the convective case, the PNS becoming fully convective at approximately 2 s post-bounce led to the development of a very neutron-rich wind, with asymptotic electron fractions as low as $Y_e \approx 0.35$. Efficient energy deposition by convection-driven waves generated entropies high enough to drive a strong second-peak r-process, but were insufficient to reach the third peak. If a heavier, or more compact, PNS were to form with a similar neutrino spectrum, it is likely that the higher wind entropy would be sufficient to drive a full, third-peak r-process. Simulations like those of Wang & Burrows (2024) will prove invaluable in the continued examination of these findings, especially as they are carried out to later times.

In the course of this work, a number of improvements were made to the STIR model as well, which will be detailed in a forthcoming paper (Couch et al., in prep.). The neutrino spectra that were observed in this work exhibit notable differences from prior work, especially in the behavior of

the average energies of the electron neutrinos and antineutrinos, which help produce the extremely neutron-rich conditions found here. We eagerly await further advances in late-time 3D supernova models to clarify these findings. Regardless, our results show the strong effect convection-driven gravito-acoustic waves can have on the integrated nucleosynthesis of the NDW, including reduction of the asymptotic electron fraction by as much as 20% and production of the second r-process peak in a relatively low-entropy environment.

CHAPTER 6

SUMMARY AND FUTURE DIRECTIONS

6.1 Summary

In this work, we have examined gravito-acoustic wave generation by convection in the outer layers of a proto-neutron star, and the effects resulting from the propagation of these waves into the neutrino-driven wind. In chapter 1, an overview of core-collapse supernovae, PNS formation, and the neutrino-driven wind were provided. Within the NDW, as matter freezes out from NSE, there is a phase of α-recombination, followed by seed formation and then either an r- or νp-process. The waves primarily affect α-recombination and seed formation, and we discuss in detail the physical processes involved. The main effects of these waves, we predicted, would be an acceleration of the wind due to the momentum flux of the waves, and an increase in entropy when the waves began to shock. We predicted that these twin effects would cause a reduction in neutrino heating and a consequent decrease in the asymptotic electron fraction of the wind.

In chapter 2, we derived a mathematical model to describe the neutrino-driven wind in the steady-state, spherically symmetric approximation that is typically used. In this model, we incorporated all the commonly modelled phenomena affecting the NDW: neutrino heating and its effects on the electron fraction, corrections from general relativity, and the wind termination shock; as well as the effects from the waves. We considered both the role of wave stresses in accelerating the wind, and the entropy deposition that occurs when the waves form shocks. A set of numerical equations were derived for simulating these winds.

In chapter 3, we used the numerical models developed in chapter 2 to explore the possibility of r-processing in a slightly neutron-rich wind. For these models, we chose electron neutrino and antineutrino average energies such that the equilibrium electron fraction in the wind, absent wave effects, would match the best-case scenarios for neutron-rich winds in recent simulations. We then examined how the wind dynamics and nucleosynthesis depend on the PNS mass, neutrino luminosity, wave luminosity, and wave frequency. Our results indicated that a strong r-process was possible and highly dependent on PNS mass and wave luminosity. If PNS convection were

strong, producing a wave luminosity of about 1% the neutrino luminosity, we predicted that a strong r-process would emerge.

A potential r-process, however, is not the only nucleosynthesis of interest in the NDW. In chapter 4, we performed a similar analysis of proton-rich winds, which recent simulations favor. The electron neutrino and antineutrino average energies were tuned to produce a proton-rich equilibrium electron fraction. Exploring the same PNS parameter space, we found that propagating waves could have an important impact on the νp-process and allow nucleosynthesis up to $A \gtrsim 200$ to take place. As in the neutron-rich case, the nucleosynthesis depends strongly on the PNS mass and the wave luminosity. Even a modest wave luminosity allowed the νp-process to proceed to fairly high mass numbers. At high wave luminosities, of order 1% the neutrino luminosity, we found an interesting result: the waves formed shocks early enough in the wind to disrupt even the earliest stages of nucleosynthesis, and a suppressed third-peak r-process took place despite neutrino energies that predicted a proton-rich wind.

Having determined that propagating waves have a significant impact on nucleosynthesis even for fiducial PNS parameters, in chapter 5 we sought to explore the time-integrated nucleosynthesis of a realistic, evolving PNS. To do so, we extracted PNS properties from the supernova code STIR for a certain progenitor star that explodes reliably in 1D. We used these properties to run an ensemble of steady-state winds, the nucleosynthesis yields of which we then integrated. This allowed us to make more robust predictions of the nucleosynthesis likely to result in the inner ejecta of a core-collapse supernova. We found a curious result: the neutrino spectrum predicted by STIR gave rise to extremely neutron-rich winds at late times, even when wave effects were neglected. We also found that the energy transmission by the waves to the wind was far more efficient than we first expected, so that the energy deposited by the waves approached 10% of the neutrino luminosity. Even so, we did not observe a third-peak r-process due to the low wind entropy during the early stages of nucleosynthesis. This was primarily due to the low PNS mass resulting from this particular progenitor, well below the lowest mass considered in our parameter studies, and its larger radius. Whereas we had assumed a 10 km PNS radius in our parameter studies, STIR

predicts an asymptotic radius close to 14 km. Such a low-compactness PNS resulted in much lower wind entropy compared to our parameter studies, and we only observed second-peak r-process production. Nevertheless, our results clearly demonstrate the key role PNS convection and wave propagation can play in shaping the dynamics and nucleosynthesis of the neutrino-driven wind, and the importance of well-resolving these effects in future simulations.

6.2 Future Research Directions

Our exploration of time-dependent winds in chapter 5 has opened some interesting pathways for further study. Though a full r-process did not attain for the PNS we examined, our results indicate that, if the neutrino spectrum we observed is typical, a full r-process could proceed for a core-collapse supernova that produces a more massive remnant. Further exploration of integrated, time-dependent nucleosynthesis from a variety of progenitors is needed: first, to confirm whether the neutrino spectrum observed here is anomalous; and second, to determine if third-peak r-processing (or if the neutrino spectrum is anomalous, νp-processing) is possible or likely in realistic core-collapse supernovae. Also of interest is the nucleosynthetic yield of winds from other STIR simulations. As mentioned in chapter 5, there are a number of nuclides of uncertain origin, for which the NDW is a promising nucleosynthesis site. If proton-rich winds are observed in other simulations, the strong wave luminosity could drive a robust νp-process that forms many of these nuclides.

In the course of this work, STIR has undergone many improvements and is still under active and vigorous development. We look forward to examining future STIR simulations in the manner described in chapter 5. We may also consider relaxing the steady-state assumption in our derivation of the wave effects, and directly including them in STIR. Nucleosynthesis could then be performed using a tracer particle method to determine the full ejecta composition. We also eagerly await future 3D exploration of late-time PNS evolution and neutrino wind behavior, which resolves the wave effects discussed here.

BIBLIOGRAPHY

Arcones A., Montes F., 2011, ApJ, 731, 5

Arcones A., Thielemann F.-K., 2012, Journal of Physics G: Nuclear and Particle Physics, 40, 013201

Arcones A., Janka H. T., Scheck L., 2007, A&A, 467, 1227

Arcones A., Fröhlich C., Martínez-Pinedo G., 2012, ApJ, 750, 18

Arnould M., Goriely S., 2003, Physics Reports, 384, 1

Arnould M., Goriely S., Takahashi K., 2007, Physics Reports, 450, 97–213

Bliss J., Witt M., Arcones A., Montes F., Pereira J., 2018a, ApJ, 855, 135

Bliss J., Arcones A., Qian Y. Z., 2018b, ApJ, 866, 105

Burbidge E. M., Burbidge G. R., Fowler W. A., Hoyle F., 1957, Reviews of Modern Physics, 29, 547

Burrows A., Vartanyan D., 2021, Nature, 589, 29

Burrows A., Radice D., Vartanyan D., 2019, Monthly Notices of the Royal Astronomical Society, 485, 3153–3168

Camelio G., 2018, PhD thesis, University of Rome "Sapienza", https://doi.org/10.48550/arXiv.1801.01350

Cardall C. Y., Fuller G. M., 1997, ApJ, 486, L111

Cavallo L., Cescutti G., Matteucci F., 2021, Monthly Notices of the Royal Astronomical Society, 503, 1–12

Couch S. M., 2017, Philosophical Transactions of the Royal Society A: Mathematical, Physical and Engineering Sciences, 375, 20160271

Couch S. M., Ott C. D., 2015, The Astrophysical Journal, 799, 5

Couch S. M., Warren M. L., O'Connor E. P., 2020, The Astrophysical Journal, 890, 127

Curtis S., Ebinger K., Fröhlich C., Hempel M., Perego A., Liebendörfer M., Thielemann F.-K., 2018, The Astrophysical Journal, 870, 2

Côté B., et al., 2019, The Astrophysical Journal, 875, 106

Desai D., Siegel D. M., Metzger B. D., 2022, ApJ, 931, 104

Dessart L., Burrows A., Livne E., Ott C. D., 2006, ApJ, 645, 534

Drout M. R., et al., 2017, Science, 358, 1570–1574

Duncan R. C., Shapiro S. L., Wasserman I., 1986, ApJ, 309, 141

Eichler M., et al., 2017, Journal of Physics G: Nuclear and Particle Physics, 45, 014001

Ekanger N., Bhattacharya M., Horiuchi S., 2022, Monthly Notices of the Royal Astronomical Society, 513, 405–419

Fischer T., Whitehouse S. C., Mezzacappa A., Thielemann F.-K., Liebendörfer M., 2010, A&A, 517, A80

Fischer T., Guo G., Dzhioev A. A., Martínez-Pinedo G., Wu M.-R., Lohs A., Qian Y.-Z., 2020, PhRvC, 101, 025804

Friedland A., Mukhopadhyay P., Patwardhan A. V., 2023, arXiv e-prints, p. arXiv:2312.03208

Fröhlich C., Martínez-Pinedo G., Liebendörfer M., Thielemann F. K., Bravo E., Hix W. R., Langanke K., Zinner N. T., 2006, PhRvL, 96, 142502

Goldreich P., Kumar P., 1990, ApJ, 363, 694

Gossan S. E., Fuller J., Roberts L. F., 2020, MNRAS, 491, 5376

Hoffman R. D., Woosley S. E., Qian Y.-Z., 1997, ApJ, 482, 951

Hüdepohl L., 2013, PhD thesis, Technische Universitat M ¨ unchen ¨ Max-Planck-Institut fur¨ Astrophysik, https://mediatum.ub.tum.de/doc/1177481/file.pdf

Hüdepohl L., Müller B., Janka H.-T., Marek A., Raffelt G. G., 2010, Phys. Rev. Lett., 104, 251101

Jacques S. A., 1977, ApJ, 215, 942

Kennedy C., Carpenter M., 2016, Technical report, Diagonally Implicit Runge-Kutta Methods for Ordinary Differential Equations. A Review. National Aeronautics and Space Administration

Kobayashi C., et al., 2023, The Astrophysical Journal Letters, 943, L12

Kuroda T., et al., 2008, in AIP Conference Proceedings. AIP, doi:10.1063/1.2943617, https://doi.

org/10.1063%2F1.2943617

Lippuner J., Roberts L. F., 2017, The Astrophysical Journal Supplement Series, 233, 18

Martínez-Pinedo G., Fischer T., Lohs A., Huther L., 2012, Physical Review Letters, 109

Martínez-Pinedo G., Fischer T., Huther L., 2014, Journal of Physics G: Nuclear and Particle Physics, 41, 044008

Metzger B. D., Thompson T. A., Quataert E., 2007, ApJ, 659, 561–579

Meyer B. S., 2002, PhRvL, 89, 231101

Mihalas D., Mihalas B. W., 1984, Foundations of radiation hydrodynamics. Oxford University Press, Inc.

Mirizzi A., Tamborra I., Janka H. T., Saviano N., Scholberg K., Bollig R., Hüdepohl L., Chakraborty S., 2016, La Rivista del Nuovo Cimento, 39, 1–112

Nagakura H., Burrows A., Radice D., Vartanyan D., 2020, Monthly Notices of the Royal Astronomical Society, 492, 5764

Nagakura H., Burrows A., Vartanyan D., 2021, MNRAS, 506, 1462

Nevins B., Roberts L. F., 2023, Monthly Notices of the Royal Astronomical Society, 520, 3986

Nevins B., Roberts L. F., 2024, Monthly Notices of the Royal Astronomical Society, 530, 2001–2011

Otsuki K., Tagoshi H., Kajino T., ya Wanajo S., 2000, ApJ, 533, 424

O'Connor E., 2015, The Astrophysical Journal Supplement Series, 219, 24

Pascal A., Novak J., Oertel M., 2022, Monthly Notices of the Royal Astronomical Society, 511, 356

Pllumbi E., Tamborra I., Wanajo S., Janka H.-T., Hüdepohl L., 2015, ApJ, 808, 188

Pons J. A., Reddy S., Prakash M., Lattimer J. M., Miralles J. A., 1999, ApJ, 513, 780

Pope S. B., 2000, Turbulent Flows. Cambridge University Press

Prasanna T., Coleman M. S. B., Thompson T. A., 2024, Favorable conditions for heavy element nucleosynthesis in rotating proto-magnetar winds, doi:10.48550/arXiv.2402.06003, https://arxiv.org/abs/2402.06003

Pruet J., Woosley S. E., Buras R., Janka H. T., Hoffman R. D., 2005, ApJ, 623, 325

Pruet J., Hoffman R. D., Woosley S. E., Janka H. T., Buras R., 2006, ApJ, 644, 1028

Qian Y., Woosley S. E., 1996, ApJ, 471, 331–351

Rauscher T., Dauphas N., Dillmann I., Fröhlich C., Fülöp Z., Gyürky G., 2013, Reports on Progress in Physics, 76, 066201

Roberts L. F., 2012, ApJ, 755, 126

Roberts L. F., Reddy S., Shen G., 2012a, Physical Review C, 86

Roberts L. F., Shen G., Cirigliano V., Pons J. A., Reddy S., Woosley S. E., 2012b, Physical Review Letters, 108

Suzuki T. K., Nagataki S., 2005, ApJ, 628, 914–922

Thompson T. A., 2003, The Astrophysical Journal, 585, L33–L36

Thompson T. A., Burrows A., Meyer B. S., 2001, ApJ, 562, 887–908

Timmes F. X., Swesty F. D., 2000, The Astrophysical Journal Supplement Series, 126, 501

Van der Swaelmen M., et al., 2023, Astronomy & Astrophysics, 670, A129

Wanajo S., 2006, ApJ, 647, 1323

Wanajo S., 2013, ApJL, 770, L22

Wanajo S., Kajino T., Mathews G. J., Otsuki K., 2001, The Astrophysical Journal, 554, 578–586

Wanajo S., Janka H.-T., Kubono S., 2011, ApJ, 729, 46

Wang T., Burrows A., 2023, ApJ, 954, 114

Wang T., Burrows A., 2024

Weaver T. A., Zimmerman G. B., Woosley S. E., 1978, ApJ, 225, 1021

Witti J., Janka H. T., Takahashi K., 1994, A&A, 286, 841

Woosley S. E., Baron E., 1992, ApJ, 391, 228

Woosley S. E., Hoffman R. D., 1992, ApJ, 395, 202

Woosley S., Janka T., 2005, Nature Physics, 1, 147–154

Woosley S. E., Wilson J. R., Mathews G. J., Hoffman R. D., Meyer B. S., 1994, ApJ, 433, 229

Xiong Z., Wu M.-R., Qian Y.-Z., 2019, ApJ, 880, 81

Xiong Z., Sieverding A., Sen M., Qian Y.-Z., 2020, ApJ, 900, 144

Zel'dovich Y. B., Raizer Y. P., 1967, Physics of shock waves and high-temperature hydrodynamic phenomena. Dover Publications

Zha S., Müller B., Powell J., 2024, ApJ, 969, 141